Faculdade de Engenharia da Universidade do Porto

Thermo-responsive Magnetic Hydroxyapatite Composites as Theranostics for Triple Negative Breast Cancer

Tiago José Gil Pousa Ribeiro

Dissertation for the Master in Biomedical Engineering

Supervisors
Dr. Marta de Sousa Laranjeira
Prof. Dr. Fernando Jorge Mendes Monteiro

Porto, June 2019

Abstract

Every year, millions of people die of cancer worldwide. Triple negative breast cancer is one of the most aggressive oncological conditions currently known. Such aggressiveness is derived from poor prognostics and the higher grade of this tumour. This breast cancer subtype is known for being the most invasive with a higher tendency of recurrence. Additionally, chemotherapy, commonly associated with undesired side effects due to its non-specific action, is still the best treatment option for this type of tumour. Nonetheless, taking advantage of the biological conditions of tumours, such as high temperatures, smart materials for a controlled drug delivery are a promising solution due to their selective release of both diagnostics and therapeutic agents.

In this work, a multifunctional thermo-responsive composite was designed. For this, iron(III)-doped hydroxyapatite nanoparticles were synthetized and fully characterized in terms of chemical constitution, size, morphology and both electric and magnetic properties. For the carrier, a thermo-responsive polymeric core-shell microgel composed of poly[(N-isopropylacrylamide-co-2-(dimethylaminoethyl methacrylate)] as the core and poly[(N-isopropylacrylamide-co-poly(ethylene glycol) methacrylate] as the shell was synthetized and characterized in terms of size, morphology, chemical profile and thermo-responsiveness. The nanoceramics yielded sizes around 100nm and surface charges of -45±1.3mV. Chemically, the nanoparticles showed to be mostly hydroxyapatite with small phases of tricalcium phosphate, magnetite and hematite. The iron-doped nanoparticles showed both piezoelectric and superparamagnetic properties, presenting good potential for being used in cancer treatment using techniques like electroporation and magnetic hyperthermia. Additionally, they can be applied as contrast agents in T2-weighted contrast in magnetic resonance imaging, concluding that small percentages of iron are enough in order to obtain a contrast signal. In terms of therapy, these nanoparticles proved to be highly toxic to cancer cells, inducing damage at both the mitochondria and cell membrane levels, due to calcium and iron release. Nonetheless, when tested on fibroblasts, less toxic effects were obtained due to the more well-defined mechanisms of healthy cells on dealing with ion overload. As for the polymeric carrier, sizes below 200nm at body temperature were obtained, associated with a lower critical solution temperature of 39.04°C. Additionally, encapsulations of the iron nanoparticles into the microgel were done with relative success, while doxorubicin encapsulation showed a remarkable encapsulation efficiency of 77.7%, added to a loading capacity of 9.32% by the microgels.

In sum, a very promising multifunctional micro system, with great theranostics potential, was developed and characterized. Further studies should include the evaluation of electroporation and magnetic hyperthermia induced cancer cell damage, associated with the final assembly of the magnetic microcarrier.

(page intentionally left blank)

Resumo

Todos os anos, milhões de pessoas morrem de cancro a nível mundial, sendo o cancro da mama triplo negativo uma das condições oncológicas mais agressivas atualmente conhecidas. Tal agressividade é derivada de um fraco prognóstico e às características deste tumor. Este subtipo de cancro da mama é conhecido como sendo o mais invasivo e com uma elevada tendência para reaparecer. No entanto, aproveitando as condições biológicas do tumor, tais como as elevadas temperaturas, materiais inteligentes para uma entrega controlada de fármacos são uma solução promissora devido à sua liberação seletiva de agentes de diagnóstico e terapêuticos.

Neste trabalho, um compósito multifuncional termo-responsivo foi desenvolvido. Para isso, nanopartículas de hidroxiapatite dopada com ferro(III) foram sintetizadas e totalmente caracterizadas em termos de constituição química, tamanho, morfologia e propriedades elétricas e magnéticas. Para o transportador, um microgel polimérico termo-responsivo, em estrutura núcleo-coroa, composto de poli [(N-isopropilacrilamida-co-2- (dimetilaminoetil metacrilato)] como núcleo e poli [(N-isopropilacrilamida-co-poli (etilenoglicol) metacrilato como a coroa foi sintetizado e caracterizado em termos de tamanho, morfologia, perfil químico e termoresponsividade. Os nanocerâmicos apresentaram tamanhos em torno de 100nm e cargas de superfície de -45±1.3mV. Quimicamente, as nanopartículas mostraram ser maioritariamente compostas por hidroxiapatite com pequenas fases de fosfato de tricálcio, magnetite e hematite. As nanopartículas dopadas com ferro apresentaram também, propriedades piezelétricas e superparamagnéticas, tendo por isso potencial para o tratamento do cancro, utilizando técnicas como electroporação e hipertermia magnética. Podendo também serem usadas como agentes de diagnóstico no contraste em T2 em ressonância magnética. Tal potencial de contraste foi confirmado, concluindo que pequenas percentagens de ferro são suficientes para obter um sinal de contraste. Em termos terapêuticos, as nanopartículas mostraram-se altamente tóxicas para células cancerígenas, induzindo danos nas mitocôndrias e na membrana celular, devido à libertação de cálcio e ferro. No entanto, quando testados em fibroblastos, reduzida toxicidade foi verificada devido aos mecanismos bem definidos de células saudáveis em lidar com a sobrecarga de iões. Quanto ao transportador polimérico, foram obtidos tamanhos inferiores a 200nm à temperatura corporal, associados a uma temperatura de transição de 39.04°C. Adicionalmente, o encapsulamento das nanopartículas de ferro no microgel foi realizado com relativo sucesso, enquanto que o encapsulamento de doxorrubicina mostrou uma notável eficiência de encapsulação de 77.7%, somado a uma capacidade de carga de 9.32% por parte dos microgéis.

Em suma, um sistema multifuncional promissor, com grande potencial para teranosticos, foi desenvolvido e caracterizado. Outros estudos deverão incluir a avaliação dos efeitos de eletroporação e de hipertermia magnética em células tumorais, associados à construção final do microtransportador magnético.

“Our greatest weakness lies in giving up. The most certain way to success is always try just one more time”

-Thomas A. Edison

Acknowledgements

First of all, I would like to thank my supervisors, Dr. Marta Laranjeira and Prof. Dr. Fernando Jorge Monteiro for giving me the opportunity to work on their project, for all the knowledge they provided me with, for supporting my ideas and for the friendship. A big thanks goes also to the Biocomposites Group at i3S and to INEB for welcoming me and for making me part of the team.

Secondly, my appreciation goes to Dr. Sónia Silva from the University of Aveiro, for introducing me to nanotechnology and for teaching me the importance of this subject in creating novel solutions for current problems.

To Prof. Dr. Joaquim Agostinho and Prof. Dr. Abílio Almeida, thank you for introducing me to medical physics and for all the patience while explaining me this new concept.

To Dr. Rui Vilarinho and Dr. Fábio Figueiras, thank you for helping me with material characterization and for clarifying many aspects of my work regarding piezoelectricity.

To Rui Fernandes, Ricardo Vidal, Dalila Pedro and Fátima Fonseca, thank you for giving me valuable advice and training in the equipment at i3S.

Now, to my parents, thank for all the motivation words when nothing seemed to work. Thank you for making me what I am today and for always guiding me in the right way.

To all my fellow MEB colleagues and friends, especially Luís and Diana, a big thank you for dealing with me every day and for taking me out of the house to have fun once in a while.

To Francisca Gomes, thank you for all the teaching in polymer chemistry and for the friendship.

A special thanks goes to my friends and housemates, Sara and Beto, for being there and for helping me with my frustrations when work seemed overwhelming.

To Diana, a big thank you for your help, in every single aspect. For listening to my concerns every day, for guiding me through all my frustrations and for being there all the time. Thank you.

(page intentionally left blank)

Contents

(page intentionally left blank)

Figure list

(page intentionally left blank)

Table list

(page intentionally left blank)

Abbreviations

AAPH	2,2′-Azobis(2-methylpropionamidine) Dihydrochloride
APS	Ammonium Persulfate
CT	Computerized Tomography
CTAB	Cetyl Trimethylammonium Bromide
DCIS	Ductal Carcinoma *in situ*
DLS	Dynamic Light Scattering
DMAEMA	2-(Dimethylamino)ethyl Methacrylate
DOX	Doxorubicin
EE	Encapsulation Efficiency
EGF	Epidermal Growth Factor
EPR	Enhanced Permeability and Retention
ER	Estrogen Receptor
FBS	Fetal Bovine Serum
FDA	Food and Drug Administration
Fe-HAp	Iron (III) Doped Hydroxyapatite
FTIR	Fourier-Transform Infrared Spectroscopy
HAp	Hydroxyapatite
HER2	Human Epidermal Growth Factor Receptor 2
HGF	Human Gingival Fibrosblasts
ILC	Invasive Lobular Carcinoma
LC	Loading Capacity
LCST	Lower Critical Solution Temperature
MRI	Magnetic Resonance Imaging
NIPAM	N-isopropylacrylamide
PEG	Poly (ethylene glycol)
PEGMA	Poly (ethylene glycol) methacrylate
PFM	Piezoresponse Force Microscopy
PNIPAM	Poly (N-isopropylacrylamide)
PR	Progesterone Receptor
ROS	Reactive Oxygen Species
SDS	Sodium Dodecyl Sulfate
SPIONs	Superparamagnetic Iron Oxide Nanoparticles
SQUID	Superconducting Quantum Interference Device
TCP	Tricalcium Phosphate
TE	Echo Time
TEM	Transmission Electron Microscopy
TGA	Thermogravimetric Analysis
TNBC	Triple Negative Breast Cancer
TR	Repetition Time

TRT	Tissue Relaxation Time
UV-Vis	Ultraviolet to Visible Radiation Spectroscopy
VEGF	Vascular Endothelial Growth Factor
VPF	Vascular Permeability Factor
XRD	X-ray Diffraction

(page intentionally left blank)

Chapter 1

Introduction

Cancer is one of the most problematic medical conditions in the current years. Despite all the efforts that are being made in terms of diagnostics and treatments. There is still a long way to go until cancer can be controlled and fully treated. Most problems arise from deficient knowledge about the tumour biochemical behaviour and from high prevalence of side effects and low success rates in current therapies.

In this chapter, cancer characteristics will be explained, with emphasis to triple negative breast cancer. Current cancer therapies and diagnostics techniques will be presented, evaluating their advantages and disadvantages, presenting new solutions that are being studied in the oncology field associated with other sciences.

1.1 – Cancer Statistics and Epidemiology

Nowadays, cancer is one of the most severe medical conditions worldwide. According to a global study made in 2018 by the World Health Organization, cancer is the first cause of death in the noncommunicable diseases category and the second in the general one, only being surpassed by heart related diseases. In 2017, cancer caused about 600000 deaths in the United States only, corresponding to about 1600 deaths per day, being lung, pancreatic, colon and breast the most common types of cancer and the most deadly [1]. Worldwide, nearly 8.8 million people died of this condition in 2017, which translates into 1 in every 6 deaths. Still, many advances in oncology have been made in the past years, leading to the reduction of the mortality rates. Between 2005 and 2014, cancer death rates reduced about 1.5% per year, and 25% from 1991 to 2014. Nevertheless, it is still difficult for physicians to provide the best diagnosis and treatment.

One of the main challenges consists in ensuring the correct delivery of chemotherapeutical drugs to the tumour, without affecting healthy tissues and thus reducing the undesired side effects, like loss of hair, fatigue and mutagenesis in healthy cells. This problem is explained by the subtle difference between cancer and healthy cells, which is mostly detected in the biochemical behaviour that has been a very important object of study in the past years.

1.2 - Cancer Biology

Neoplasms, or tumours, were given a definition by W.H. Clarke in 1991 and it is still the one that is used today [2]. This definition describes a tumour as abnormal cells with

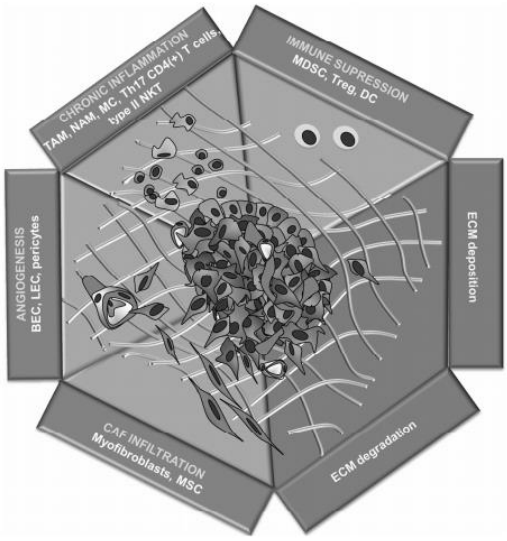

Figure 1.1 – Tumour microenvironment organization and cellular processes. Adapted from [4].

unrestricted growth preference over their normal counterparts. Such cells have the ability to invade surrounding tissues, traverse at least one basement membrane, grow in the mesenchyme at the primary site and may metastasise to distant sites, travelling through the blood and lymphatic systems [3]. More commonly, tumour cells assemble into solid masses, divided in two regions, illustrated in figure 1.1, the parenchyma, which consists in the central mass of cells with abnormal growth, and the stroma which is composed by the extracellular matrix, a basement membrane, blood vessels that irrigate the mass and some cells like bone marrow-derived cells, tumour-associated macrophages or carcinoma-associated fibroblasts [4]. The communication between the different cells in the stroma and in the parenchyma contributes to the establishment of the primary tumour site and of the pre-metastatic niches in other sites, all leading to cell proliferation [5]. These usually translate into other conditions and symptoms, like chronic inflammation, immunosuppression, extracellular matrix reconstructing, with the interchanged cleavage and growth of collagen fibres and especially the development of new blood vessels by a process called angiogenesis, for increased flow of nutrients and oxygen to the tumour site [6].

Two classifications can be attributed to tumours, benign or malignant. The main factor responsible for the differentiation between both is the existence and the integrity of the basal membrane. While malignant tumours are able to break this membrane, through the action of cleaving proteins like collagenases and therefore being able to get into the bloodstream, benign tumours are contained in its limits.

As mentioned before, in tumour sites there is a process called angiogenesis that is responsible for the development of new blood vessels that will provide oxygen, nutrients and some molecules for biosynthesis that are highly required for proliferation to take place. With this information new therapies have been tested in order to inhibit angiogenesis, decreasing the chances of growth and survival of tumour masses. Some molecular factors such as vascular endothelial growth factor (VEGF) and vascular permeability factor (VPF) are responsible for this process and are overexpressed in cancer cells, being two key targets for antiangiogenic treatments [4].

Given the abrupt need for these resources, along with the fast cell proliferation, newly-formed blood vessels usually have wide fenestrations with sizes between 100 and 700nm and badly organized structures, leading to a higher permeability [7]. In addition to this, accumulation of molecules for biosynthesis is potentiated by a poor lymphatic drainage. Both

these observations were given the name enhanced permeability and retention (EPR) effect, and can also be used for the development of new therapies.

Besides VPF and VEGF, other receptors are also overexpressed. Receptors of epidermal growth factor (EGF), folic acid or transferrin, as well as integrins αvß3 or αvß5, are differently expressed in cancer and healthy cells, and therefore can also be beneficial targets for cancer therapies [8]. On the other hand, it is important to mention that healthy cells also express some of these receptors, constituting a disadvantage of this targeting type.

A better bet for cancer cell death is through the process of programmed cell death, scientifically known as apoptosis, that is also observed in non-cancer cells that are not in perfect conditions [9]. During apoptosis regulatory pathways in cancer cells, the mitochondria produces and releases pro-apoptotic factors into the cytosol, such as endonuclease G and cytochrome-c to stimulate the activation of several protein complexes, which will trigger cell death. Several stimuli can induce the mitochondria to produce and release such agents, like ion imbalance with calcium and iron ions, oncogene factors or DNA-damaging factors. Regarding ion imbalance, calcium overload will affect the permeability of the outer membrane of the mitochondria by stimulating the opening of the mitochondrial transition pores, thus contributing to a faster release of pro-apoptotic factors.

1.3 - Breast Cancer

Breast cancer is the most common type of cancer in women, comprising 25% of all cancers. It can be categorized according to the expression of three main receptors, estrogen receptor (ER), progesterone receptor (PR) and human epidermal growth factor receptor 2 (HER2) and can be divided into non-invasive such as ductal carcinoma *in situ* (DCIS), invasive such as invasive lobular carcinoma (ILC) and metastatic breast cancers. Several hormonal therapies are being studied in order to disrupt the effects of progesterone, estrogen and HER2 protein. On the contrary, there is a type of breast cancer called triple negative breast cancer (TNBC) that does not express any of these receptors, corresponding to approximately 20% of the cases [10]. TNBC is considered to be more aggressive, to have poorer prognostics and higher tendencies to recur than other types of breast cancer [11]. It is also the type with higher grade, meaning that TNBC cells are physiologically more different than healthy cells and have an abnormal growth pattern. Statistically, studies proved that 11% of breast cancer patients suffered from TNBC and reported that the five years survival rate is lower than for any other types of breast cancer.

Since hormones are not the triggers for TNBC growth, hormonal therapies will not cause any response in cell growth [12]. Therapies that target HER2 proteins also do not work since HER2 is not expressed in these cells. With this being presented, TNBC is, unarguably, one of the most aggressive types of breast cancer and one of the most difficult to detect and treat, for which new therapies need to be developed.

1.4 - Cancer Diagnostics

The most usual practice for cancer diagnosis throughout the world starts with an appointment with a physician, who detects a possible risk and advises analysis from three categories, body fluids like urine or blood, imaging such as magnetic resonance imaging (MRI), nuclear scanning, ultrasounds or computerized tomography (CT) and biopsies followed by pathological analysis. Body fluids analysis is considered a non-invasive technique but it is still

very limited since it cannot detect every type of cancer. On the contrary, biopsies give more precise diagnosis but are an invasive procedure that requires the prior knowledge of tumour location, leaving imaging as a promising solution since it can be less invasive than biopsies and more accurate than a body fluid analysis. After confirmation, the disease is staged and the best treatment is decided.

In terms of imaging, it is a useful technique for early detection of tumours, especially in the study off deeply-located or small cell masses [13]. The type of imaging technique depends on the organs to be analysed, health, age of the patient and costs. The techniques mentioned before can be based on positron emission, magnetic field, ultrasound application and X-ray emission. Interestingly, in MRI, CT and nuclear imaging, obtained images can be enhanced with the application of contrast agents, such as paramagnetic or superparamagnetic materials, X-ray absorbing materials and pharmaceuticals with radioactivity, respectively.

MRI is a type of nuclear magnetic resonance which consists in the application of a strong magnetic field, between 0.3 and 1.5T, to an organism. A MRI machine is composed by a magnet, a superconductive coil, radiofrequency and gradient coils, receptors and a processing unit. This technique provides images of biological tissues obtained based on the concept of tissue relaxation time (TRT), being this model dependent on the hydrogen atoms of the, abundantly present in every tissue, water molecules [14]. Under a magnetic field, hydrogen atoms align with the field as magnetic dipoles and also absorb and emit specific radio frequencies. The formed gradients enable the mapping of the signal and the selection of the plane to be visualized [13]. When the frequency pulse is shut down these protons re-emit radio waves, at different rates, according to the chemical composition of each tissue. These waves are detected by the reception coil, and then converted into an electrical current which is processed in order to produce a contrast image of the body part or sample.

TRT has two classifications, longitudinal or spin-lattice (T1) and transverse or spin-spin (T2). The first parameter translates the regain of longitudinal z-magnetization, parallel to the external magnetic field, returning to its maximum value which existed prior to the electromagnetic pulse application. It is associated with the loss of energy from the excited hydrogen nuclei to the surrounding atoms, hence its name spin-lattice, and the higher the hydrogen density, the shorter T1 will be. On the contrary, T2 translates the loss of magnetization in the xy-plane, transverse to the vector of the magnetic field [15]. It is associated with dephasing of the spinning dipoles after the application of the electromagnetic pulse, and similarly to T1, the higher the density of hydrogen atoms, the shorter T2 will be.

Other parameters like the repetition time (TR) and the echo time (TE) are crucial in MRI. TR is the time between the application of radiofrequency pulses and TE is the time measured between the instant of application of one radiofrequency pulse and the signal peak detected by the receptor coils. Short TR and TE are associated with T1-weighted image acquisition, tissues with longer T1 relaxation times usually get lower signals in this modality and, therefore, appear darker in the final image, unlike tissues with shorter T1, like fat, which appear lighter. On the other hand, T2-weighted images have long TR and TE, consequently, fluids with low density of hydrogen atoms and longer T2 relaxation times will be the only ones retaining signal, appearing brighter. Logically, owing to its shorter T2 relaxation time, fat will appear darker in the final images.

In the medical field MRI has been proven to be very useful in various medical conditions, among others, like chronic heart diseases, acute tubular necrosis of the kidney, arthritis and cancer. In this last case MRI has already been used to detect tumours in the urinary tract, in the endometrium and in the pancreas. What enables the distinction between cancer tissue and healthy tissue is the differences in the movement of water molecules. With the disorder of the

tumour microenvironment, plus the fast occurring cell proliferation leads to a restriction of water movement to a significant level, which may be detected in certain modalities of MRI, such as diffusion-weighted MRI.

Regarding the ratio of advantages/disadvantages of MRI in comparison to other techniques it has been proven to be positive. MRI enables the choice of a slice of the sample to be analysed, has a remarkable spatial resolution, high sensitivity, is non-invasive and is radiation-free, which is especially relevant for the prevention of mutagenesis and tumour formation. It is also important to emphasize that MRI contrast agents are safer than the ones used in X-rays and CT imaging, which can be nephrotoxic.

1.5 - Cancer Therapies

After the correct diagnosis, the next step is choosing the best therapy to be employed. In cancer treatment there are numerous options, such as surgery in order to excise the tumour mass, chemotherapy, which is employed through the administration of drugs that reduce cell proliferation, radiotherapy, which induces cell death through irradiation with X-rays, hormonal therapy by inhibition of the binding of certain hormones to their receptors, or immunotherapy which consist in the boost of the body natural immune system, using antibodies or T-cells [16]. Additionally, in recent years, the concept of targeted therapy has been explored, which consists in the preferential attack of tumour cells, leaving healthy counterparts unharmed.

In cancer treatment, the ultimate goal is to apply the most effective treatment with the least side effects and the most comfort for the patient in order to assure a satisfactory quality of life [17]. Taking this into account, the treatments and combination of treatments like surgery with radiotherapy or chemotherapy, that are applied nowadays, still cause significant discomfort or side effects. Indeed, non-specific treatments affect every tissue in the body, in the case of chemotherapy, hair follicles, bone marrow cells and cells from the digestive system are heavily affected, causing symptoms like hair loss, anaemia and nausea. Targeted therapies, arisen from these needs and have been developed in order to solve them [18].

For the past years, several drugs were developed and approved to be used in chemotherapy, like cisplatin, paclitaxel and doxorubicin. This last one, is one of the most common drug to be used for the treatment of several types of cancer including breast cancer [19]. It is a lipophilic molecule initially made from the bacteria *Streptomyces peucetius* and it was approved for medical use in 1974 in the United States. This anticancer drug interacts with DNA through intercalation and inhibition of biosynthesis of other molecules, it also inhibits both transcription and replication processes by stopping the progression of topoisomerase II and by linking with this enzyme to prevent the formation of the DNA double helix, respectively [20]. In addition, in some cases, it can increase quinone type free radical production, contributing to an increase in toxicity. However, due to the fault in the targeting of cancer cells and to the need of solving the pharmacokinetics limitations of freely administrated drugs such as fast renal clearance and easy capture by the mononuclear and reticuloendothelial phagocyte systems, attempts have been made to conjugate drugs with monoclonal antibodies or to transport them in nanocarriers.

In terms of antibodies, the first FDA approved monoclonal antibody was Rituximab that has affinity to CD20 antigens [18]. Following this antibody, several naked monoclonal antibodies such as Trastuzumab (Herceptin®) for HER2 overexpressing breast cancers, or antibodies conjugated with other molecules, like Brentuximab vedotin (Adcetris®) for the treatment of Hodgkin lymphoma and anaplastic large cell lymphoma by CD30 antigen targeting, have been produced [21].

Regarding nanocarriers, numerous nanosystems for cancer therapy have been approved by the FDA since the 1990s, being mostly created of polymers, lipids or proteins. Polymer products include Eligard® for prostate cancer (approved in 2002) [22] and Oncaspar® for acute lymphoblastic leukemia (approved in 1994) [23]. For breast cancer Abraxane® was approved in 2005 being lately approved, in 2013, for pancreatic cancer, this one is an example of albumin-bound anticancer drug delivery system, in this case, of paclitaxel [24]. More commonly used are the liposome-based nanosystems, these include DaunoXome® for Kaposi's sarcoma (approved in 1996), LEM-ETU® for breast and stomach cancers (approved in 2006) and Doxil® for ovarian cancer in 2005 and for multiple myeloma in 2008 [25]. In addition to these, new promising drug delivery systems are made every year involving other materials like polysaccharides, metals, ceramics, or a combination of two or more of these.

Besides all the therapies mentioned before, some emerging cancer treatments are being explored, such as hyperthermia and photothermal therapy [26]. This last one consists in the conversion of photon energy into thermal energy in cancer cells, which leads to an increase of temperature and therefore to cell death by heat. The first one has the same concept, causing death by heat, however temperature increase is preferentially caused by a magnetic field, being less harmful to the patient [27]. The energy derived from dipole alignment and posterior relaxation is converted into thermal energy, which is used to create the desired therapeutic effect. Most importantly, both techniques require an intermediate within the tumour microenvironment, preferentially inside tumour cells. For photothermal therapy the most common materials are gold nanoparticles [26], while magnetic materials such as superparamagnetic iron oxide nanoparticles (SPIONs) have been suggested for hyperthermia purposes [28].

Summarizing, targeted cancer therapies are an attractive branch of oncology, being a promising adjuvant treatment when coupled with surgery, since they reduce most problems associated with other treatments, especially chemotherapy.

1.6 - Conclusion

In conclusion to this chapter, cancer is unarguably one of the most threatening medical conditions of the modern days. It can appear in almost every part of the human body, having an outstanding mortality rate all around the world, mostly due to poor diagnosis and treatment. Breast cancer, and specifically triple negative breast cancer, is one of the most problematic types of breast tumours since it does not express any of the common cancer cells receptors, such as HER2, ER and PR, which means it cannot be treated with hormonal therapies that are associated with less side effects, leaving chemo and radiotherapies as the best options.

Chemotherapy is one of the most common evasive therapies used in oncology, unfortunately it can cause severe side effects and it is not always the best option in terms of success rates due to poor drug delivery to the tumour site. With this purpose, several investigations are being done in creating targeted therapies that ensure the correct delivery of the chemotherapeutical drugs into the tumour site. These new therapies are based on the nanometric systems that can carry a chemotherapeutical drug and deliver it, specifically, at the tumour mass. These nanocarriers can be both inorganic and organic and can have physical characteristics such as magnetism that can be used for other cancer therapies like magnetic hyperthermia and as a contrast agent in MRI. Interestingly enough, some of the created nanocarriers have already been approved by FDA and have shown promising results in cancer diagnostics and treatment.

(page intentionally left blank)

Chapter 2

Introduction

New cancer therapies are being studied and developed with the help of nanotechnology. These therapies are based on the creation of small sized carriers that promise to deliver drugs and other molecules into the tumour mass.

In this chapter the importance of nanotechnology in life sciences will be addressed as well as its current applications in the biomedical field. Two main types of nanoparticles, inorganic and polymeric, will be explained in detail, discriminating their characteristics, synthesis techniques and applications. In addition, the biological interaction of these particles will be enlightened, giving a general review of the possibilities for new cancer treatment products.

2.1 - Nanotechnology in Life Sciences

Several fields of science take advantage of nanotechnology in order to develop new products. Areas such as environmental, textiles, electronics and life sciences have benefitted a lot from the excellent properties derived from materials at the nanoscale. Having said that, the general definition for nanoscale is a material with size between 1 and 100 nanometres and just to put it in scale, ten hydrogen atoms can be stacked next to each other and fit them in one nanometer [29]. In sum, nanotechnology is the manipulation of matter to this small scale with the objective to develop useful materials, systems and devices.

In terms of materials development, nanomaterials have several characteristics that can provide better applications than bulk materials, being the surface to volume ratio one of the most relevant [30]. Interaction between materials and other molecules is mediated by the atoms at the surface of the material, in bulk materials atoms are mostly located inside the volume of the material leading to a smaller ratio. In nanosized materials this ratio is higher due to the fact that atoms are mostly located at the surface. In the biological field nanomaterials enable a better interaction with biological systems, due to the match in size. Animal cell sizes usually range between 10000 and 20000nm in diameter, which means that nanosized materials can enter cells, usually by endocytosis and their organelles, enabling a direct interaction with macromolecules such as DNA, proteins and receptors that can also be present outside the cells with which nanomaterials can bind.

In addition, for a better interaction with biological systems these materials can be coated with biological materials such as antibodies or biopolymers, leading to an increase in biocompatibility, creating a combined device with excellent properties to be applied into the biomedical field [31].

2.2 - Nanoparticles in Medicine

In the biomedical field nanoparticles are mostly being studied as nanocarriers for drugs or other molecules, for diagnosis and treatment of several diseases such as viral and fungal infections, diabetes and cancer [32]. In diagnostics, nanoparticles found their use as contrast agents, fluorescent dyes and magnetic materials and as for treatments these downsized materials can be used for targeted drug delivery and for enhancement of drug safety profile [33].

According to several studies, nanoparticles can have magnetic properties and therefore can be used as contrast agents in MRI scanning, which is a very interesting technique for cancer detection, as previously reported [34]. Some metallic nanoparticles have been studied as contrast agents for this type of diagnosis technique, such as iron oxides and gadolinium-based products. These are, respectively, negative and positive contrast agents and enhance contrast in T2 and T1-weighted images in MRI, also respectively. Additionally some of them were already approved by the United States Food and Drug Administration (FDA).

Although gadolinium-based products are more used than iron oxide and magnesium-based products, some studies found that these products were toxic for patients with acute or chronic renal insufficiency, leading to nephrogenic systemic fibrosis and with this, the use of these particles was discontinued in patients with this severe disease [35]. Having said that, the scientific community shifted towards the alternatives. Iron oxides proved to be an interesting category of materials since the human body has a significant percentage of iron ions and several methods and well-defined mechanisms to transport and process them. Several nanosystems using these materials have already been developed and approved, but it is important to emphasize that numerous tests and investigations are still being made since these oxides are not the best in terms of biocompatibility [36]. With this purpose, other materials with higher biocompatibility such as hydroxyapatite-based products are being explored.

Nonetheless, nanoparticles can be composed of different materials with a number of properties that lead to several applications besides cancer diagnosis. Examples of this are quantum dots [37], nanowires [38], carbon nanotubes [39] and dendrimers [40] that can be used as biosensors for HIV and bacterial infections, among others.

Treatment wise, nanoparticles are usually used as drug and other biomolecules delivery systems. As mentioned before, a substantial number of drugs have poor pharmacokinetic behaviour when freely administered, leading to a poor treatment and to the occurrence of undesired side effects [41]. Drugs can be incorporated into a nano-transport system in a wide variety of ways, in order to overcome the poor pharmacokinetics problem, depending on the characteristics of the drug and the features of the used material as a transporter. The drug can be conjugated with proteins, nucleic acids or polymer chains, it can also be incorporated into a biodegradable porous matrix, incorporated into a non-biodegradable matrix and released upon certain stimuli or added to a nanocapsule, that has a hollow compartment, and released later on.

From these carriers, several methods of drug release can be explored. The most common mechanism of release is through stimuli that can be divided into internal and external to the body [42]. External stimuli include, magnetic and electric fields, mechanical stress and ultrasounds or light, usually ultra-violet or near-infrared radiations. Magnetic field is often

combined with magnetic nanoparticles such as iron oxides and gadolinium. These convert electromagnetic energy into thermal energy that can be applied to hyperthermia treatment and for drug release. Some investigators produced a magnetic liposome which released doxorubicin when a magnetic field of 1.5mT was applied [43]. Other studies where performed in the rupture of a poly(allilamine)-magnetite complex to release doxorubicin [44]. Further investigations confirmed that a magnetic field application translates into an increase of 15% in the releasing process when compared to the absence of said stimulus [45]. This method has several advantages since magnetism is biologically safe for the body, however it requires big magnets and specialized technicians to perform the treatment. Also, some magnetic nanoparticles proved to be toxic, with the example of gadolinium based products which limits the range of options.

The use of electric fields is a relatively new technique that is based on polyelectrolyte systems of neutral or positive charge that can be either natural or synthetic. As an example, a team of investigators proved that hyaluronic acid-based gels tend to reversibly shrink under the presence of an electrical stimulus, thus releasing its contents. A current limitation for this stimuli dependent drug release is the presence of natural electrolytes in biological fluids, which affect the good performance of this technique.

Associated with an electrical field application, research has been focusing on piezoelectric materials. A piezoelectric material is characterized by the production of an electrical field when a mechanical force is applied and vice-versa [46]. These materials are being applied to create electro-mechanical micropumps, but they can also be used for electroporation which causes the formation of pores in the cell membrane which can increase drug uptake. An interesting material that is both piezo and pyroelectric and has an excellent biocompatibility is hydroxyapatite. Some studies were performed to evaluate if the piezoelectric effect in bones was generated from collagen fibers or from hydroxyapatite and proved that both express this characteristic.

Another stimulus is temperature. This is a very versatile trigger since it can derive from external actions like magnetic and electric fields that can be converted into thermal energy and from internal temperature, being this last example the most common form of internal stimuli. Since tumour sites tend to present higher temperatures and more acidic environments, contrary to the rest of the body tissues, temperature alongside pH variations can have numerous uses. Several drug delivery systems take use of temperature to perform their functions, possible examples are microgels that in response to temperature contract or distend. Such structures will be explored further on.

After releasing, another crucial factor for drug cellular uptake is a good targeting, illustrated in figure 2.1 [47]. In tumours a passive cell targeting, that does not require any modification to the particle, can seem quite effective due to the high vascularization [48]. However reports show that these systems only have a 0.7% delivery efficiency. With this being said, active targeting seems to be a better option, since it is based on surface modifications of the particle that will interact with receptors at the cell surface [49]. It can be categorized into selective or non-selective targeting depending if it aims at a specific receptor that is characteristic of one cell type, or if it acts on a more common and less specific one. For the specific case of tumour cells there are a group of FDA approved selective targeting models [50].

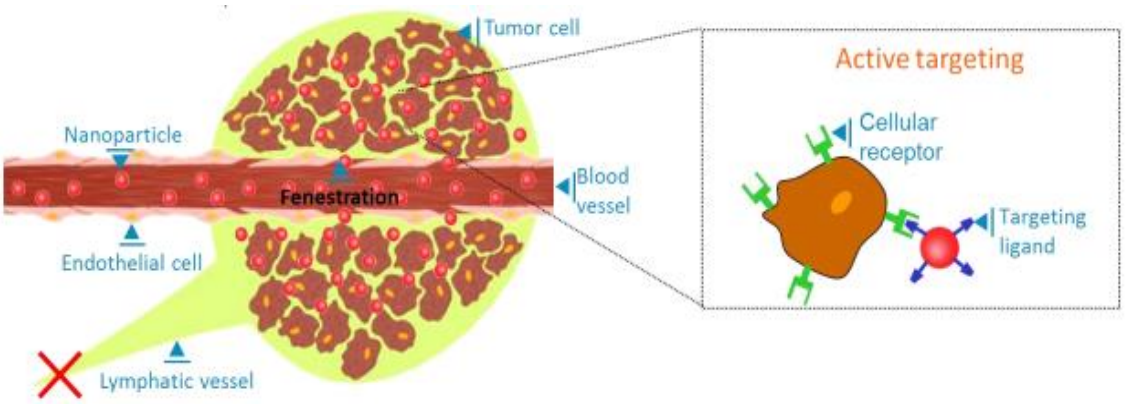

Figure 2.1 - Active vs passive targeting of nanoparticles. Adapted from [47].

These are generally based on antigen-antibody bonds, like trastuzumab, which targets the HER2 receptor in some breast cancers.

When creating a new drug delivery system, factors like ease of production, stability and therapeutic success need to be considered. In terms of targeting, both active and passive strategies are satisfactory, even though the first one provides higher rates of success while the last one is less expensive and easier to produce.

2.3 - Calcium Phosphate Nanoparticles

Calcium phosphates are widely employed in bone tissue engineering, especially hydroxyapatite (HAp) and tricalcium phosphates (TCP) [51]. These materials were introduced as alternatives to bone substitutes with metals like titanium alloys and steel, due to their excellent biocompatibility derived from the similarity with natural bone tissue, and bio and thermodynamic stability at physiological pH. Nonetheless, these materials suffer from poor tensile strength, which can be a problem in tissue engineering, but not in nanotechnology. The main uses of HAp in biomedicine are in dentistry and in bone regeneration [52].

TCP, $Ca_3(PO_4)_2$, can be divided into to three polymorphs, α-TCP, ß-TCP and α'-TCP, being α- and ß-TCP the most common types, formed at higher and lower temperatures, respectively [53]. Both are biodegradable, α-TCP more than ß-TCP and both more easily degradable than HAp. Overall, TCP is FDA-approved and it is often used for a controlled release of antibiotics and proteins, when associated with a polymeric matrix.

Hydroxyapatite is a crystalline mineral that belongs to the calcium orthophosphates group of the apatite family ($A_{10}(BO_4)_6X_2$), with the chemical formula of $Ca_{10}(PO_4)_6(OH)_2$. It has a Ca/P molar ratio of 1.67, a density of 3.16 $g.cm^{-3}$ and a stable pH of 9.5 in an aqueous solution at 25°C [54]. It has a hexagonal structure, in the space group of P6/3mc, and has proved to be both piezo and pyroelectric at the nanoscale as long as it is electrically polar [55]. So far, several methods to synthesize HAp nanoparticles have been explored, such as sol-gel, biomimetic and electro depositions, ultrasonic and dry sprays and combustion processes. Still, wet chemical precipitation has proven to be the most used, due to its simplicity and to the use of environmental friendly solvents [56].

$$5Ca(OH)_2 + 2H_3PO_4 \rightarrow Ca_{10}(PO_4)_6(OH)_2 + 9H_2O \; . \qquad \textbf{(1)}$$

Equation 1 translates the general and the simplest reaction to synthesize HAp. This is made by reacting an alkaline calcium solution with an acidic *ortho*-phosphoric acid solution in an alkaline environment, producing HAp as a solid precipitate and water as a side product. Nonetheless, synthesizing HAp through this method is still very complex, due to the Ca/P molar ratio and pH and temperature conditions that will have influence on particle chemical composition, size and morphology [57]. With this method HAp particles can range from a few nanometres to hundreds of micrometres, can be both spherical and rod shaped and can have secondary phases like α and ß-TCP.

As mentioned before, a possible cancer therapy is based on programmed cell death, apoptosis, induced by a calcium ion imbalance. HAp is mainly composed by calcium, it is biocompatible and biodegradable especially in acidic environments such as tumour microenvironments [58]. All these factors increase calcium ions release and cellular uptake, increasing intracellular ion concentration, thus inducing apoptotic responses. Therefore, HAp can be a possible biomaterial for cancer treatment, nonetheless it can also be a promising material for cancer diagnostics due the possibility to be doped by different ions.

In fact, HAp is one of the best ceramics to induce modifications. The structure and organization of the atoms in the crystalline network enables an easy doping with other ions [59]. Also, in nature, HAp can incorporate almost half of the elements of the periodic table in its atomic structure, depending on temperature and pressure conditions. Of course, in the laboratory, such conditions cannot be simulated, diminishing the wide range of options, regarding synthetic HAp substitutions. Nevertheless, the hexagonal phase of HAp, that is rarely stoichiometric, is the main motif for the facilitated ion substitution. These incorporations can be both anionic and cationic, being carbonate (CO_3^{2-}) ions the most common to integrate the HAp structure, but it can also happen with Chloride (Cl^-), Magnesium (Mg^{2+}), Iron II (Fe^{2+}), Iron III (Fe^{3+}), Fluorine (F^-) and other ions.

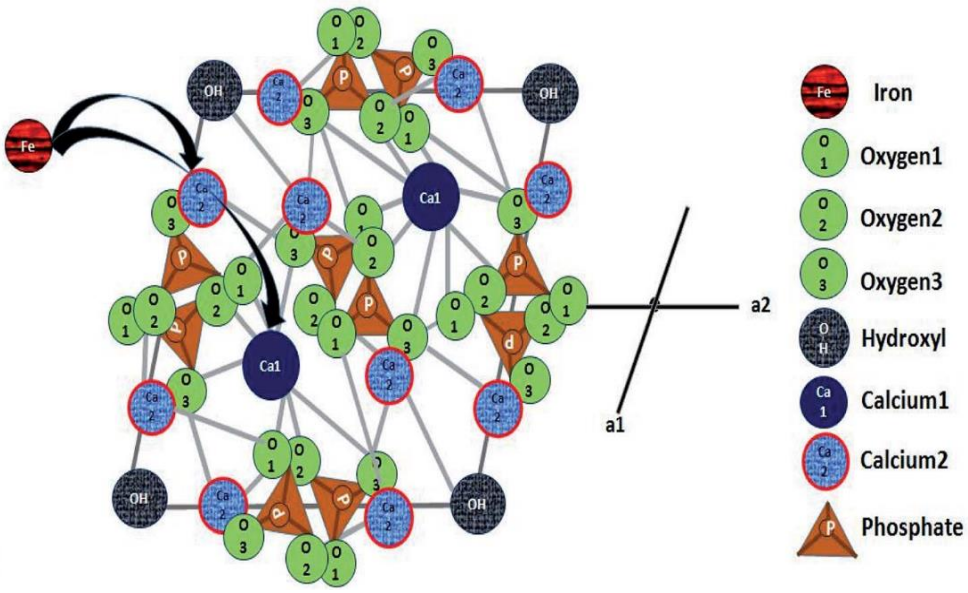

Figure 2.2 – Expanded view of the crystalline structure of hydroxyapatite and iron ion incorporation model. Adapted from [62].

These substitutions can give rise to new properties in the material that can have different applications in biomedicine, like mechanical strength and stability [60]. Some studies confirmed that ions like Fe^{3+} increase the mechanical strength of the material but they can also decrease its stability in a physiological environment, which can be very interesting in terms of ion release. Besides, iron ions can give rise to magnetic assets, which can be applied in the oncology field, for diagnostics with the use of MRI and therapeutics as a mediator for magnetic hyperthermia, as proved by Tampieri et al. due to the superparamagnetic features of these particles [61]. Concerning the method in which the ion incorporation is based , it happens mostly by ion substitution, as illustrated in figure 2.2, where calcium ions can be substituted by iron atoms during synthesis [62]. This can be easily adapted in the wet chemical precipitation method, by adding an iron solution to the calcium solution alongside the phosphoric acid solution, generating an iron doped hydroxyapatite precipitate. A possible reaction is described in equation 2,

$$(10\text{-}x)Ca(NO_3)_2{\cdot}4H_2O + xFe(NO_3)_3{\cdot}9H_2O + 6(NH_4)2HPO_4 \rightarrow Ca_{10\text{-}x}Fe_x(PO_4)_6(OH)_2 + (4+4(10\text{-}x)+9x)H_2O \; . \quad \textbf{(2)}$$

Regarding the electrical properties of HAp, studies showed that this material is both piezo and pyroelectric, characteristics that can be applied for electroporation and for increased biocompatibility [63]. There is a lack of studies regarding doped HAp and its electrical characteristics, nonetheless, Dhal and collaborators studied the effects of tantalum doping percentage on HAp on its polarization and biocompatibility, confirming that the addition of tantalum increased the biocompatibility of the material and that the change in polarization contributed to this factor due the increase in the wettability of the sample [64]. Nevertheless, the effects of doping HAp with iron were never studied to a full extent.

HAp biocompatibility is an important feature of these material for biomedical applications. Even though some studies show that doping HAp with iron does not change these characteristics, other studies such as the one carried out by Laranjeira et al. proved that iron doped HAp can be slightly thrombogenic [65][66]. On the other hand, this slight incompatibility can be compensated with surface modifications or by particle encapsulation in polymeric chains or matrixes.

2.4 - Polymeric Particles

Hydrogels are described as physically restricted hydrophilic polymeric network that can retain a large amount of water or biological fluids [67]. What determines the capability of a hydrogel to absorb and retain water is the presence of hydrophilic groups such as, -OH,-$CONH_2$, -CONH. Regarding the formation of the network, this is made by the formation of covalent crosslinks which can be imagined as a chain of atoms that are capable of joining at least two polymeric chains together [68]. These covalent bonds provide additional control, integrity and maintain the structure of the gel while the swelling and shrinking processes occur in aqueous medium and also provide a favourable environment to encapsulate guest molecules.

The structure characteristics will determine the gels properties to undergo a phase transition from a swollen liquid-like hydrated state to a solid-like collapsed state in response to an external stimuli such as ionic strength, molecule concentration, magnetic field, pH or

temperature, among others [69]. The volume changes are highly dependent on the solvent, the type of monomers and the interactions between the groups of the side chains of the different monomers and with the solvent. Hydrogels can be described as cationic [70], anionic [71], neutral and amphiphilic or zwitterisonic, depending on the origin of the incorporated functional groups. Another way to designate these gels is based in size, with macrogels being gels that have a size distribution between one millimetre and several centimetres, while microgels rage from 100 nanometres to several hundred microns. Microgels are found to be of great interest due to their high surface area and small size, and also by enabling controlled and regulated applications due to their environmentally responsive behaviour.

Generally, microgels are composed of a covalently crosslinked, porous spherical network of randomly oriented polymeric chains that are swollen in a suitable solvent. Microgels morphology appears as a spherical sponge due to the crosslinked linear chain structure with a narrow particle size range.

Regarding how microgels are classified, there are three general ways [71]. The first classification is relative to the type of functional groups incorporated into the network, leading to charge related classifications. The second classification is based on the responsive behaviour of the microgels, which can be stimuli-responsive or non-responsive. Where in case of non-responsive behaviour, gels swell in response to water absorption while stimuli-responsive microgels swell in response to external environmental changes like pH or temperature, as mentioned before. There is also a category for multi-responsive microgels that, as the name describes, are sensitive to multiple stimuli and can have different responses accrue to the different combinations of stimuli. For the second classification, microgels are sorted by the nature of the crosslinks in the network, in which microgels can be chemically or physically crosslinked [72]. Chemical crosslinking refers to covalently linked monomers that are highly stable and can maintain the structure of the polymer when submitted to environmental changes. This type of crosslinking is mainly generated by copolymerization of monomers with a multifunctional crosslinker that can lead to different properties, morphology and size distribution according to the percentage of crosslinker. The most common method to synthesize these microgels is through radical or condensation polymerizations. On the subject of physically crosslinked microgels, these are stabilized by non-covalent interactions such as hydrophobic and ionic interactions as well as hydrogen bonds. Since these interactions are weaker that covalent bonding, this type of crosslink gives rise to less stable microgels when compared to their chemically-linked counterparts. Nonetheless, these microgels can have useful applications in the biomedical field, like drug and protein encapsulation, since they can release their incorporated agents through dissolution of their own structure. Another important characteristic derived from this is the easier biodegradation process, since it is easier to break the crosslinked gel into monomers, which can be interesting for injectable microgels, in order to generate less cytotoxicity.

As previously mentioned, microgels that have a stable structure and a well-defined morphology tend to be well dispersed in solution, creating a stable colloidal suspension that can lead to several applications in diverse fields of science and engineering. In addition, these microgels mimic some characteristics of natural tissues due to their high content in water and also tend to be biocompatible, creating new biomedical opportunities and applications, e.g. in wound dressing, catheters, biosensors and drug delivery systems.

For these applications to work, a crucial factor is the stability of the microgel suspension, meaning the capability to avoid the formation of aggregates [73]. This phenomenon is controlled by the balance between attractive and repulse forces, creating a potential between microgel particles that is usually attributed to Van der Waals forces which induce strong short-

range isotropic attractions and electrostatic repulsive forces. However some polymers do not tend to be electrostatically stable, like microgels synthesised by some emulsification processes, and for these a surface modification with polymeric chains, like poly ethylene glycol, that causes an adverse entropy between the chains of different particles, can be a solution.

In the last years, several methods to synthetize microgels have been studied and optimized. One of the most used and maybe one of the simplest is the free-radical polymerization method, nevertheless, other methods such as atom transfer radical polymerization or reversible addition-fragmentation chain-transfer polymerization can also be employed. In the free-radical method the predominant process of polymerization is by continuous addictions [74]. The monomers used in this synthesis are usually alkenes or functionally substituted alkenes, where the most common and thermodynamically favoured chemical transformations are addiction reactions.

Radical polymerization is a step-by-step process with the following stages, initiation, propagation and termination. In the initiation step, radical compounds are formed by an initiator that usually is a peroxide or an azo compound. Formation of a radicals can happen through thermal decomposition, where a covalent bond is homolytically cleaved to form two radicals. Nevertheless, there are other ways to form radicals, either through photolysis, redox reactions, ionizing radiation, electrolysis or even sonication. In the second step, the name derives from the fact that the polymeric network is expanding, through the formation of new bonds between chains as explained before. As the radical initiator is formed, it attacks the carbon-carbon double bond of the monomer, this double bound is a sigma bond that holds a pair of electrons in a very stable manner, while other electrons are more loosely held by a pi bond. The radical uses one of the electrons of this bond to form a more stable link with the carbon atom, while the other electron returns to the second carbon atom, turning the whole molecule into a radical, enabling itself to proceed with the polymerization without the need of more initiator. This seems as a positive feedback process since there is always the formation of radicals in each propagation, and it could happen if there are impurities in the system, polymerizations like these where given the name of living polymerizations. On the other hand, the most common occurrence is a termination step that eliminates every radical species from the system. This step can happen through several methods, but the most usual is by combination of two radicals to form a covalent bond. Different from the free radical polymerization there are other ways to form microgels without the need to form radicals.

With this characteristics and several ways to synthesise microgels, the interest for applications in biomedicine increases, as mentioned above. As previously described, drug delivery systems are the solution to many problems in actual biomedicine, since these systems deliver their content in a specific region according to certain stimuli, enabling the possibility to inject substances into the body without harming non-targeted tissues. In the case of cancer, the stimuli that can be explored are temperature and pH. As already explained, tumours have an acidic (pH<6) environment when compared to healthy cells and also a higher temperature (~40°C). With this information it is possible to create a microgel system that will respond to these changes and adjust its structure in order to release its contents, and for this, the choice of monomers that constitute the microgel is crucial. The monomers must be sensitive to temperature and pH when polymerized and for the temperature sensitive characteristic N-isopropylacrylamide (NIPAM) is one possible example. NIPAM is a water soluble monomer with the molecular formula of $C_6H_{11}NO$ that can be easily polymerized, by the free radical method due to a carbon double bond, to form Poly (N-isopripylacrylamide) (PNIPAM) [75]. When polymerized it is possible to obtain thermosensitive microgels with a reversible lower critical solution temperature (LCST) phase transition from a swollen liquid-like hydrated state to a

shrunken solid-like dehydrated state at 32°C, losing about 90% of its volume [76]. Considering the LCST of PNIPAM and the application of the microgel, this value should be higher, closer to 40°C, and for that purpose, the idea of a copolymer could solve the problem. A copolymer is described as a polymeric chain composed of different monomers, resulting in a system with the characteristics or a mixture of features from each monomer. With the finality to increase the LCST of PNIPAM a monomer with a higher LCST when polymerized should be incorporated into the microgel.

Dimethylaminoethyl methacrylate (DMAEMA) is a cationic, water soluble monomer with the molecular formula of $C_7H_{13}NO_2$ that has a pKa of 7.5. Depending on the ratios it is possible to polymerize NIPAM and DMAEMA together to form a copolymer with the desired LCST [77]. This methacrylate monomer is also known for its pH responsivity, due to a tertiary amine that is easily protonated in acidic environments. Also, the fact that DMAEMA is a cationic monomer, allowed it to be applied in different studies for gene delivery. On the other hand, some studies tried to polymerize NIPAM and DMAEMA together, in order to get a final LCST of 40°C, and in the process it was found that the pH-responsivity was easily overrun by the temperature sensitivity of NIPAM due to the small amounts of DMAEMA added to the system. Another possible monomer for this purpose is 3-dimethylaminopropyl methacrylamide (DMAPMA) that is very similar to DMAEMA, maintaining the pH-sensitivity feature. Olga et al. successfully created a copolymer of NIPAM-DMAPMA with both thermal and pH sensitivity [78]. This team also explained that the polymerization was easier with the use of DMAPMA when compared to DMAEMA, producing more reproducible results.

These smart materials have a wide potential as delivery systems. One of the methods for the administration of these materials is the intravenous process. One of its associated problems, besides the size of the injected materials that should be lower than 200nm in order to avoid thrombus formations, is the activation of the immunological response to an external body. This problem can be corrected by the functionalization of the materials with certain hydrophilic molecules like Poly(ethylene glycol) methacrylate (PEGMA) that is one of the possible modifications of Poly(ethylene glycol) (PEG) [79]. It consists of a polymeric chain of variable size with the addition of a methacrylate group, while maintaining the OH^- termination. Several studies related to PEGMA are being made, but regarding its application on microgels it is still relatively unexplored.

PEG, on the other hand, is widely known due to its characteristics regarding immunological responses [80]. It is FDA approved and it is not only used in medicine but also in cosmetics and pharmaceuticals. In drug delivery systems, it is used as particle coating to stabilize suspensions and to increase particle half-life. PEGylated surfaces have a high affinity to albumin, a very abundant protein in the blood system, avoiding the opsonisation process to occur and therefor avoid an immunological response. Due to these properties the modification of PEG to form PEGMA creates the possibility to covalently link this monomer to a matrix, maintaining its properties.

2.5 Nanoparticle Pharmacokinetics and Biodistribution

When designing a biomedical system at the nanoscale, pharmacokinetic and biodistribution analysis are of great importance [81]. Pharmacokinetics comprises a set of parameters known as ADMET evaluation, which stands for: administration routes, distribution, metabolism, excretion and toxicity.

Administration routes can be divided into two categories, enteral or parental. Enteral are all the routes associated with the gastrointestinal system, including sublingual, buccal or rectal. On the other hand, parenteral routes include intravenous, intramuscular, transdermal or inhalatory, among others. The most common option is oral administration due to its simplicity and slow release, nonetheless, administrated drugs must be exposed to the enterohepatic system and suffer metabolism-induced reactions, affecting nanoparticle functionality and bioavailability. Also it is important to point out that nanoparticles will be exposed to different pH values, susceptive particles to degradation at low pH and pH-sensitive systems are not adequate for this administration route. The ideal alternative to these circumstances is intravenous administration, leading to high bioavailability, fast response and easy access to the tumour area when applied as a cancer therapy. However, some disadvantages include the need of skilled medical staff for application and the need for sterilization.

After administration, for the intravenous route, nanoparticle biodistribution through the body is the next parameter to be evaluated. In the blood circulatory system, opsonisation is a process in which serum proteins, such as opsonins, bind to hydrophilic structures. These proteins are responsible for the activation of the reticuloendothelial system. This tends to reduce the half-time and the mean resident time, while increasing the value associated with clearance. Hydrophobic particles and drugs are more resistant to protein binding, thus having higher half-life and mean resident time and lower clearance.

The next step in nanoparticle action in the body is metabolic processing. This happens after cellular uptake in different organs, such as liver, spleen and kidneys. This uptake will depend on particle size and shape, where particles with less than 10nm are not immediately eliminated and elongated shapes tend to penetrate better [82]. Metabolic process can be a step-by-step reaction starting by cell intake mediated by proteins, redox reactions performed by cytochromes, conjugation with polar groups for an easier extraction and cell efflux mediated by glycoproteins such as ATP-binding cassette proteins [83].

Excretion is considered the last step, it mostly happens at renal level but it can also happen through perspiration or exhalation. Once again size takes an important role in this process. Particles with less than 5.5nm are almost immediately cleared at the renal level. Larger particles, between 5 and 200nm suffer hepatic clearance. Above 300nm, particles are retained in the spleen by red pulp macrophages and suffer splenic clearance. Nonetheless, structures with this size or above can cause embolisms and therefore their administration is never advised.

A lack of clearance can lead to a bioaccumulation problem and cause different levels of toxicity, which is defined by the ability to cause harm to the organism. Several inorganic particles such as iron oxides and gadolinium-based tend to accumulate in the kidneys and can cause serious conditions as explained above. Particle characteristics are of major importance in terms of toxicity. Bigger and less spherical particles tend to be more toxic, while negatively charged particles tend to be less toxic in comparison to their cationic counterparts, probably due to repulsion forces created by the negatively charged membrane of cells. Particle composition is also a main impact factor, where inorganic particles are more toxic due to ion imbalance caused in cells.

In conclusion, when studying a nanodelivery system or any pharmacological system the ADMET evaluation parameters should be taken into account. It should be performed very carefully using correct biological models in order to establish correct criteria for the application purpose.

2.6 Conclusion

Nanoparticles, unarguably, prove to be a promising solution for cancer diagnosis and treatment, due to the wide range of materials, shapes and structures that these particles can take. These small sized materials provide new properties, with great advantages when compared to bulk materials, such as a facilitated interaction with biological tissues. Nanoparticles in the biomedical field can be used as biosensors, biomarkers and gene and drug delivery devices, among others, ensuring to be less toxic, more effective and easier to eliminate from the organism, mainly due to their small size and wide range of materials.

In the past years, nanotechnology has been highly explored. In the biomedical field, properties such as magnetism, piezoelectricity, drug delivery and others, offer good solutions for several severe medical conditions. In the specific case of cancer, magnetic nanoparticles are being studied as MRI contrast agents with less toxicity as well as substrates for hyperthermic therapy. Hydroxyapatite, since it is highly biocompatibility and mainly composed by calcium ions may be an excellent material to introduce into the human body. However in its nanometric form, when internalized by cells, it can induce an ion imbalance that leads to cell death by apoptosis, being a useful material in cancer treatment. In addition, this calcium phosphate can be easily doped with iron ions to create magnetic assets.

Finally, drug delivery systems can be the future in terms of better cancer diagnosis and treatment, since drugs and contrast agents can be introduced in the tumour site without damaging healthy tissues. With this aim, several combinations of polymeric carriers are being explored, with characteristics such as temperature and pH responsiveness, with the main objective to deliver their content in the warmer and more acidic tumour environment.

2.7 Aim

In recent years, the concept of theranostics has been highly studied. This new concept is proposed as a conjugation between therapeutics and diagnostics into one unitary system. Advances in materials science unveiled great potential in biomedical applications using materials never thought to be employed in medicine. In fact, with resort to several scientific adaptations, biomedical and biopharmaceutical research have offered novel and highly creative solutions for injury and disease treatment as well as general drug delivery.

The main purpose of this project was to develop a multifunctional composite at the nanoscale with potential to be employed in both cancer treatment and diagnosis. With this objective, iron doped hydroxyapatite (Fe-HAp) nanoparticles were synthesised via the chemical precipitation method, being analysed in terms of size, surface charge, morphology, chemical composition, crystallinity and both electric and magnetic properties. Further on, the toxic effects of these nanoparticles were evaluated on cancer cell lines of TNBC and also in primary cultures of fibroblasts. Next, thermo-responsive microgels composed by a core of P(NIPAM-co-DMAEMA) and an outer shell of P(NIPAM-co-PEGMA) were synthesized by the free radical polymerization route and further characterized in terms of size, surface charge, thermoresponsivity, morphology and chemical composition. Finally, encapsulation of the ceramic nanoparticles into the core of the microgel was attempted, alongside with the encapsulation of the hydrophobic chemotherapeutical drug doxorubicin.

This final small sized composite, represented in figure 2.3, should provide a less toxic and more specific cancer treatment. Tumour biological characteristics, such as the mass higher temperature, were explored in order to develop an internally triggered drug release. When

properly tuned, nanocarriers with a LCST between 38 and 40°C would release most of their load above these temperatures, mostly inside the tumour microenvironment. Additionally, due to the EPR effect, these particles would tend to accumulate in such regions.

Additionally, Fe-HAp nanoparticles, when internalised by cells, calcium release contributes to membrane damage and possible apoptosis induction, while iron release can increase reactive oxygen species formation (ROS). In general terms, when internalized by cancer cells, Fe-HAp nanoparticles can be characterized as toxicity-inducing agents.

With both piezoelectric and superparamagnetic properties, Fe-HAp may also be employed

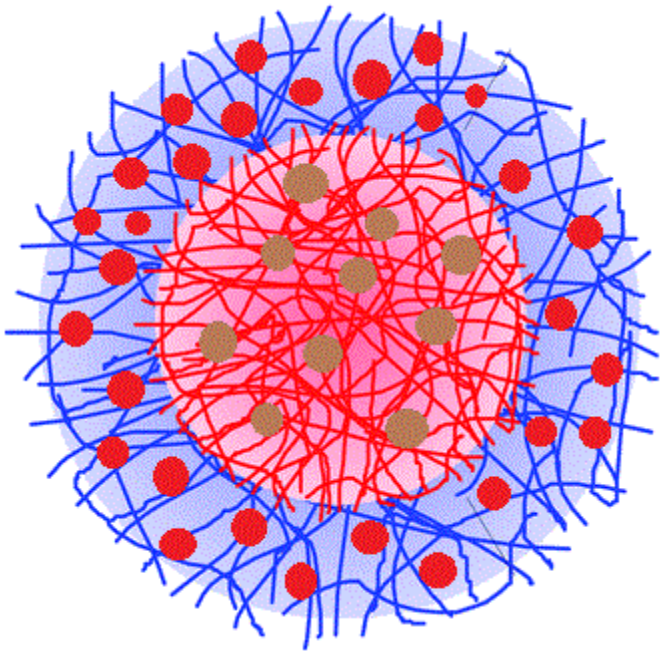

Figure 2.3 – Representation of the final composite. The core-shell structure is composed by a P(NIPAM-co-DMAEMA) core (red matrix) and a P(NIPAM-co-PEGMA) shell (blue matrix). In the core Fe-HAp nanoparticles (brown dots) are encapsulated while doxorubicin (red dots) is encapsulated mainly in the shell.

as media for electroporation and magnetic hyperthermia for cancer treatment, alongside with the potential to be used as a T2-weighted contrast agent in MRI. Finally, when encapsulated into the microgels, the polymer matrix will provide protection against degradation while traveling in the bloodstream and also ensure the correct delivery at the tumour site.

This work, alongside with advances in medicine, molecular biology and nanotechnology, will hopefully provide new diagnostic techniques and new therapies with less side effects and better results for cancer treatment. Additionally, the high variability of nanocarriers and nanoparticles is expected to take part in this process and in the development of the concept of personalized medicine.

(page intentionally left blank)

Chapter 3

Materials and Methods

3.1 Materials

For the synthesis of the ceramic nanoparticles, calcium hydroxide (98%), iron III nitrate (98+%) and phosphoric acid (85% in water) were purchased from Acros Organics, USA, while ammonium hydroxide (25%) was obtained from MERCK, Germany.

For the synthesis of the polymeric microgels, N-(isopropylacrylamide) (NIPAM, 97%), N,N'-methylenebis(acrylamide) (Bis, 99%), 2-(dimethylamino)ethyl methacrylate (DMAEMA), poly(ethylene glycol) methacrylate (PEGMA, average Mn 500) and ammonium persulfate (APS, >97%) were purchased from Sigma-Aldrich, Germany. The initiator 2,2′-Azobis(2-methylpropionamidine) dihydrochloride (AAPH, 97%) was obtained from Acros Organics, USA.

Sodium citrate tribasic dihydrate (SDS, >99.0%), hexadecyltrimethylammonium bromide (CTAB, >99%) and doxorubicin hydrochloride (DOX, 98.0-100.0%) were purchased from Sigma-Aldrich, Germany. 3-(Trimethoxysilyl)propyl methacrylate (MPS, 98%) was obtained from Acros Organics, USA.

Cell lines of triple negative breast cancer were purchased from ATCC (USA) and cultured in 96-well cell culture plates with D-MEM medium (Gibco, Germany) containing fetal bovine serum (FBS, Gibco, USA) and a penicillin/streptomycin solution (Biowest, France). Primary cultures of human gingival fibroblasts were purchased from Sciencell (USA) and cultured in 96-well cell culture plates with α-MEM medium (Sigma, Germany) containing fetal bovine serum (FBS, Gibco, USA), a penicillin/streptomycin solution (Biowest, France).

All chemicals were used as bought without any purification step and all the synthesis were performed using ultrapure water with a resistivity of 18.2MΩ.

3.2 Ceramic Nanoparticles Synthesis

3.2.1 Hydroxyapatite Nanoparticles Synthesis

Undoped hydroxyapatite nanoparticles were synthesized through the chemical precipitation method. Briefly, a 0.5M calcium hydroxide solution was prepared and heated at 100ºC in an oil bath under vigorous magnetic stirring. Into this solution, a previously prepared 0.3M orthophosphoric acid solution was added dropwise at a rate of 0.500mL/min using a peristaltic pump (ISMATEC-ISM795C, Germany). The pH of the solution was continuously measured and kept above 9.5 by adding ammonium hydroxide as needed. After the acid addition, the reaction was kept under the same conditions, as an aging process, for 2 hours. After cooling down to room temperature the nanoparticles were washed three times, with ultrapure water, by

centrifuging at 15.000 rpm (Beckman Avanti J25 XP, UK) and dried at 60°C in a laboratory oven (Heraeus, Germany). The dried powder was grinded in an agate mortar and pestle and half the produced amount was sintered at 1000°C for one hour, with a heating rate of 5°C/min. Finally, both the non-sintered and the sintered powders were stored in a desiccator.

3.2.2 Fe^{3+} Doped Hydroxyapatite Nanoparticles Synthesis

The synthesis of iron doped hydroxyapatite nanoparticles was performed through the same method as the undoped nanoparticles with slight changes. Briefly, into a 0.5M calcium hydroxide solution, solutions of 0.1M iron(III) nitrate and 0.6M orthophosphoric acid were added dropwise at the same time at a fixed rate of 0.500mL/min using a peristaltic pump. The aging, washing, drying, grinding and sintering processes were the same as for the undoped samples as well as the storage method.

3.3 Ceramic Nanoparticles Characterization

3.3.1 Size and Surface Charge

Particle hydrodynamic diameter was measured through dynamic light scattering (DLS) and surface charge measurements were obtained through zeta potential analysis. Both were performed in a Zetasizer Nano ZS (MALVERN, UK) with a scattering angle of 173° and a He-Ne 633nm wavelength laser. The measurements were performed at i3S, Porto. For a better dispersion, 1mg of the dried particles was dispersed in a 10mg/mL solution of sodium citrate tribasic that will act as a surfactant, and sonicated twice in 15 minutes intervals using a Vibra CellTM probe sonicator (Sonics&Materials Inc., USA). Afterwards, the suspension was diluted 10 times in ultrapure water before analysis. Three size and zeta potential measurements were done per sample at 25°C.

3.3.2 Chemical Profile

In order to determine the chemical composition of the samples Fourier-Transform Infrared Spectroscopy (FTIR) and Raman Spectroscopy (RAMAN) were the two chosen techniques. FTIR was performed in a Perkin-Elmer 2000 (Perkin-Elmer, USA) with a $4cm^{-1}$ spectral resolution and the spectra were obtained after averaging of 32 scans. RAMAN was performed in a Raman confocal spectrometer InVia Qontor (Renishaw, UK) with a He-Ne laser of 514.5nm wavelength and a spectral resolution of $0.15cm^{-1}$. FTIR measurements were done at i3S, Porto, while RAMAN was performed at IFIMUP, Porto.

For FTIR, approximately 2mg of the ceramic powders were mixed with 200mg of potassium bromide and compressed (8 Tons) in a hydraulic press (Grasedy Specac, UK). Pellets were produced in a low humidity environment to improve samples quality.

For RAMAN spectroscopy, a small amount of the ceramic nanoparticles was placed on a glass substrate. Several grain regions were analysed with different optimization parameters, namely the laser attenuation and acquisition times.

3.3.3 Thermogravimetric Analysis

The thermal behaviour of the non-sintered HAp and Fe-HAp powders was studied by thermal gravimetric analysis (TGA) using a NETZSCH STA 449F3 (NETZSCH, Germany). The program used an oxygen environment and involved a one minute initial temperature of 25°C, followed by a 5°C/min slope up to 1200°C. The analysis were performed at ISEP, Porto.

3.3.4 Crystallinity

Crystalline phase characterization was performed using of X-ray diffraction (XRD) in a EMPYREAN diffractometer (Malvern Panalytical, UK), within a 2θ range from 6° to 70° at every 0.026° using CuKα1 radiation with a wavelength of λ=1.5406 Å, generated at 45kV and 40mA. A comparative analysis was made based in the JCPDS database of the International Centre for Diffraction Data. The analysis was performed on the dry powders at CICECO, Aveiro.

3.3.5 Size and Morphology

For a deeper study of the nanoparticles size and morphology, Transmission Electron Microscopy (TEM) was employed in a JEOL JEM-1400 electron microscope (JEOL Ltd., Japan), operating at an accelerating voltage of 120kV. Images were obtained using a CCD digital camera Orius 1100W (Gatan, USA) and further analysed with ImageJ® software (University of Wisconsin, USA). This analysis was performed at i3S, Porto.

The samples were prepared by dispersing the ceramic powders in an aqueous solution of sodium citrate 10mg/mL followed by two 15 minute cycles of sonication in a Vibra CellTM probe sonicator (Sonics&Materials Inc., USA). Also, the dispersed samples were diluted by adding 100µL of the suspension to 1mL of ultrapure water. A 10µL drop was then loaded onto a Formvar/carbon film-coated nickel mesh grid (Electron Microscopy Sciences, USA) overnight in order to let the solvent evaporate.

3.3.6 Ferroelectric Properties

Macroscopic ferroelectricity measurements were made by using the conventional Sawyer-Tower P-E loop plotter, following the circuit represented in figure 3.1. For this, 400mg of non-sintered powders were compressed (10MPa) into 1.5mm, in diameter, disks in a hydraulic press (Talleres Mestraitua, Spain). Half of the produced disks were sintered in the same conditions used for powder sintering, as mentioned in section 3.2. The samples were then polished with sand paper (P4000) until a smooth surface was obtained. The samples were tested by using gold electrodes, on both faces, that were sputtered using a Leica EM ACE200 (Leica, UK), working at 60mA in an argon atmosphere, 50mm from the sample and with a deposition time of 80 seconds. The gold deposition was made at UPTEC, Porto, while the ferroelectric measurements where performed at IFIMUP, Porto.

The samples were then analysed, at room temperature, with the conditions expressed in table 3.1. Several combinations were tested, but the ones presented gave the best results.

Table 3.1 – Measurement conditions to evaluate ferroelectric properties of the samples.

Sample	**Voltage** (V)	**Frequency** (Hz)	**C** (nF)	**R** (kΩ)
HAp	300	1.1	100	100
HAp Sint.	300	1.1	10	3600
FeHAp	300	1.1	10	350
FeHAp Sint.	1000	1.1	10	50

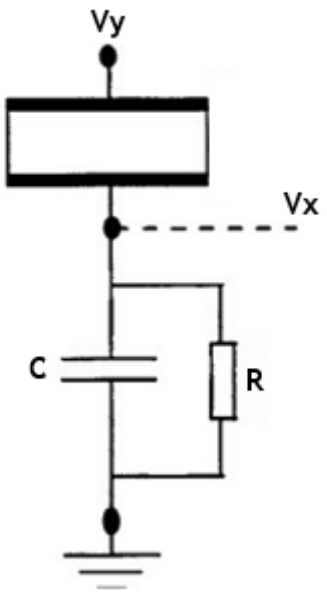

Figure 3.1 – Schematic of a common Sawyer-Tower circuit. Values for C and R are represented in table 3.1.

3.3.7 Piezoelectric Properties

Piezoresponse force microscopy (PFM) was performed using a scanning probe microscope NT-MDT Solver Next, equipped with internal lock-in amplifiers and through the respective Nova_Px 3.4.0 interface software. All PFM and spectroscopy studies were performed out-of-resonance (21kHz), in order to decrease electrostatic responses with correspondent topographic crosstalk. Commercial conductive Pt coated silicon probes (NT-MDT) were used, with curvature radius of 10nm, resonance frequency of ~130kHz and spring constant of 3N/m. The topographic, piezo-response amplitude and phase images were edited via the WSxM 5.0 8.0 software. The measurements where performed at CICECO, Aveiro. The samples were prepared in the same way as for the measurement of the ferroelectric properties in section 3.3.6.

3.3.8 Magnetic Properties

The magnetization of the ceramic iron-doped nanoparticles was studied in a Physical Property Measurement System at a temperature of 300K, with a magnetic field range from -30kOe to 30kOe. The strength of the magnetic moment is presented as a mass magnetization (M), corresponding to the magnetic moment per total mass of the sample. The measurements were performed at Imperial College London, United Kingdom.

3.3.9 Contrast Agent Potential

In order to evaluate the potential of the sintered iron-doped samples for contrast enhancement in Magnetic Resonance Imaging (MRI) several percentages of iron where tested. The measurements were performed using a 3T clinical scanner (Sigma HDXT 3T, GE Health Care, USA) and the analysis was performed at IPO, Porto.

For this tests, the synthesis of the Fe-HAp samples from section 3.2.2, was adapted to accommodate 20, 30, 40, and 50% of iron. The sintered powders were weighted and dispersed in ultrapure water at the following particle densities, 100, 250, 500, 1000, 5000 and 10000µg/mL. T2 contrast images were recorded by pulse sequence technique with TR/TE=4.8/1.3, FGR 30, EC 1/1 and band width 31.2Hz. In order to confirm the chemical composition of these samples a XRD analysis was carried out by repeating the methods in section 3.3.4. Additionally, in order to quantify the iron percentage, inductive coupled plasma spectroscopy (ICP) was performed on the sintered samples.

3.4 Cell cultures

3.4.1 Effects of Non-doped and Iron Doped Hydroxyapatite Sintered Nanoparticles on Breast Cancer Cells

Triple negative breast cancer cells (MDA-MB-468) were cultured in Dulbecco's Modified Eagle Medium (D-MEM) supplemented with 10% (v/v) fetal bovine serum and 1% (v/v) penicillin/streptomycin and incubated at 37ºC at 5% CO_2. Trypsinization and seeding were performed every three days.

3.4.1.1 Metabolic Activity Evaluation

The metabolic activity of MDA-MB-468 cells in contact with the sintered HAp and Fe-HAp nanoparticles was assessed by the resazurin assay. Briefly, metabolically active cells can reduce the blue compound resazurin into resorufin, turning it into a pink-purple appearance that can be detected by spectrophotometry. For this assay, the cells were trypsinized and seeded onto 96-well plates at a density of 5000 cells per well and incubated for 24h. In parallel, ceramic nanoparticles were sterilized in absolute ethanol, washed with PBS and then re-dispersed in complete supplemented D-MEM culture at a density of 2mg/mL. After 24h incubation, regular medium was exchanged for the nanoparticle-rich medium, at the density of 125, 250 and 500 µg/mL, and the cells were again incubated at 37ºC and 5% CO_2. At timepoints of 24 and 48 hours of incubation, each well was loaded with resazurin and re-incubated for 4 hours. The medium was then transferred to a black 96-well plate with transparent bottom and fluorescence was

measured at excitation and emission wavelengths of 566 and 605nm, respectively, in a SynergyMX fluorimeter (BioTek, USA). This analysis was performed at i3S, Porto.

3.4.1.2 Live-Dead Assay

In order to evaluate the efficacy of the ceramic nanoparticles to induce cell death, a conventional live-death assay was chosen. Briefly, cancer cells were seeded onto 96-well plates at a density of 5000 cells/well and incubated for 24h at 37°C and 5% CO_2. After incubation, ethanol sterilized HAp and Fe-HAp nanoparticles were dispersed in complete D-MEM and added to the wells at the following densities, 125, 250 and 500µg/mL, and finally the cells were again incubated at 37°C and 5% CO_2. At timepoints of 24 and 48h hours of incubation, each well was loaded with a 2µM solution of calcein AM for 20 minutes at 37°C, followed by the addition of a 3µM solution of propidium iodide for 5 minutes at room temperature, both prepared in PBS. The wells were washed with PBS and fluorescence was analysed under an Axiovert 200M inverted fluorescence microscope (Zeiss, Germany) at an objective magnification of 10x under a multidimensional acquisition mode of GFP and Cys 3.5 channels. Images were obtained at i3S, Porto.

3.4.1.3 Morphology Evaluation

Cells morphology was also assessed after 24 and 48h contact with the sterilized nanoceramics. Briefly, cells were seeded onto a 96-well plate at a density of 5000 cells per well and incubated at 37ºC and 5% CO_2 for 24h. After each timepoint, the wells were washed with PBS and fixed with 4% paraformaldehyde (PFA) solution. After washing 3 times with PBS, the cells were permeabilized with 0.2%(v/v) Triton-X in PBS for 10 minutes while shaking at 50rpm in an orbital shaker. After washing again with PBS, cells were incubated with 1wt% BSA in PBS for 30 minutes while shaking at 50rpm for protein blockage. Next, cells were incubated with AlexaFluor® 488 phalloidin (ThermoFisher, USA) (diluted 100 times in the 1wt% BSA in PBS solution) for 20 minutes stirring at 50rpm in an orbital shaker in dark conditions. After rinsing 3 times with PBS cells were incubated with DAPI in PBS at a concentration of 0.1µg/mL for 10 minutes under stirring at 50rpm in an orbital shaker. Finally, the cells were rinsed 3 more times with PBS and their fluorescence was analysed under an Axiovert 200M inverted fluorescence microscope (Zeiss, Germany) at an objective magnification of 10x under a multidimensional acquisition mode of DAPI and AlexaFluor® 488 channels. Images were obtained at i3S, Porto.

3.4.1.3 Nanoparticle Internalization and Cell Damage Evaluation

Cells were treated, in T75 culture flasks, with several concentrations of HAP and Fe-HAp sintered nanoparticles (125, 250 and 500 µm/mL), incubated at 37°C and 5% CO_2 for 24 h, similar procedure was used for setting up the control without any ceramic nanoparticles. All plates were washed with PBS and cells were collected by trypsinization. The cells were fixed with 2.5% glutaraldehyde mixed with 2% paraformaldehyde in 0.1M sodium calcodylate for 1h, post-fixed with 1% osmic tetraoxide prepared in 0.1M calcodylate buffer, dehydrated in graded ethanol, embedded in Epon 812 mixture and cut into ultrathin sections (~60 nm) on an Ultramicrotome, PT RMC PowerTome PC=XL (Boeckeler Instruments, USA). Sections were single

stained with uranyl acetate and lead citrate. The cells were observed under TEM (JEOL-JEM-1400, Japan) at 120kV. Images were obtained at i3S, Porto.

3.4.2 Effects of Non-doped and Iron Doped Hydroxyapatite Sintered Nanoparticles on Fibroblasts

Human gingival fibroblasts cells (HGF) were cultured in Alpha Modified Eagle Medium (α-MEM) supplemented with 10% (v/v) fetal bovine serum and 1% (v/v) penicillin/streptomycin and incubated at 37ºC and 5% CO_2. Trypsinization and seeding was performed every three days.

Every evaluation assays done for the cancer cells in section 3.4.1, with the exception of the ones in sections 3.4.1.2 (Morphology Evaluation) and 3.4.1.3 (Nanoparticle Internalization and Cell Damage Evaluation), were repeated, under the same conditions, for the fibroblasts using α-MEM instead of D-MEM.

3.5 Polymeric Microgels Synthesis

3.5.1 Poly(N-Isopropylacrylamide) Microgels Synthesis

Microgels of P(NIPAM) were synthesized through the free radical polymerization method. Briefly, 0.100mL of a 20% SDS solution, 0.025g of Bis and 0.700g of NIPAM, were mixed and dissolved in 40mL of ultrapure water in a 250mL three-neck round bottom flask. This solution was then heated to 70°C in an oil bath and then purged with nitrogen for 20 minutes, while stirring at 300rpm on a magnetic plate. In parallel, a 0.014M solution of APS was prepared by dissolving the required amount of initiator in 10mL of ultrapure water and equally purged with nitrogen for 15 minutes.

The solution turned opalescent in the first minutes and later became white, with a milky appearance. After 3 hours at the specified conditions, the reaction was cooled down to room temperature and centrifuged trice at 35000rpm in a Beckman Optima L80-XP ultracentrifuge (Beckman, USA) in 2 hour cycles, for removal of unreacted monomers. The pellet was re-suspended in ultrapure water between washings and stored at room temperature for further characterization.

3.5.2 Core Microgels Synthesis

Core microgels of P(NIPAM-co-DMAEMA) were synthesized via free radical polymerization. Briefly, 0.005g of CTAB, 60µL of DMAEMA, 0.01g of Bis and 0.250g of NIPAM, were mixed and dissolved in 40mL of ultrapure water in a 250mL three-neck round bottom flask. This solution was then heated to 75°C in an oil bath and then purged with nitrogen for 20 minutes, while stirring at 300rpm on a magnetic plate. In parallel, a 0.0037M solution of AAPH was prepared by dissolving the required amount of initiator in 10mL of ultrapure water and equally purged with nitrogen for 15 minutes.

The solution turned cloudy in the first minutes and later became white, with a milky appearance. After 6 hours at the specified conditions, the reaction was cooled down to room temperature and dialyzed using SnakeSkin™ Dialysis bags (Thermo Scientific, USA) against

deionized water for 3 full days, for removal of unreacted monomers. The washed suspension was stored at room temperature for further characterization.

3.5.3 Shell Microgels Synthesis

Shell microgels of P(NIPAM-co-PEGMA) were synthesized via free radical polymerization. Briefly, 0.017mL of a 20% SDS solution, 0.025mL of PEGMA, 0.02g of Bis and 0.325g of NIPAM, were mixed and dissolved in 40mL of ultrapure water in a 250mL three-neck round bottom flask. This solution was then heated to 75°C in an oil bath and then purged with nitrogen for 20 minutes, while stirring at 300rpm on a magnetic plate. In parallel, a 0.0066M solution of APS was prepared by dissolving the required amount of initiator in 10mL of ultrapure water and equally purged with nitrogen for 15 minutes.

The solution turned opalescent in the first minutes and later became white, with a milky appearance. After 6 hours at the specified conditions, the reaction was cooled down to room temperature and centrifuged three times at 35000rpm in a Beckman Optima L80-XP ultracentrifuge (Beckman, USA) in 2 hour cycles, for removal of unreacted monomers. The pellet was re-suspended in ultrapure water between washings and stored at room temperature for further characterization.

3.5.4 Core-Shell Microgels Synthesis

Core-shell microgels of P(NIPAM-co-DMAEMA)-P(NIPAM-co-PEGMA) were synthesized via free radical polymerization. Briefly, 0.020g of a 20% SDS solution, 0.075mL of PEGMA, 0.020g of Bis, 0.486g of NIPAM and 0.015g of APS were dissolved in 80mL of ultrapure water. This solution was purged with nitrogen for 30 minutes at room temperature while stirring at 300rpm on a magnetic plate. Simultaneously, 20mL of the previously synthesized core particles were heated at 75°C and purged right after with nitrogen for 10 minutes, while stirring at 300 rpm in a 250mL three-neck round bottom flask. Then, the monomer solution was slowly added to the core suspension in parcels, starting by a 30mL addition, followed by 10mL additions in 5 minute intervals. The suspension was then purged again with nitrogen, for 10 minutes, to ensure a proper inert atmosphere.

The solution turned opalescent in the first minutes and later became white, with a milky appearance. After 6 hours at the specified conditions, , the reaction was cooled down to room temperature and centrifuged trice at 35000rpm in a Beckman Optima L80-XP ultracentrifuge (Beckman, USA) in 2 hour cycles, for removal of unreacted monomers. The pellet was resuspended in ultrapure water between washings and stored at room temperature for further characterization.

3.6 Polymeric Microgels Characterization

3.6.1 Size, Surface Charge and Temperature Responsiveness

Size, zeta potential and temperature responsiveness were evaluated by DLS in a Malvern ZetaSizer Nano ZS (Malvern, UK), comprising a He-Ne 633nm wavelength laser with a scattering angle of 173°. For size and temperature responsiveness evaluation, the hydrodynamic radius was studied at different temperatures, from 25°C to 50°C with a heating step of 5°C. Three measurements were done per sample, size, surface charge and per temperature, with an equilibration time of 120 seconds between temperature points. The measurements were performed at i3S, Porto.

The samples preparation was carried out by diluting 200µL of the microgel suspension in 1mL of ultrapure water.

3.6.2 Chemical Profile

Microgels chemical profile was evaluated by attenuated total reflectance Fourier transformed infrared (ATR-FTIR) spectroscopy in a Perkin-Elmer 2000 (Perkin-Elmer, USA) with a 4cm^{-1} spectral resolution. This measurements were performed at i3s, Porto, Portugal and spectra were obtain by an averaging of 32 scans.

A small drop of washed particles in ultrapure water was let to dry on the detector surface and then the measurement was run.

3.6.3 Morphology

Microgels shape was assessed by transmission electron microscopy (TEM) in a JEOL JEM-1400 Electron Microscope (JEOL Ltd., Tokyo, Japan) with an accelerating voltage of 120kV and a CCD digital camera Orious 1100W (Gatan, Japan), similarly to the ceramic nanoparticles. The analysis were performed at i3S, Porto. The samples were prepared by diluting 75µL of the washed microgels in 1mL of ultrapure water. A 10µL drop was then loaded onto a Formvar/carbon film-coated nickel mesh grid (Electron Microscopy Sciences, Hatfield, USA) for 30 seconds, after which excess liquid was removed with filter paper.

3.7 Ceramic Nanoparticle Encapsulation Into Core Microgels

Two different protocols were tested to encapsulate the sintered Fe-HAp into the core microgels. The first one was done by using the ceramic nanoparticles as seeds, on which the microgels can polymerize. The second protocol is a more specific process of polymerization, for which the surface of the inorganic nanoparticles was chemically functionalized with a methacrylate group.

3.7.1 Non-specific Seed Mediated Encapsulation

For the first protocol 10mg of sintered Fe-HAp nanoparticles were dispersed in 10mL of ultrapure water by sonication (Sonics&Materials Inc., USA) in two 15 minute cycles in ice to avoid solvent evaporation. In parallel, the protocol from section 3.4.2, to synthesize the core microgels was replicated and after the nitrogen purges the ceramic nanoparticles suspension was added to the monomer solution in the 250mL three neck round bottom flask, which was purged again with nitrogen for 10 minutes to ensure an inert atmosphere. Finally, the AAPH

initiator solution was added and the reaction was continued at 75°C for 6 hours. The suspension turned milky white with a slight orange undertone derived from the Fe-HAp nanoparticles. After the reaction ended it was let to cool down to room temperature and the suspension was stored.

This final composite was then coated with a shell of NIPAM-co-PEGMA, using the protocol for the core-shell microgel synthesis, described in section 3.4.4, prior to the washing steps to avoid ceramic nanoparticles deposition.

3.7.2 Methacrylate Specific Encapsulation

3.7.2.1 Iron Doped Hydroxyapatite Surface Functionalization

In order to modify the surface of the Fe-HAP nanoparticles, 3-(Trimethoxysilyl)propyl methacrylate was used. This coupling agent is a silica precursor with a terminal methacrylate group. A direct reaction between the nanoparticles and the coupling agent occurred, where the silane groups connect to the hydroxyl groups of hydroxyapatite, through a series of hydrolysis and condensation steps.

Briefly, 50mg of sintered Fe-HAP nanoparticles were dispersed in 20mL of ultrapure water through a 20 minutes sonication cycle (Sonics&Materials Inc., USA). In parallel, 3mL of the coupling agent were diluted in 80mL of pure ethanol and heated in an oil bath at 74°C in a 100mL round bottom flask and stirred at 400rpm. Finally the nanoparticle suspension was slowly added into the ethanol solution and was let to react for 4 hours.

The now functionalized nanoparticles were cooled to room temperature and washed twice with ultrapure water and once with pure ethanol by centrifuging at 25000rpm (Beckman Avanti J-26 XP, UK). The pellet was dried at 50ºC (Heraeus, Germany) in a Petri dish and stored in a desiccator for further use.

In order to ensure the correct functionalization of the ceramic nanoparticles with the methacrylate group a FTIR analysis was carried out. With this objective, the protocol, presented in section 3.3.2, for characterizing the chemical profile of the non-functionalized ceramic nanoparticles was reproduced.

3.7.2.2 Functionalized Ceramic Nanoparticle Encapsulation

With the objective to establish a polymer layer around the nanoparticles, the protocol presented in section 3.7.1 for the non-specific encapsulation was employed with slight changes. Briefly, 5mg of the functionalized nanoparticles were used and the CTAB quantity was increased to 0.010g, the rest of the protocol kept the same quantities. The washing and storage methods also remained unchanged.

3.7.3 Ceramic Polymeric Composites Characterization

The composites synthetized from the two protocols were characterized by ultrastructural imaging using TEM. The main objective was to assess ceramic nanoparticle incorporation by the microgels and for this, a small drop of the washed composites was loaded onto a Formvar/carbon film-coated nickel mesh grid (Electron Microscopy Sciences, Hatfield, USA) for 30 seconds, after which excess liquid was removed with filter paper. The analysis was performed at i3S, Porto.

3.8 Loading of Doxorubicin onto Core-shell Microgels

For the loading of doxorubicin (DOX) into the core-shell microgels, a solution of 0.6mg/mL doxorubicin in PBS was prepared. After dissolving the drug, dried core-shell microgels were re-dispersed to a concentration of 5mg/mL. The suspensions were then shaken in an orbital shaker at 4ºC overnight and, after confirming that the microgels were well dispersed, gel filtration was carried out using disposable columns loaded with Sephadex® G-25 gel (GE Healthcare, USA) with a molecular weight cut-off of 25kDa.

As a preliminary test, 0.5mL of the drug/microgel sample were loaded into the column and eluted with 6mL PBS over 1.5 days. The non-encapsulated DOX aliquot was analysed using a Synergy MX fluorimeter (BioTek, USA) at excitation and emission wavelengths of 470nm and 590nm, respectively. PBS was used as blank and a standard curve of DOX was obtained with the following concentrations: 50 – 20 - 10 - 5µg/mL. The quantification was followed by calculations of the encapsulation efficiency (EE) and drug loading capacity (LC) percentages according to Equations 3 and 4,

$$\boldsymbol{EE}\ (\%) = (\boldsymbol{Mi}-\boldsymbol{Mn})/\boldsymbol{Mi}*\mathbf{100} \quad (3)$$

$$\boldsymbol{LC}\ (\%) = (\boldsymbol{Mi}-\boldsymbol{Mn})/\boldsymbol{M\mu}*\mathbf{100}. \quad (4)$$

In these equations, *Mi* represents the initial DOX mass in solution, *Mn* represents the non-encapsulated DOX mass in solution, and *Mµ* represents the total microgel mass in solution.

3.9 Statistical Analysis

Statistical analysis and graphs were carried out with the GraphPad Prism 5 software (GraphPad, USA) and OriginPro 2018b (OriginLab, USA).

Data are represented as mean ± standard deviation (SD). Polymer LCST was analysed through Bolsean-Sigmoidal fits. Statistical analysis was performed using the analysis of variance two-way ANOVA, all for conditions with n=6. Statistical significance was considered when $p<0.05$ and represented with * or # for $p<0.05$, ** or ## for $p<0.01$ and *** or ### for $p<0.001$.

(page intentionally left blank)

Chapter 4

Results and Discussion

4.1 Characterization of Ceramic Nanoparticles

4.1.1 Size, Surface Charge and Morphology Characterization

As previously mentioned, size, surface charge and shape of nanoparticles play major roles in cellular uptake and cellular responses. For this reason, characterization of biomaterials is of extreme relevance in order to predict their behaviour in *in vivo* assays.

It has been previously reported that hydroxyapatite nanoparticles produced by the wet chemical precipitation method can have a wide range of sizes, from a few nanometers to few micrometers. Surfactants play a significant role in terms of controlling the nanoparticles size distribution or just to help their stabilization in aqueous solvents. However, introducing surfactants during the synthesis process may influence the doping process of HAp nanoparticles. Having said that, surfactants such as sodium citrate are commonly used to stabilize and to separate agglomerates afore analysis. From the DLS analysis, HAp nanoparticles had hydrodynamic diameters around 132nm±1.82 and Fe-HAp nanoparticles hydrodynamic diameters of 168nm±1.11, while in TEM HAp nanoparticles showed a length of 50nm and a width of 15nm and regarding Fe-HAp nanoparticles length ranged from 50-140nm while width stayed at 15nm. Regarding the sintered nanoparticles, from DLS HAp nanoparticles had hydrodynamic diameters of 197nm±13.2 and Fe-HAp nanoparticles presented hydrodynamic diameters of 219nm±16.02, while in TEM they had a mean size of 122nm±52.1 for HAp samples and of 98.4nm±55.07 for Fe-HAp. Besides the stabilization effects of sodium citrate, verified by the low polydispersity index (table 4.1), the formation of agglomerates was clearly shown in TEM images. Such occurrence serves as an explanation for the difference between sizes obtained from the two techniques. Nonetheless, these differences were expected since TEM provides real representative images of the nanoparticles, for which DLS can only give an estimate. However, the hydrodynamic diameter obtained from DLS gives a better idea about the nanoparticles behaviour in aqueous solutions, which is of major importance when designing injectable systems, in order to prevent thrombus formations in the circulatory system.

Table 4.1 -Hydrodynamic size, polydispersity index, surface charge measurements and sizes obtained from TEM of the samples stabilized with sodium citrate at a weight ratio of 1, at 25ºC. Results are presented as mean ± standard deviation (n=3).

Sample	**Hydrodynamic size** (nm)	**Pdi** (a.u)	**Zeta Potential** (mV)	**Size obtained by TEM** (nm)
HAp	132±1.82	0.14±0.02	-33.7±0.1	50/15
HAp Sintered	197±13.2	0.22±0.03	-35±1.12	122±52.1
Fe-HAp	168±1.11	0.42±0.06	-29.8±0.75	50-140/15
Fe-HAp Sintered	219±16.02	0.27±0.01	-45±1.31	98.4±55.07

Besides size, nanoparticle surface charge will condition cellular interaction. Animal cells have a negatively charged surface due to the negative charged phospholipids that constitute the cell membrane. As previously explained, negative charged nanoparticles are less toxic and tend to be less internalized, in comparison to their positive counterparts, due to the repulsive forces between cell membranes and the nanoparticles surface. From the Zeta potential analysis, all samples presented a negative surface charge, also influenced by the charge imposed by the negative charged citrate molecules used to stabilize the particles. Nevertheless, HAp and FeHAp nanoparticles have a negative surface charge due to the negative hydroxyl groups that are present in their structure that will be shown further on, in the chemical characterization section. In general, stable colloidal suspensions have a zeta potential greater than 30mV in modulus, preventing particle deposition and therefore increasing shelf-life.

Shape wise, nanoparticles can adopt several morphologies, such as spheres, rods, star shaped among others and hydroxyapatite nanoparticles are no exception. The morphology of

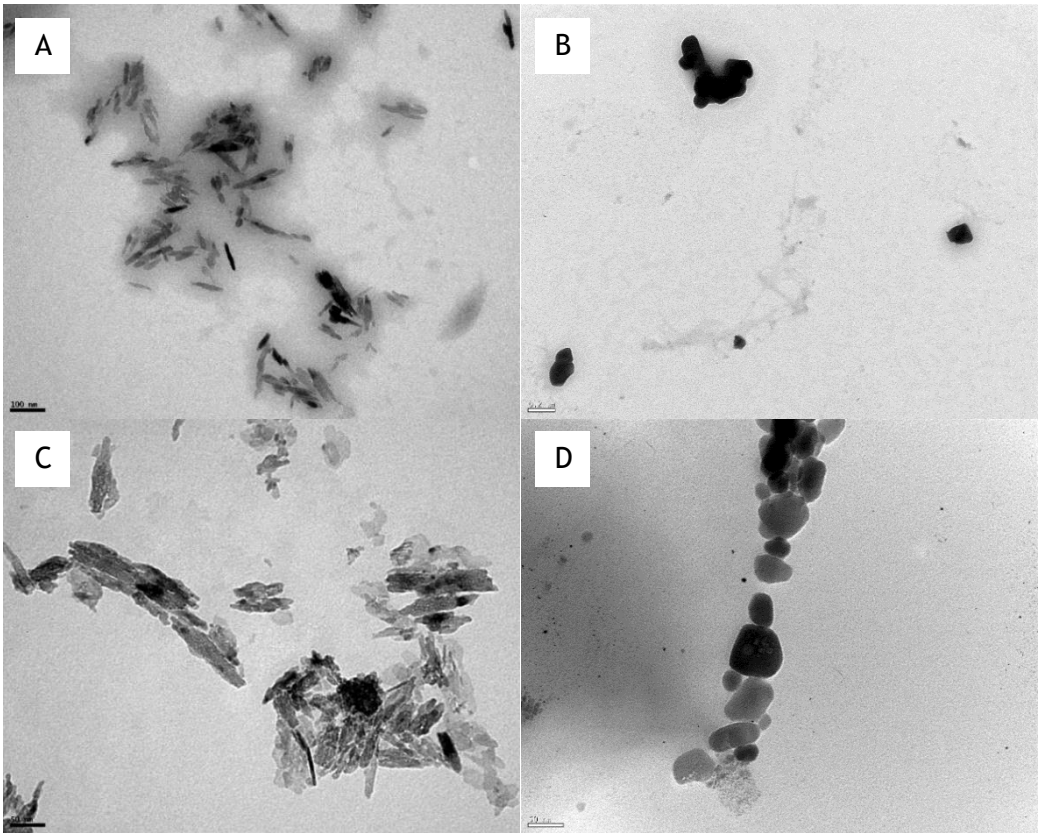

Figure 4.1 – Representative TEM images of the nanoceramics. A-HAp, B-Sintered HAp, C-Fe-HAp, D-Sintered Fe-HAp. Scale bars: 100nm (A); 200nm (B); 50nm (C,D).

nanoparticles is determined by the synthesis process and in the case of hydroxyapatite temperature and pH play a major role. Kumar et al. reported that, through the wet chemical precipitation route, HAp nanoparticles synthesized at higher temperatures and pH~10 adopt a rod-like shape, while higher pH and lower temperatures seem to lead to rounder particles. The produced nanoparticles, shown in figure 4.1, had a rod-like shape that corresponded to the expected, since they were produced at 100°C with a pH~10, however, with the sintering process, morphology changed and spherical nanoparticles could be obtained, probably due to fusion of nanoparticles and their domains. This characteristic has a massive influence in cell uptake, where sharper nanoparticles tend to be easily uptaken by cells, in comparison to spheres. However, encapsulation of these nanoparticles into microgels can be more difficult since the surface area is smaller at the rod extremities [84].

Summing up, DLS and TEM gave different results for the ceramic nanoparticle samples. In suspension the nanoparticles proved to be relatively stable, with sizes below 200nm, with the addition of sodium citrate. The particles proved to be adequate for intravenous administration due to their size (<200nm), negative surface charge and morphology. However, in order to control and obtain a more homogenous size range, synthesis conditions should be optimized in terms of temperature control, which could be done by using bioreactors. Other methods of synthesis could also be explored and one example is microfluidics, where size is mainly controlled by the size of the device itself. Besides these characteristics, when biomedical devices are being developed the chemical composition of the materials is a major concern, since it may limit the application for which the nanoparticles are employable.

4.1.2 Chemical Profile

Nanoparticles can be produced with different materials or even a combination of several materials. Such compositions give rise to different properties that can be very useful depending on the application.

Hydroxyapatite is calcium orthophosphate and, as the name describes, is mainly composed by phosphate, calcium and hydroxyl groups, however during synthesis some impurities can appear as well as secondary phases [66]. FTIR and RAMAN are two powerful techniques that when combined give a very solid proof of the chemical composition of the samples.

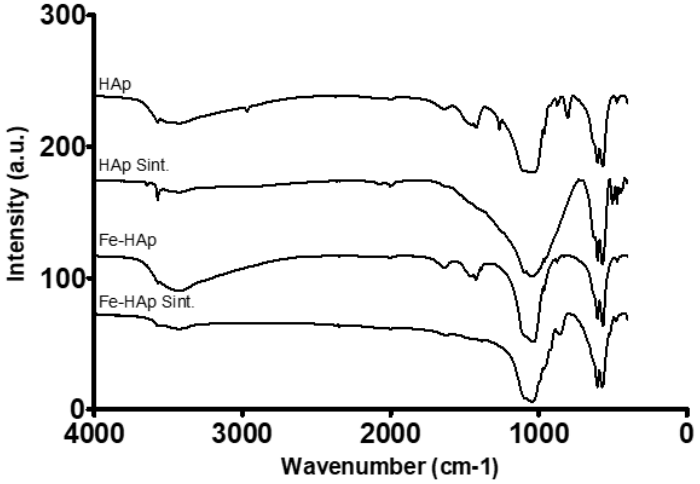

Figure 4.2 - Fourier transform infrared spectra of sintered (Sint.) and non-sintered hydroxyapatite (HAp) and iron-doped hydroxyapatite (Fe-HAp). Vertical offset was adjusted for individual curve analysis. One measurement per sample was performed.

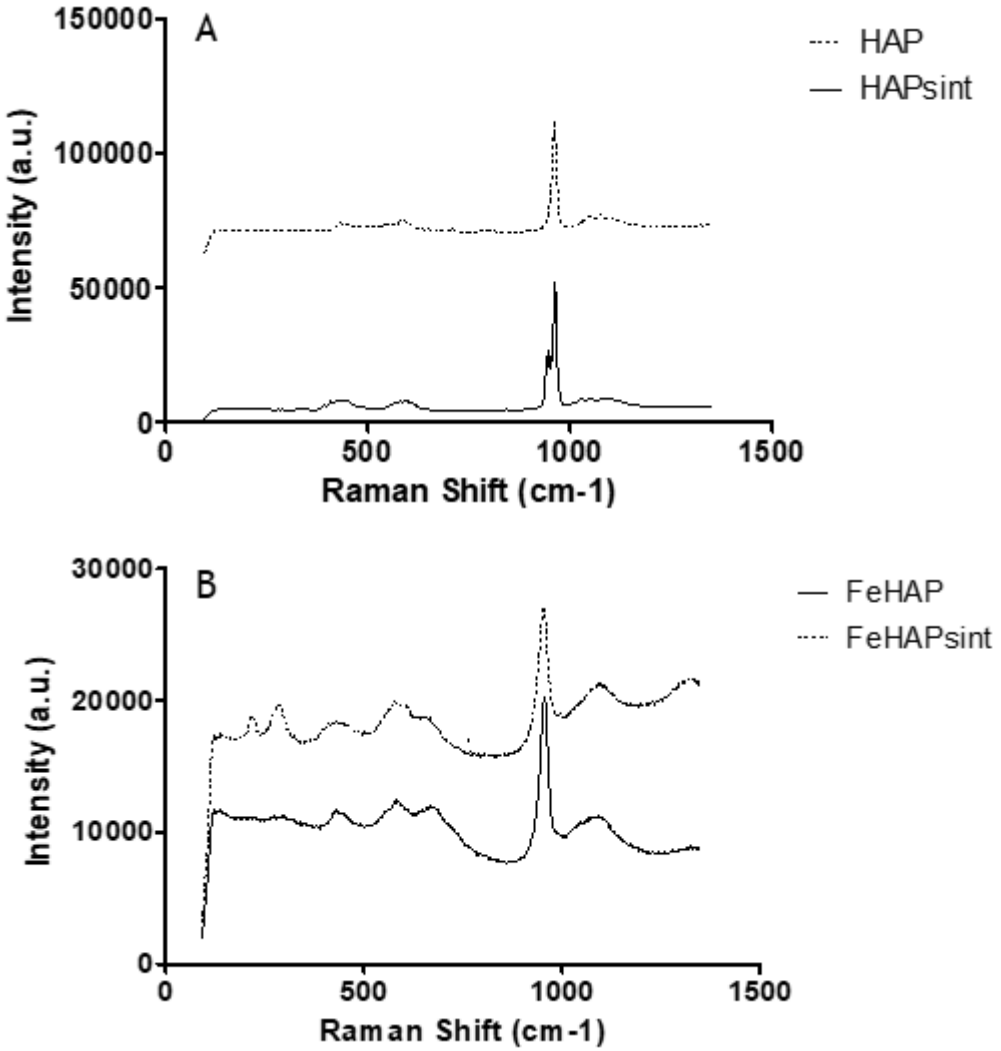

Figure 4.3 - Raman spectra of sintered and non-sintered HAp (A) and Fe-HAp (B) samples. Vertical offset was adjusted for individual curve analysis. One measurement per sample was performed.

In the FTIR analysis, figure 4.2, the spectra corresponding to hydroxyapatite O-H stretching can be found at ~3570cm^{-1} in all samples, although very faint in the iron-doped material, and the vibrational O-H peak at 634cm^{-1} can only be found in sintered HAp. A broad band and a noticeable peak associated with water are found in all samples at ~3435cm^{-1} and ~1635cm^{-1}. Residual carbonates incorporated from CO_2 can be found at ~1470 cm^{-1}, ~1421cm^{-1} and at ~874cm^{-1} in the non-sintered samples. Lastly, the four modes of PO_4^{3-} can be detected for all samples. The v1 mode can be detected at ~961cm^{-1}, although more faintly in Fe-HAp samples; the v2 mode may be seen at ~470cm^{-1}; the v3 mode can be observed at ~1035cm^{-1} and ~1090cm^{-1}, more easily in the sintered samples than in the non-sintered material, with no distinguishable third peak at 1110cm^{-1} in any of the samples; and the v4 mode can be very clearly observed at ~565cm^{-1} and ~603cm^{-1} in all samples.

From the analysis, it is possible to conclude that all samples are in fact calcium phosphates with hydroxyl groups, as expected for hydroxyapatite. It is also possible to assess that carbonate impurities are more present in non-sintered samples, due to the fact that the heat treatment consolidates the lattice and creates a less porous structure with less capability to incorporate CO_2 and associated to this, carbonate groups tend do degrade at higher temperatures, which is

confirmed in the TGA analysis that is presented further on [85]. Water is also very present in non-sintered samples, derived not only from the weakly dried state but also from atmospheric incorporations when the KBr pellet was being produced. Regarding the Fe-HAp samples, the iron components of the sample cannot be detected using FTIR and for this reason RAMAN was performed.

The RAMAN analysis, seen in figure 4.3A, for HAp samples confirmed what was already obtained with the FTIR analysis. In the spectra all the vibrational groups of phosphate are present, with peaks dividing in the sintered sample due to higher crystallinity [86]. Regarding the Fe-HAp samples, represented in figure 4.3B, new formations could be detected at 670cm^{-1} in the non-sintered sample, which correspond to iron oxide formations of magnetite. In the sintered counterpart the magnetite peaks could also be detected, with the addition of its secondary phases of hematite at 216 and 288cm^{-1}, derived from the heat treatment.

In sum, all samples appear to be calcium phosphates, with iron-doped samples having additional iron oxide portions, most likely magnetite and/or hematite. Depending on the size of these phases, their presence may bring interesting magnetic properties, especially superparamagnetism, conferring potential for T2 contrast imaging in MRI and also for hyperthermia treatments.

4.1.3 Thermogravimetric Analysis

With the objective to understand the effects of the sintering process on the samples, a thermogravimetric analysis was carried out. From figure 4.4, both HAp and Fe-HAp samples presented two major slope changes, one at ~110°C and the other at ~700°C, showing a loss of mass as a function of temperature increase. The first slope change was attributed to adsorbed water evaporation, while the second was due to carbonate impurities degradation [87]. Such mass losses were confirmed by the FTIR analysis, where the peaks attributed to water and carbonate impurities were less intense in the sintered samples. It is also important to mention that if the sintering temperature was raised above the 1200°C, thermal decomposition of the hydroxyapatite structure could possible happen, showing that the chosen sintering temperature

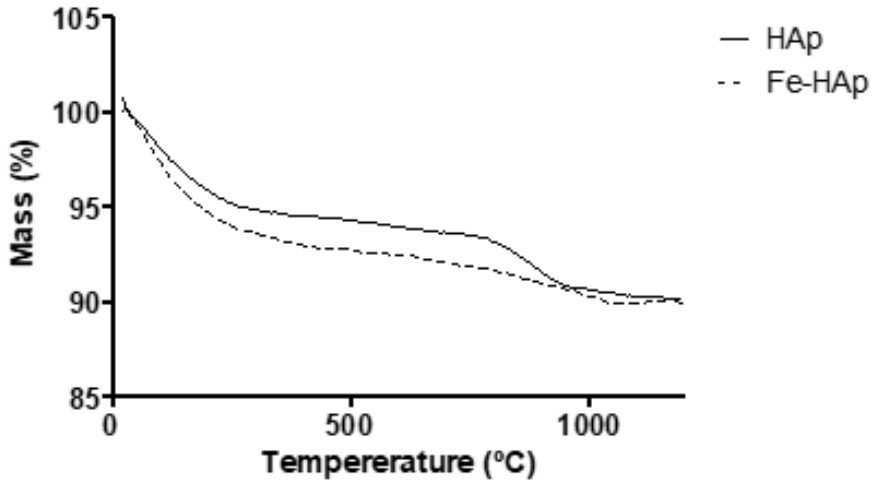

Figure 4.4 – Thermogravimetric analysis of both non-sintered HAp and Fe-HAp samples. Curves are represented in order and according to the legend. One measurement per samples was performed.

of 1000°C was a good stop mark. Interestingly, both samples presented the same mass loss ~9%, showing that iron incorporation did not affect the sample overall thermal stability [88].

4.1.4 Crystallinity

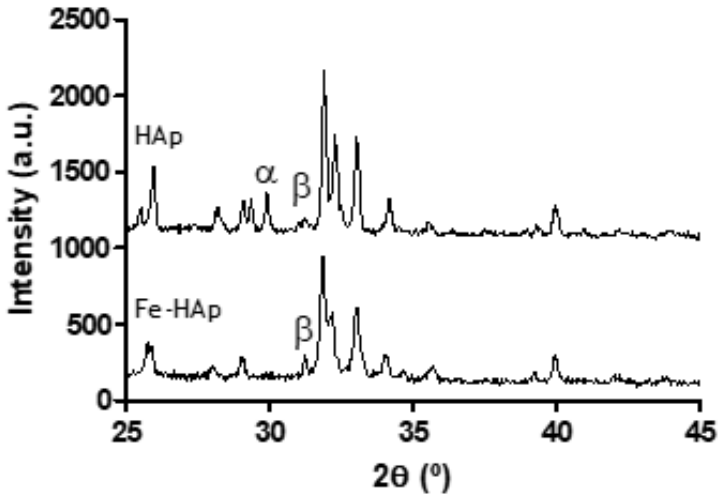

Figure 4.5 – XRD difractograms of HAp and Fe-HAp samples. Peaks marked with α and ß correspond to α-TCP and ß-TCP phases, respectively, while non-marked peaks correspond to hydroxyapatite phases. Vertical offset was adjusted for individual curve analysis.

Even though the previous analysis gave a strong interpretation of the chemical constitution of samples, hydroxyapatite is known for eventually presenting associated secondary phases. These complementary phases are not considered impurities since they usually derive from incomplete or less controlled reactions.

XRD is a technique that helps to evaluate the composition of crystalline materials, providing difractograms with intense peaks that correspond to the sample fingerprint. In the case of HAp and Fe-HAp samples, the non-sintered versions proved to be amorphous (see Appendix A.1), due to the broad bands obtained from XRD and associated with these, small secondary phases that may be present cannot be easily detected [66]. On the other hand, the sintered samples show a clealy crystalline structure, characterized by the high intensity and sharp peaks presented in the difractrogram.

With this analysis, it is possible to conclude that both doped and undoped samples are mainly composed by hydroxyapatite, with a hexagonal spatial conformation, and some secondary phases of α-TCP and ß-TCP, represented in figure 4.5 with α and ß, respectively. Such secondary phases were expected, since they are common when using the wet chemical precipitation method [66]. In this case, TCP probably derived from the incomplete reaction of the hydroxyl groups, since they are what distinguishes HAp from TCP. Nonetheless, on a biochemical point view, these calcium phosphates can have interesting applications since they are more easily degradable than hydroxyapatite, thus increasing the rate of calcium release [89]. Regarding the Fe-HAp samples, iron phases of magnetite and hematite were expected, however the difractogram did not show any evidence of such phases. This can be explained by the fact that, according to the literature, the main peak of magnetite appears at 2θ=36°, being

totally overlapped with the hydroxyapatite peak, and for this the RAMAN analysis proved to be more efficient [61].

In conclusion, all samples seemed to be mainly constituted by hydroxyapatite with small secondary phases of TCP. Regarding the Fe-HAp samples, iron presence cannot be discarded even though the XRD analysis was not conclusive. Some authors explain that iron is incorporated into the HAp lattice through calcium substitution. However, in order to confirm this hypothesis a more careful RAMAN analysis should be performed in order to understand the location of iron ions. Also, on XRD analysis, Ritvelt analysis could help to realize whether or not Fe^{3+} was partially substituting Ca^{2+} ions.

4.1.5 Electrical Properties

The electrical properties of HAp regarding its ferroelectric nature are still very little understood, with some authors referring to HAp as non-ferroelectric, while others report the contrary. Nonetheless, ferroelectric materials can have several applications in biomedicine, in cancer treatment, bone regeneration among others [90]. As already mentioned, ferroelectric materials can be employed to induce the formation of small pores on the cell membrane in order to de-stabilize cells and increase drug uptake.

In the study done at the macroscopic level with the conventional polarization vs. applied electric field measurements, all samples had a ferroelectric behaviour with the exception of the non-sintered Fe-HAp sample, represented in figure 4.6. It is important to notice that every hysteresis loop was different, leading to very distinct ferroelectric responses, shown by the coercive field and remanent polarization expressed in table 4.2. Regarding the HAp samples, the hysteresis loop opened up more with the sintering process, indicating a stronger ferroelectric response, however the non-symmetric loop indicated that there was a strong influence of current leakage that may happen with some types of capacitors [91]. Regarding the Fe-HAp samples the heat treatment seemed to have very significant effects in the ferroelectric behaviour. The non-sintered sample had the common response of a dielectric,

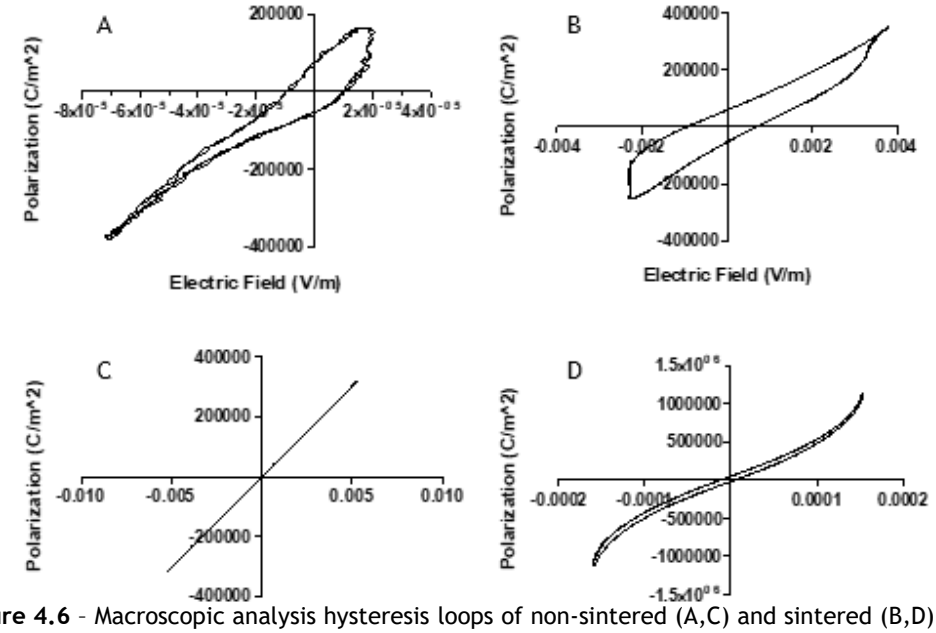

Figure 4.6 – Macroscopic analysis hysteresis loops of non-sintered (A,C) and sintered (B,D) HAp (A,B) and Fe-HAp (C,D) samples. One measurement was performed per sample.

observable by the lack of a loop formation, while its sintered counterpart had the common profile of a

Table 4.2 - Coercive field and remnant polarization of the samples.

Samples	**Coercive Field** (V/m)	**Remanent Polarization** (V/m)
HAp	7.50E+04	1.00E-05
HAp Sintered	6.00E+04	8.50E-04
Fe-HAp	0	0
Fe-HAp Sintered	4.00E+04	8.00E-06

hysteresis loop, clearly indicating a ferroelectric behaviour. It is also important to notice that the samples were in the hexagonal spatial group as suggested by the XRD analysis, but since piezoelectricity is not observable in centrosymmetric systems, it is possible to say that the samples have a non-centrosymmetric hexagonal conformation, and for this, better difractograms should be obtained [92].

On the other hand, PFM is a more grain specific technique that evaluates piezoelectricity, in a qualitative manner, grain by grain. From this analysis, represented in figure 4.7, it was possible to conclude that the sintered Fe-HAp sample had a clear ferroelectric nature, described by the hysteresis loop obtained from the amplitude and phase signals, corresponding to the results obtained with the macroscopic analysis. Regarding its non-sintered counterpart, it showed a faint ferroelectric response that was not detected at the macroscopic level. For the undoped samples, surprisingly the high ferroelectric behaviour of the sintered sample was not detected with PFM, showing a dielectric behaviour and therefor proving to be a good

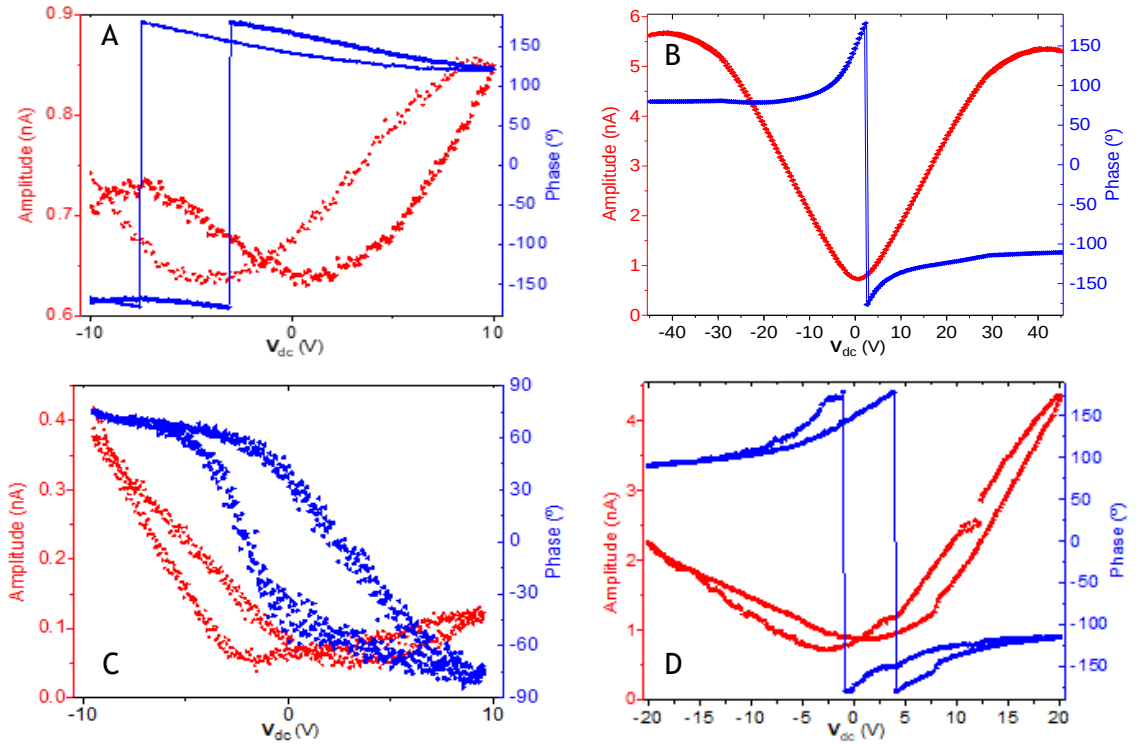

Figure 4.7 - Local piezoelectric hysteresis loops measured by PFM. Both phase (blue) and amplitude (red) signals are represented. A- HAp; B- Sintered HAp; C- Fe-HAp; D- Sintered Fe-HAp.

insulator. Such differences can be due to the region of the sample on which the electrical properties were measured. Thus, PFM analysis must be repeated to confirm the results. The non-sintered HAp sample showed a weak ferroelectric nature, also observable at the macroscopic level.

In general terms, the macroscopic tests should be the ones to take into account since they express the nature of the entire sample, however PFM should not be totally discarded (see Appendix A.2). This macroscopic results are very promising for the sintered Fe-HAp sample since it is a totally novel result that has never been described. Associated to this, iron incorporation can also lead to the creation of magnetic assets that alongside with the electric properties create a very powerful weapon in cancer detection and treatment, using techniques such as MRI, electroporation and magnetic hyperthermia.

4.1.6 Magnetic Properties

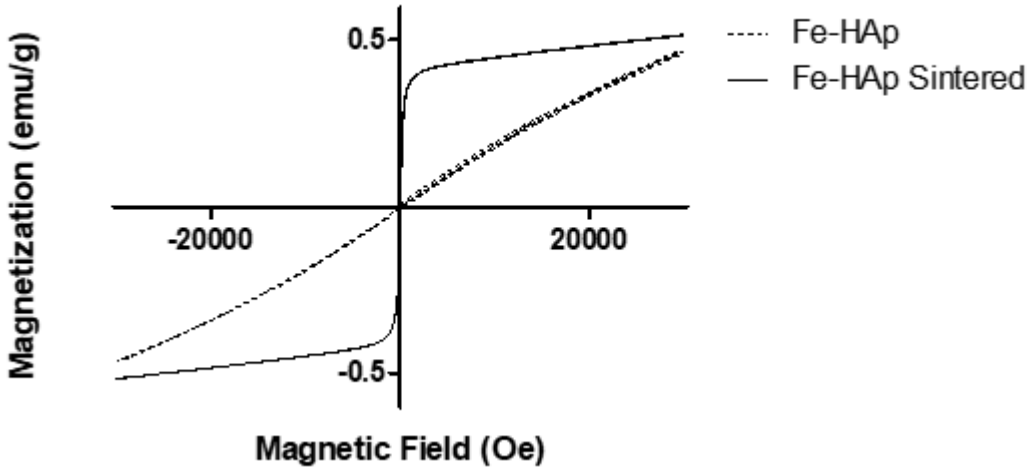

Figure 4.8 - SQUID characterization of sintered and non-sintered iron-doped hydroxyapatite nanoparticles. One measurement was made per sample.

Magnetic nanoparticles are being studied as contrast agents for MRI in order to avoid toxicity problems associated with current products. From RAMAN spectroscopy Fe-HAp samples indicated the presence of iron oxide phases and consequently, their magnetic properties were assessed, for both non-sintered and sintered samples.

Superparamagnetic iron oxide nanoparticles have high saturation magnetizations around 50-60emu/g, but since Fe-HAp samples have a low percentage of iron phases its magnetization was expected to be lower [34]. Some studies already described Fe-HAp nanoparticles as having saturation magnetization values between 0.5 and 1emu/g [66].

From the analysis of figure 4.8, sintered and non-sintered Fe-HAp nanoparticles showed completely different magnetic behaviours, with the first being superparamagnetic and the latter paramagnetic. Superparamagnetism is usually attributed to single magnetic domains of some iron oxides, however in these particles it can also be attributed to iron(III) domains incorporated into the HAp lattice [28]. Non-sintered nanoparticles, due to their low saturation magnetization, cannot be used as a contrast agents in MRI, while the superparamagnetic behaviour of the sintered nanoparticles reflects their potential to be used as T2-weighted MRI contrasting, despite their low saturation magnetization of 0.5emu/g.

In sum, this material seems to be a good alternative to current iron oxide nanoparticles that are used in clinics, in the sense that the superparamagnetic characteristics would be maintained while the complications associated with the toxicity of high concentrations of iron in the bloodstream would be reduced. However, Laranjeira et al. proved that this material is not perfectly blood compatible, for which these nanoparticles would need to be covered with some sort of blood compatible coating [66].

4.1.7 Contrast Agent Potential

Since the sintered Fe-HAp samples have the necessary magnetic requirements to be applied in T2-weighted MRI contrasting, several samples of Fe-HAp with increasing percentages of iron were produced and in order to assess such increment ICP was performed. From figure 4.9 it is possible to observe that there is in fact an increment in iron content, proving that hydroxyapatite can incorporate higher amounts of iron ions, while maintaining its characteristic chemical composition and structure (see Appendix A.3).

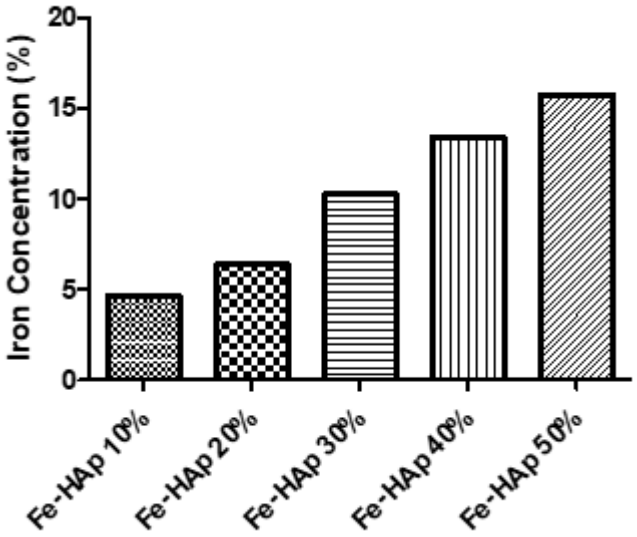

Figure 4.9 – ICP analysis of Fe-HAp doped with iron at 10, 20, 30, 40 and 50%.

In order to evaluate the potential of these particles for T2 contrast, the samples were exposed to a magnetic field using an actual MRI scanner that is already used in clinic. From the obtained images, represented in figure 4.10, it is possible to see that these particles have a slight contrast effect (red circles) however, due to particle deposition it was not possible to quantify which iron percentage gives the best results. For this reason, a better way of dispersing the particles in water should be explored in order to obtain a more homogeneous signal.

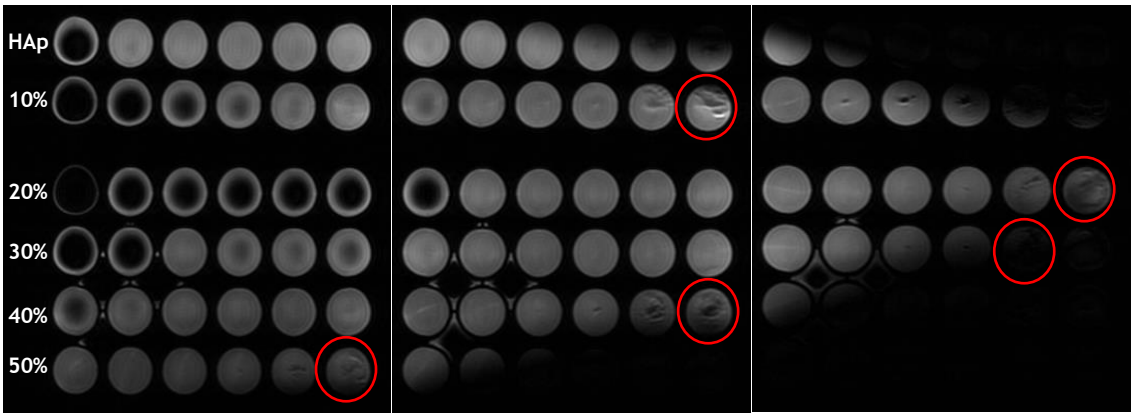

Figure 4.10 – Different Magnetic Resonance Imaging sections of HAp and Fe-HAp doped at different percentages. Particle concentration (100, 250, 500, 1000, 5000 and 10000μg/mL) increases from left to right in each image. Red circles indicate a contrast phenomenon.

However, it is possible to understand that 10% iron doping is already enough in order to obtain a T2-weighted contrast. This is a very important result since higher iron concentrations can lead to an intense cellular toxicity that is not ideal in intravenous administrated systems, presenting a good solution for the high iron concentration in common iron oxide particles used already in clinics [66]. Associated with this, a lower iron incorporation facilitates the production method, proposing a cheaper and also safer synthesis since the only side product from 10% Fe-HAp production is water and low quantities iron ions that do not react.

4.2 Cell Cultures

4.2.1 Toxicity of HAp and Fe-HAp Nanoparticles on Cancer Cells

The purpose for the development of these ceramic nanoparticles was to create an alternative treatment for triple negative breast cancer (TNBC). TNBC is the most aggressive subtype of breast cancer and associated with this, the only treatment option is chemotherapy, which unfortunately is linked to several negative side effects that also leads to low treatment success rates.

Hydroxyapatite, is mostly known for its biocompatibility and low toxicity, however nanosized hydroxyapatite particles seem to have higher toxicity when uptaken by cells [93]. Such toxicity is related to calcium release in the cytosol that creates an ion overload and therefore induce cell damage. Internally, mitochondria are the most susceptive organelles to calcium induced damage, where the membrane is destabilized, leading to the release of pro-apoptotic factors into the cytosol, activating an apoptotic response [94]. The cell membrane is also susceptive to damage, due to calcium interaction with the phospholipids that constitute the membrane [95].

Regarding Fe-HAp nanoparticles, studies were never performed in order to assess their toxicity on cancer cells. Nonetheless, it was expected for these particles to be more toxic due to iron ions. Iron plays a major role in several mechanisms of cell survival, however iron induced toxicity exists and is mostly observable at the mitochondria level [96].

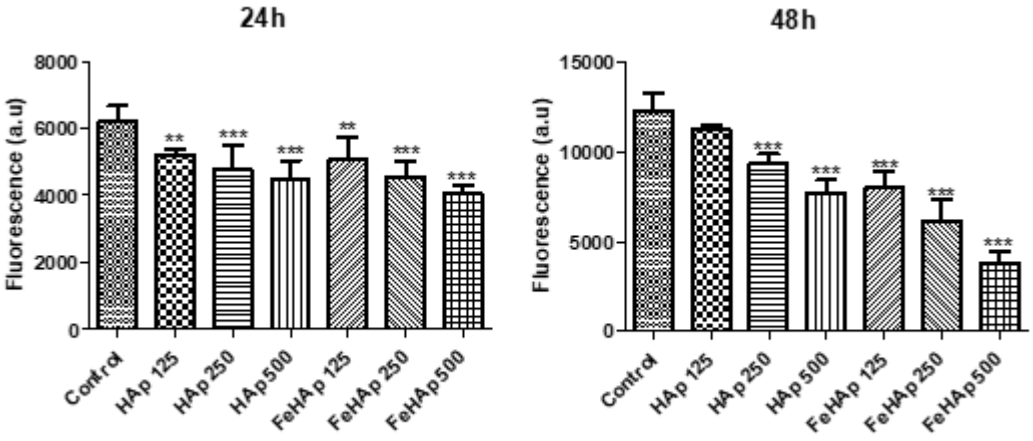

Figure 4.11 – Metabolic activity of MDA-MB-468 cell lines after 24h and 48h of incubation with HAp and Fe-HAp nanoparticles at densities of 125, 250 and 500mg/L. ** corresponds to $p<0.01$ and *** to $p<0.001$. All statistical differences were obtained in comparison with the control group.

In order to study the toxicity of the synthetized nanoparticles on cancer cells, TNBC cell lines were exposed to both sintered versions of HAp and Fe-HAp nanoparticles at different particle densities. The sintered versions of the nanoparticles where chosen due to their electric and magnetic properties, while particle densities where chosen based on the maximum concentration (500mg/L) of administrated contrast agents for MRI [97]. As a first test, a metabolic activity analysis was performed. From figure 4.11, it is possible to see that cells decreased their metabolic rates as particle density increased when compared to the control group at the 24h mark. Also, Fe-HAp nanoparticles induced a stronger effect than HAp nanoparticles. At the 48h mark the metabolic activity decreased even more, suggesting that cells were in stressful conditions.

To confirm these results a live/dead assay was carried out. This test consists in a fluorescence assay where viable cells give a green colour while non-viable cells show a red colour. Briefly, in live cells the nonfluorescent calcein AM is converted to green-fluorescent calcein, after acetoxymethyl ester hydrolysis by intracellular esterases, while propidium iodide easily enters damaged cells, marking them with a red colour. From figures 4.12 and 4.12, it is

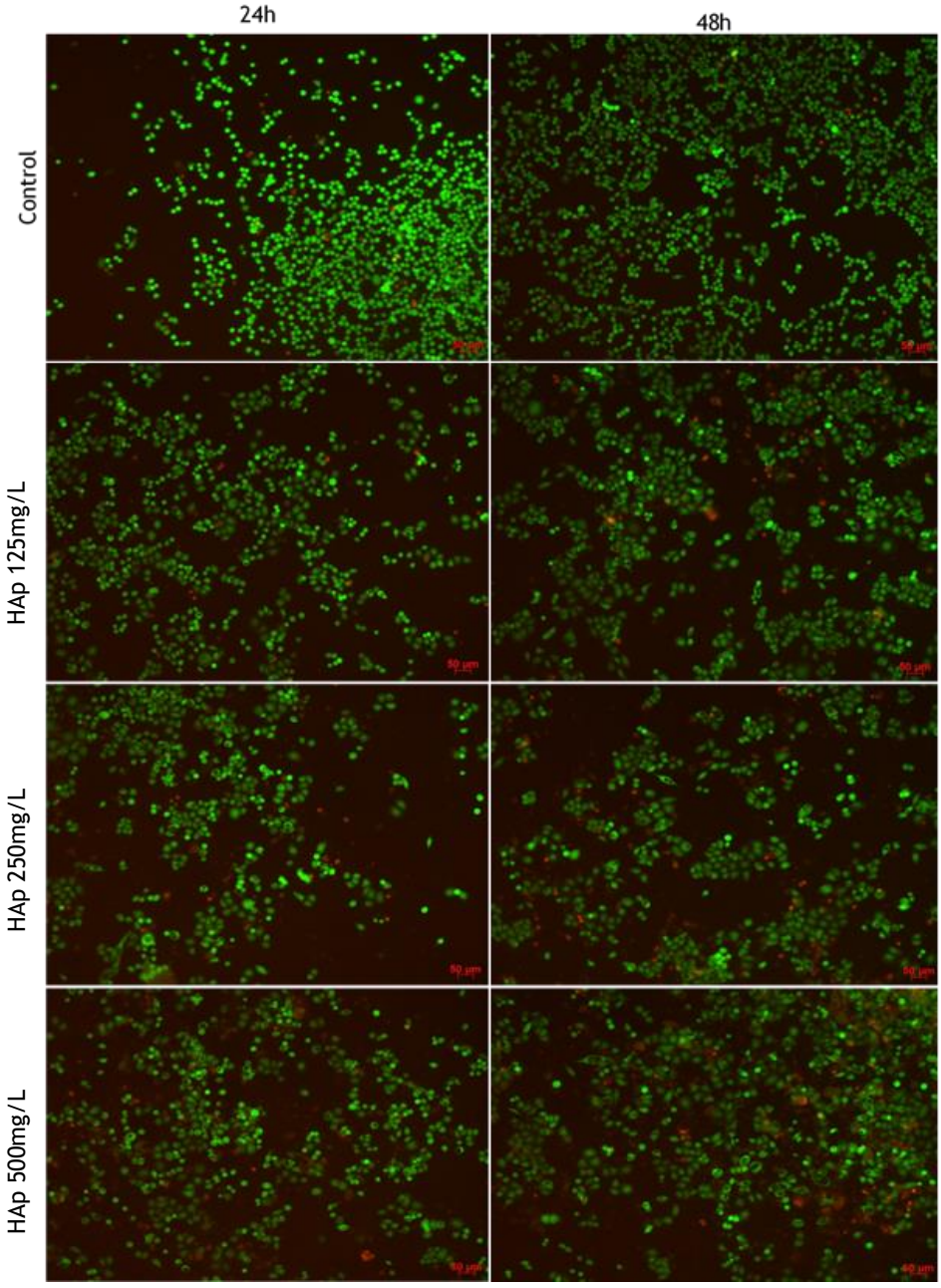

Figure 4.12 – Live/Dead assay on MDA-MB-469 cell lines after 24h and 48h of incubation with HAp nanoparticles at densities of 125, 250 and 500mg/L. Viable cells are marked with green while non-viable cells are marked with red. Scale bars: 50µm.

possible to observe an increase in red marked cells with particle density increase and such result was intensified for cells exposed to Fe-HAp nanoparticles. As expected at the 48h mark

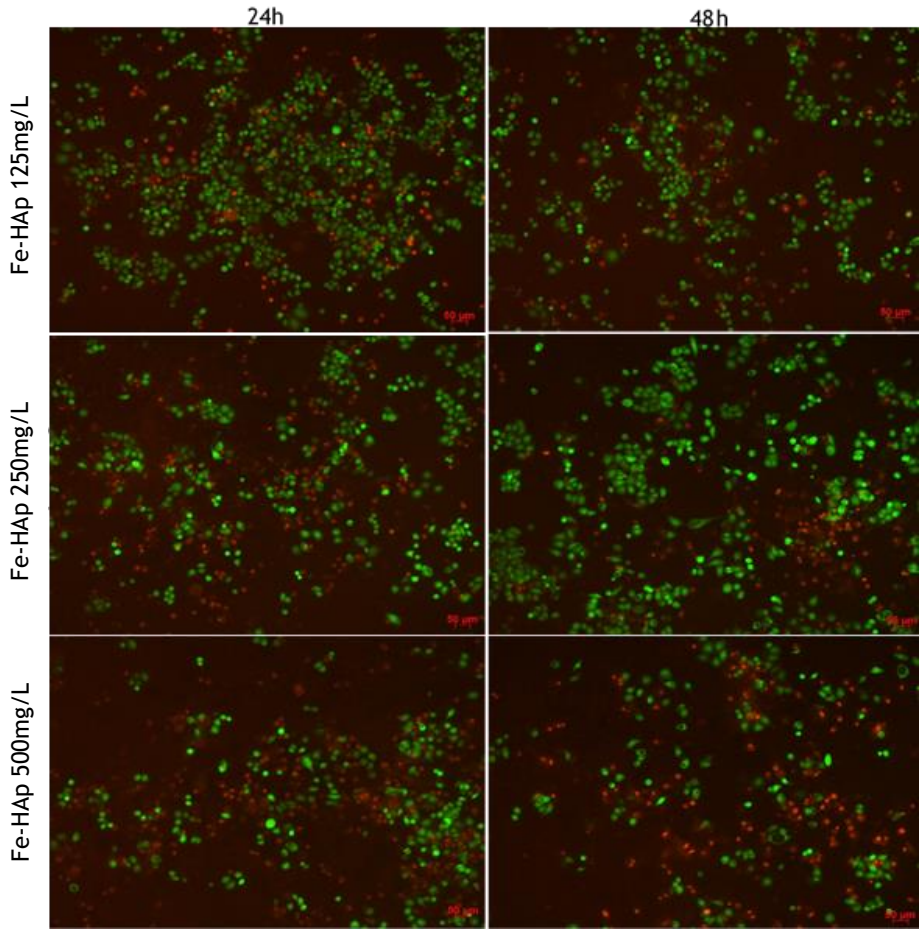

Figure 4.13 - Live/Dead assay on MDA-MB-469 cell lines after 24h and 48h of incubation with Fe-HAp nanoparticles at densities of 125, 250 and 500mg/L. Viable cells are marked with green while non-viable cells are marked with red. Scale bars: 50μm.

the non-viable population also increased. This qualitative analysis corroborates the results obtained with the metabolic activity assay, since non-viable cells have a lower metabolic activity.

From these two preliminary tests, very promising results were obtained, suggesting that some sort of damage/toxicity was being induced by the ceramic nanoparticles. Consequently, two more qualitative analysis were performed, evaluating morphology changes and also organelle dysfunction. MDA-MB-468 cells tend to arrange themselves in a cobblestone-like morphology when fully viable, from figures 4.14 and 4.15, it is possible to observe that several cells lose their shape, becoming rounder, and in some conditions it is possible to spot free nucleus (marked with a blue colour) without cytoplasm (marked with a green colour) which is a good indicator for cell death. Interestingly enough, non-viable cells tend to separate, indicating a loss in communication between cells, which is crucial for cell survival [98]. Additionally, when compared to the control group, less mitotic activity can be detected, with less dividing cells. All these phenomena tend to be more intense with particle density increase and more prevalent on cells exposed to Fe-HAp nanoparticles. Additionally, all these results were intensified at the 48h mark, being in agreement with the live/dead and metabolic activity assays.

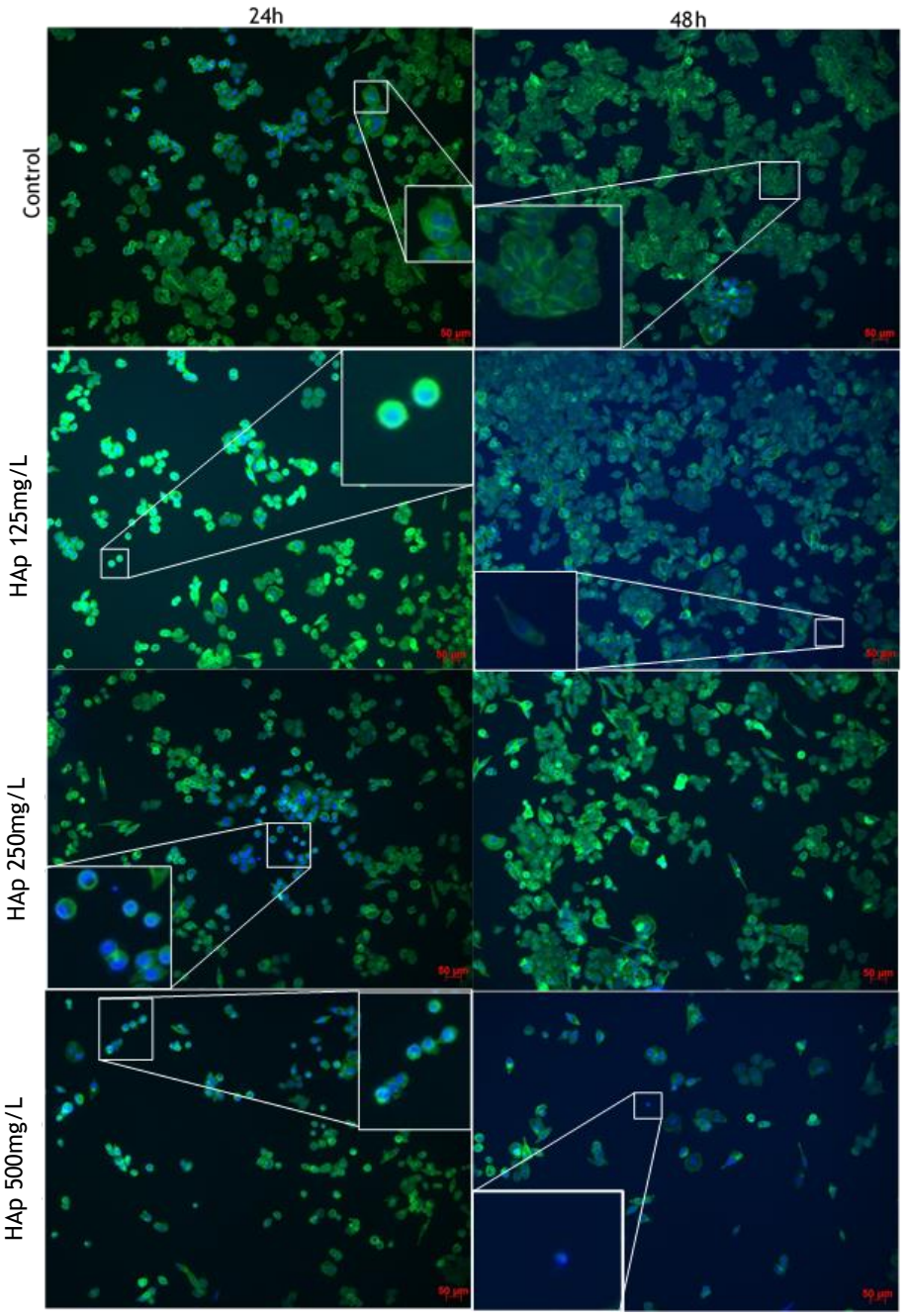

Figure 4.14 – Fluorescence images of MDA-MB-469 cell lines after 24h and 48h incubation with HAp nanoparticles at densities of 125, 250 and 500mg/L. Nuclei were stained with DAPI and F-actin with Alexa Fluor® 488. All images have been equally enhanced for contrast and brightness in agreement with the Journal of Cell Biology policies. Inset images represent magnifications of significant sections. Scale bars: 50µm.

For the second test, cells ultrastructure was evaluated by TEM at the 24h mark. Firstly, from the obtained images, shown in figures 4.16 and 4.17, it is possible to confirm nanoparticle internalization, where this is mainly mediated by an endocytosis process as explained by Meena et al. [99]. On cells exposed to HAp nanoparticles (figure 4.16) the first spotted difference is the loss of pseudopody, indicating a loss of cell membrane stability, and also explaining the round and isolated cells seen in the morphology evaluation test. Nonetheless, as expected, the most affected organelles where the mitochondria (green arrows), where it was visible that with particle density increase this organelles tend to swell, lose their external shape and also the cristae shape. This results show, beyond doubt, that released calcium ions interact directly

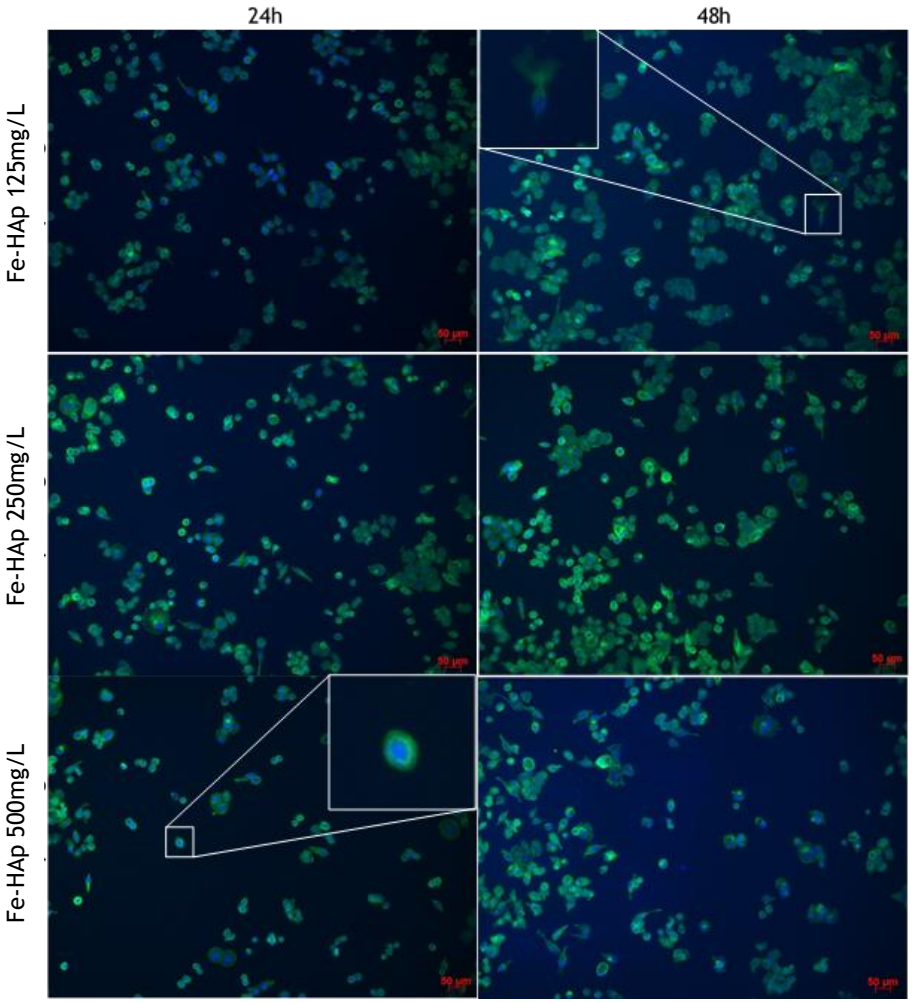

Figure 4.15 - Fluorescence images of MDA-MB-469 cell lines after 24h and 48h incubation with Fe-HAp nanoparticles at densities of 125, 250 and 500mg/L. Nuclei were stained with DAPI and F-actin with Alexa Fluor® 488. All images have been equally enhanced for contrast and brightness in agreement with the Journal of Cell Biology policies. Inset images represent magnifications of significant sections. Scale bars: 50µm.

with mitochondria and also with the cell membrane, making the toxicity levels higher. Additionally, a usually difficult organelle to spot is the Golgi apparatus (yellow arrow), was easily found and associated with it, several lysosomes where also spotted, indicating the efforts of the cell to digest and eliminate the excess ions [95].

Finally, on cells exposed to Fe-HAp nanoparticles (figure 4.17), all toxicity indicators found on cells exposed to HAp nanoparticle were also spotted, associated with higher mitochondria damage and also some mortal remains of totally disrupted cells (blue arrow). In fact, a phenomenon not found on HAp exposed cells was the formation of lipid droplets (red arrows). This structures are common in highly stressed cells and are usually associated with mitochondria damage [100]. Cells produce lipid droplets as a way to fight oxidative stress, very commonly induced by iron overload, by accumulating toxic mitochondria derived lipids. However, lipid droplet formation has also been associated with avoiding toxicity from misfolded proteins and as a method to maintain cell membrane stability [101].

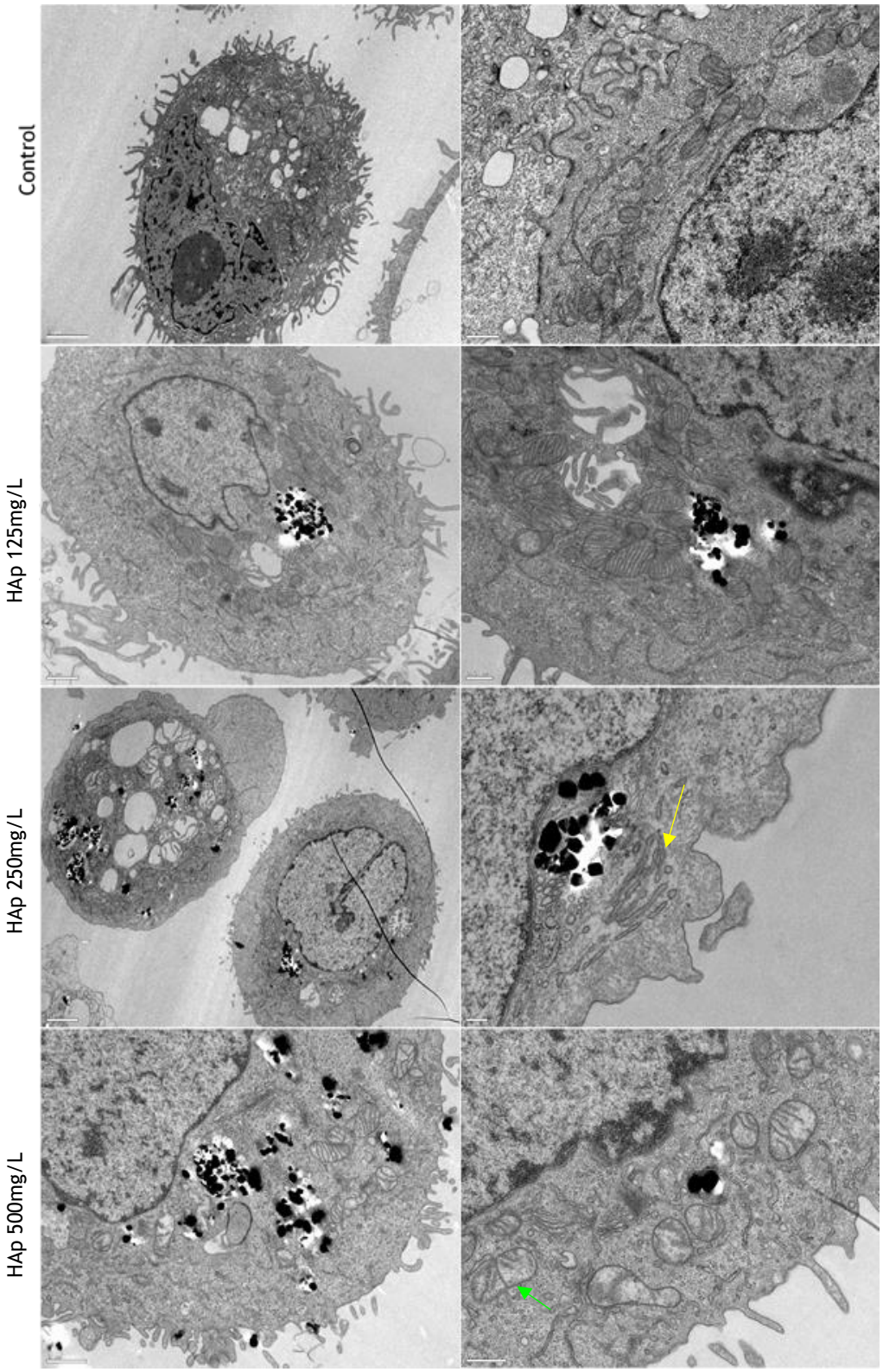

Figure 4.16 – TEM images of MDA-MB-468 cells incubated for 24h in the presence of HAp nanoparticles.

As a result, the synthetized nanoparticles proved to be very efficient on inducing cancer cell death only by themselves. Nonetheless, techniques such as electroporation and magnetic hyperthermia should intensify these results and therefore give rise to a more robust treatment.

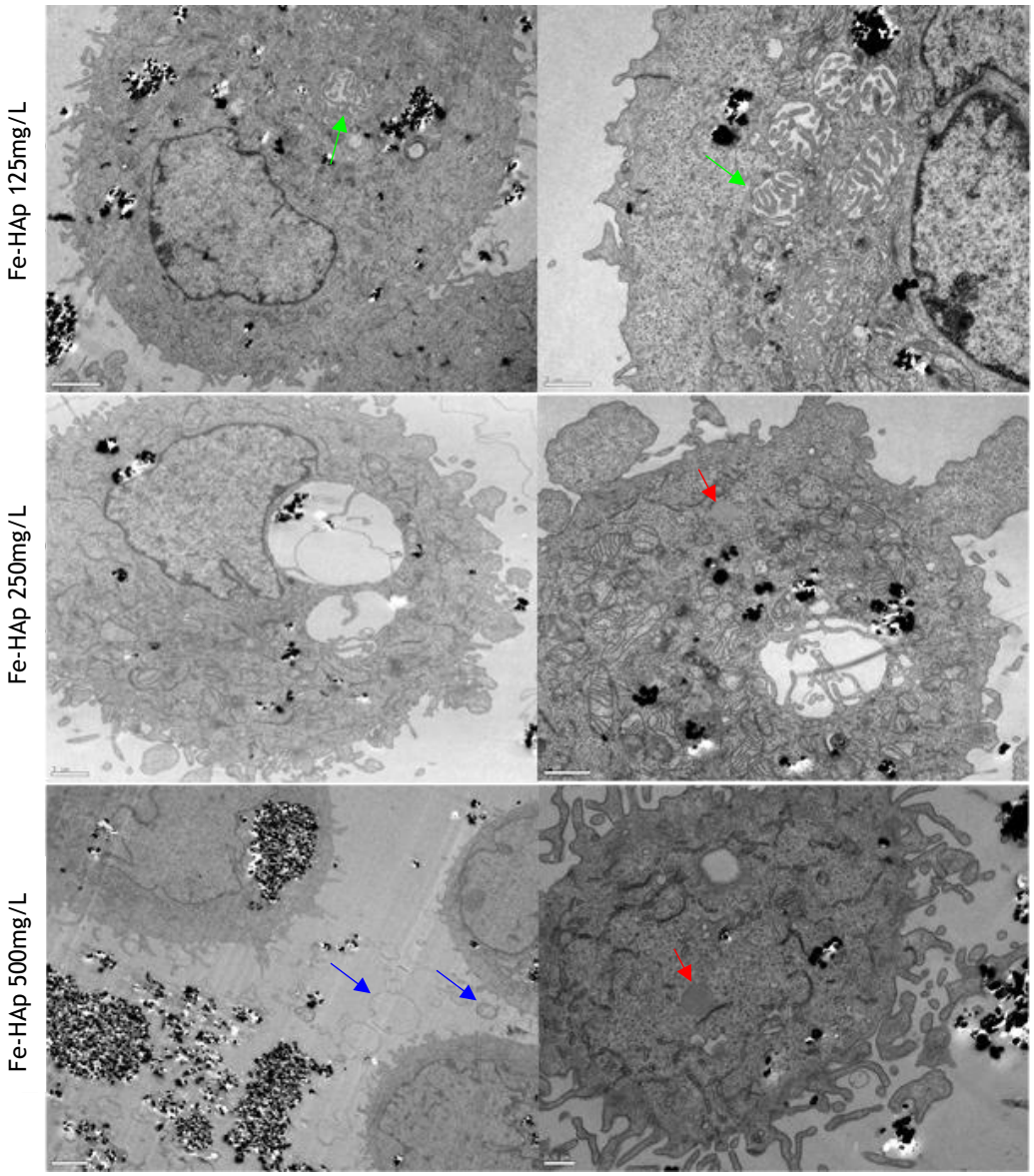

Figure 4.17 - TEM images of MDA-MB-468 cells incubated for 24h in the presence of Fe-HAp nanoparticles.

4.2.2 Toxicity of HAp and Fe-HAp Nanoparticles on Fibroblasts

Since the synthesized nanoparticles proved to be toxic to cancer cells, a test on healthy cells was performed in order to ensure a cancer specific targeting. Fibroblasts are highly predominant cells in breast cancer tumour microenvironments, and for this reason, primary cultures of HGF were exposed to the ceramic nanoparticles in the same conditions as the ones for cancer cells [102].

Surprisingly, as observable from figure 4.18, very different results were obtained at the 24 hour mark. Fibroblasts metabolic activity seemed not to be altered by the influence of the nanoparticles, and the live/dead confirmed such results, where the viable cell population did not decrease a lot in comparison with the control group. However, at the 48 hour mark toxicity started to induce effects on the cells. Firstly, the metabolic activity of fibroblasts exposed to Fe-HAp nanoparticles decreased significantly with increasing particle density, however no differences were obtained for cells exposed to HAp nanoparticles, showing that iron plays a

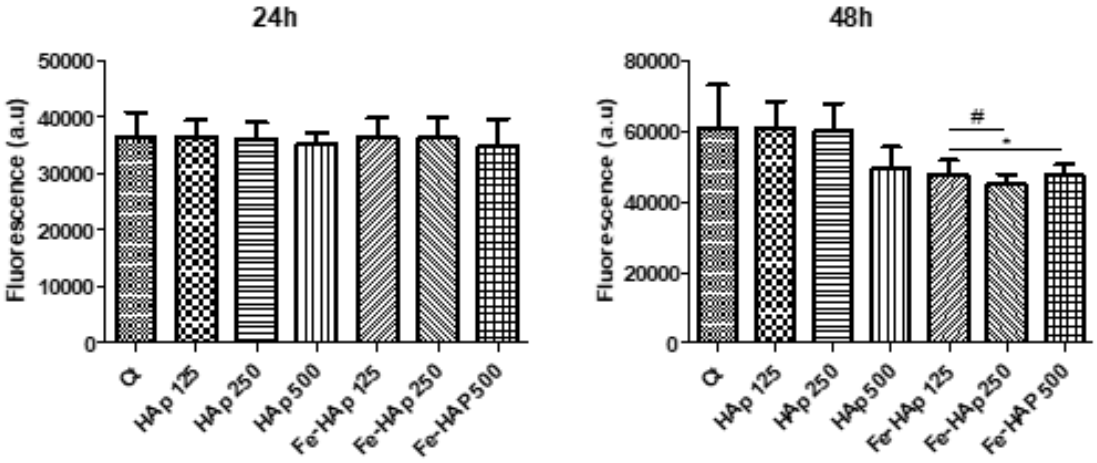

Figure 4.18 - Metabolic activity of HGF cells after 24h and 48h of incubation with HAp and Fe-HAp nanoparticles at densities of 125, 250 and 500mg/L. * corresponds to $p<0.05$ in comparison with the control and # to $p<0.01$ in comparison between types of nanoparticles.

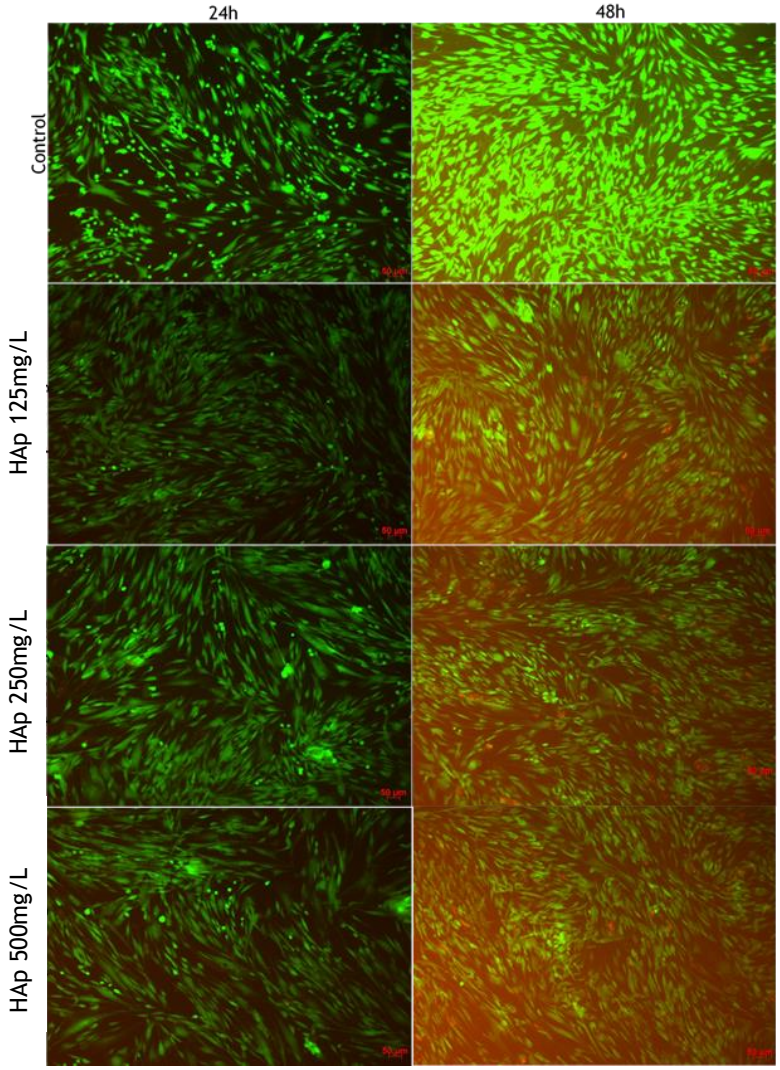

Figure 4.19 - Live/Dead assay on HGF cells after 24h and 48h of incubation with HAp nanoparticles at densities of 125, 250 and 500mg/L. Viable cells are marked with green while non-viable cells are marked with red. Scale bars: 50µm.

major role in cell toxicity. Such results were also confirmed by the live/dead assay, presented in figures 4.19 and 4.20, where the non-viable cells population increased for groups exposed to

the nanoparticles, in comparison with the control group.

When comparing the effects of the ceramic nanoparticles on cancer cells and fibroblasts, the differences are obvious, indicating that cancer cells are more susceptible to ion overload toxicity. This can be explained by the biochemical characteristics of cancer cells, where these ones do not possess well defined mechanisms for dealing with ion overload, while healthy cells can more easily counteract this overload through exocytosis [103]. However, at the 48h mark fibroblasts started to suffer from the influence of these nanoparticles, indicating that they should be modified to be internalized only by cancer cells. Such modification can be achieved through antibody functionalization of the particles and in the specific case of TNBC, studies show that VEGF and Pd-L1 are good targets [104].

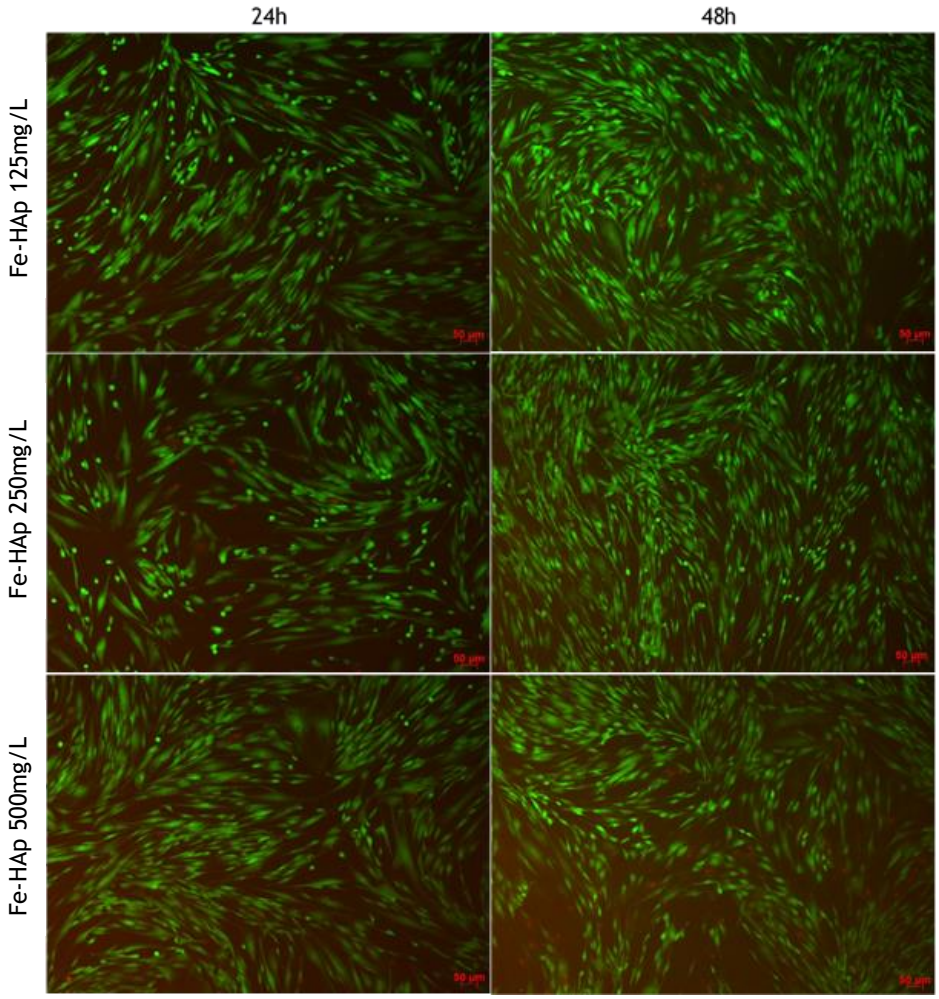

Figure 4.20 - Live/Dead assay on HGF cells after 24h and 48h of incubation with Fe-HAp nanoparticles at densities of 125, 250 and 500mg/L. Viable cells are marked with green while non-viable cells are marked with red. Scale bars: 50µm.

4.3 Polymeric Microgels Characterization

4.3.1 Size and Thermo-responsivity

The aim of this work regarding the production of polymeric microgels was to obtain thermo-responsive microparticles with sizes below 300nm at 25°C and a lower critical solution temperature (LCST) around 39°C. Throughout the synthesis of the final nanoparticles, intermediate syntheses were conducted to assess the properties of each individual portion. The intermediate steps include the production and characterization of core and shell particles.

Firstly, PNIPAM microgels were produced in order to understand their characteristics since NIPAM is the main constituent of the final microgels and the responsible monomer for temperature responsiveness. These microgels showed a LCST of 34.32°C (figure 4.21A) that is different from the 32°C found in the literature [49]. This phenomenon can be explained by the low degree of crosslinking derived from the low concentration of BIS used to produce the microgels. As explained in the literature, at lower crosslinking degrees, polymer chains are more loosely held together and consequently their repulsive forces are weaker, leading to an increase in the LCST. However, another factor to take into account is the effect of the surfactant. In fact, SDS is an anionic surfactant that, at temperatures below the LCST, can form micelles within the polymer matrix and further stretch it. Some studies reported that higher concentrations of SDS can lead to a LCST close to 37°C [105].

Since the PNIPAM microgels do not easily have a LCST of 39°C, the idea of a copolymer was explored using DMAEMA as a co-monomer in order to get the polymer closer to those temperatures. This copolymer was classified as the core of the final product. Despite all the efforts to optimize the synthesis protocol of the core microgels, where several monomer ratios, initiator and surfactant ratios and types were tested, from the analysis (figure 4.21B) it was clear that the protocol produced very different results between batches in terms of size. The core thermoresponsivity, however, did not vary much as the LCST kept at an average of 40.51°C. Also, despite these distinct cores, the final core-shell was not radically affected.

On the other hand, shell microgels showed very homogeneous results between batches, regarding both size and LCST values (figure 4.21C). The LCST mean value obtained from these microgels was 36.98°C, showing that the addition of PEGMA into the matrix increased the PNIPAM usual LCST. Such increase is mainly due to the size of the PEGMA chains and their interactions inside the polymer. Some authors explain that longer chains of PEGMA can further increase the LCST, but such phenomenon has never been fully described. Actually, the main purpose of the analysis of the shell particles was to observe LCST changes, as way to infer about the adequate shell formation around the core particles.

Finally, as a preliminary test core-shell microgels were produced. These polymeric particles showed excellent size homogeneity and LCST values of 39.04°C, located between the average values for core and shell microgels, showing the presence of the PNIPAM-co-DMAEMA nuclei. However, more core-shell replicas should be produced and analysed in order to perform a thorough study.

In sum, core-shell microgels were successfully produced with hydrodynamic sizes, slightly above 300nm at 25°C and a LCST of 39.04°C (figure 4.21D). The sizes at room temperature may be too high for intravenous administration, nonetheless at regular body temperature (~37°C)

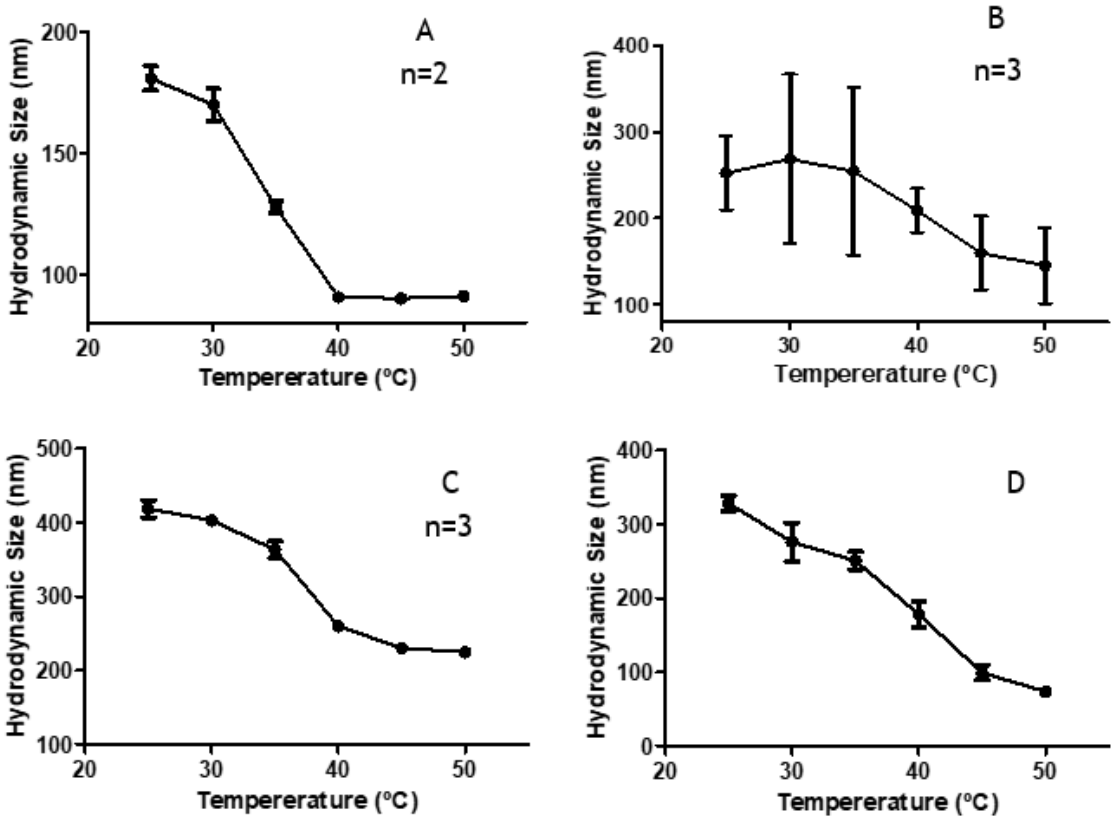

Figure 4.21 - Temperature trend curves for PNIPAM (**A**), core (**B**), shell (**C**), and core-shell (D) microgels. All are presented as the average temperature curve for n batches except for core-shell microgels. Data represented as mean ± SD (n= number of batches of each type of microgel). Boltzmann sigmoidal fit analysis were conducted for V50 (LCST) comparisons.

these nanocarriers would have diameters below 200nm, thus not imposing risk of emboli formations. Additionally, these sizes could facilitate cell uptake and due to the LCST the microgels contents should only be released in the tumour milieu where temperatures are higher.

4.3.2 Surface Charge

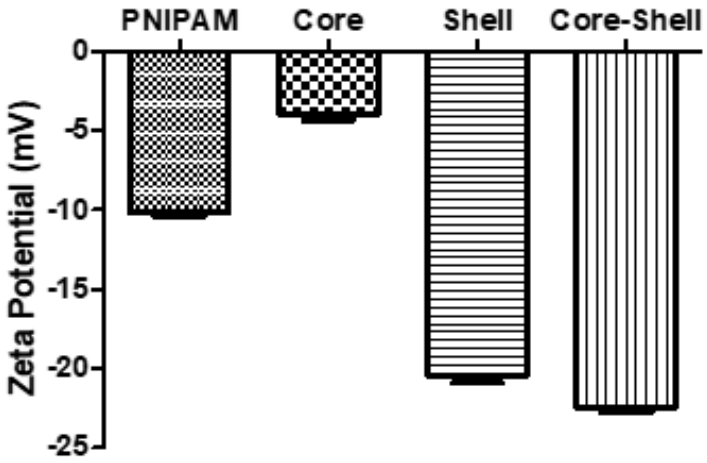

Figure 4.22 - Zeta potential of PNIPAM, core, shell and core-shell aqueous suspension at 25ºC. Data represented at mean ± SD (n= number of measurements presented in figure 26).

As already explained, surface charge plays a huge rule in the interaction between nanoparticles and cells. The zeta potential analysis performed on the microgels has two main objectives, the first to characterize the microgels in terms of surface charge to predict their behaviour in cell interaction, while the second was to confirm the synthesis of the co-polymers and finally the correct formation of the shell layer in the core-shell microgels.

From these analysis (figure 4.22), PNIPAM microgels showed a negative surface charge, ~-10mV, besides the neutral NIPAM monomer. The negative value can be derived from the negatively charged SDS and APS molecules used during synthesis. Not surprisingly, core microparticles showed values close to zero, due to the cationic nature of DMAEMA. Shell nanoparticles, on the other hand showed a very negative surface charge due to the presence of PEGMA that in aqueous solution exposes its OH^- terminations facing outwards. Interestingly, core-shell microgels also reported a highly negative surface charge, -22.4mV, due to the terminal groups of PEGMA in the outer shell of the polymer.

In short, every type of microgel had its own characteristic surface charge derived from its composition. The final core-shell microgels presented a negative surface charge, contributing to a good colloidal suspension, a characteristic that can be useful in order to diminish toxicity during intravenous administration.

4.3.3 Morphology

Morphology assessment was not very conclusive through TEM imaging (figure 4.23). Taking into account the low crosslinker percentage used to synthesize the microgels, it is possible to hypothesize that the vacuum to which the samples are submitted may disrupt the particle

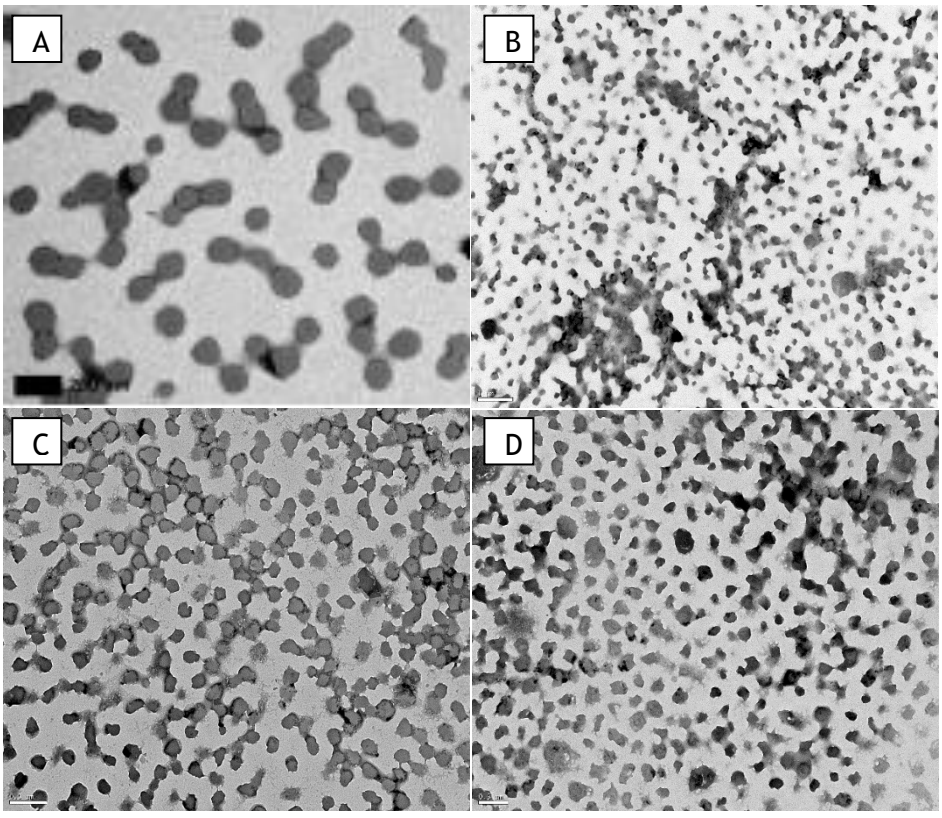

Figure 4.23 - TEM images for PNIPAM (**A**), core (**B**), shell (**C**) and core-shell (**D**) microgels. Scale bars: 200nm (A) and 500nm (B,C,D).

structure [106]. PNIPAM was used as a control during this analysis due to its more uniform and well-known synthesis. Naturally, the most damaged sample was the one corresponding to the core microgels, due to its very heterogeneous synthesis. Nonetheless, two interesting conclusions can be taken from this analysis, being the first one the spherical shape, that is characteristic of methacrylate based microgels synthesised through free radical polymerization. The second observable phenomenon is that most particle size did not correspond to the values obtained from DLS. This effect may be due to water removal during sample preparation and/or the interaction with the grid [79].

In short, TEM proved to be a weak technique to assess size of such weakly-crosslinked particles, nevertheless, the expected spherical shape was confirmed.

4.3.4 Chemical Profile

The chemical composition of polymeric microgels provides information about the success of the polymerization and the presence of contaminants.

According to figure 4.24, all spectra comprise peaks at ~3500cm^{-1} corresponding to N-H stretching, ~1640cm^{-1} corresponding to C=O stretching, and ~1548cm^{-1} corresponding to C-N stretching, all relative to the amide bonds of PNIPAM. The peak at ~3299cm^{-1} probably corresponds to the O-H stretching of water, and the =C-H stretch peak at ~3050cm^{-1} possibly corresponds to the unreacted methacrylate and acrylamide groups that were unsuccessfully removed. The -C-H stretching region is located between ~2975cm^{-1} and ~2875cm^{-1} and is represented by three peaks. Similarly, the C–H deformation region is also characterized by three peaks at approximately 1460cm^{-1}, 1387cm^{-1} and 1371cm^{-1}.

Since tertiary amines, present in DMAEMA, do not show any peaks in FTIR relative to N-H stretching, little to no difference was detected between the core microgels and the remaining samples. PEGMA on the other hand could be identified through its unique peaks at ~1106 and ~1250cm^{-1}, corresponding to C-O and C-O-C stretching, respectively. However, due to the low amounts of PEGMA introduced in these peaks are overrun by the NIPAM signal.

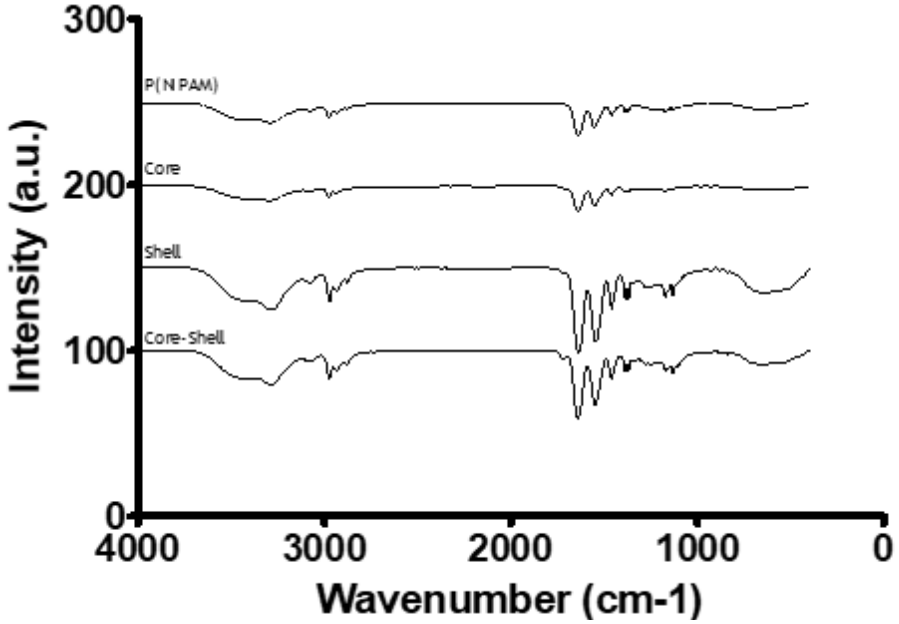

Figure 4.24 - Fourier transformed infrared spectrogram of PNIPAM, core, shell and core-shell microgels. Vertical offset was adjusted for individual curve analysis. One measurement per sample was performed.

In sum, for these low percentage co-polymers FTIR was not very conclusive, but it was still possible to see that NIPAM was in fact the major component of the particles. Regarding PEGMA inclusion, in order to confirm its presence, protein adsorption assays should be performed in the future.

4.4 Magnetic Ceramic Nanoparticles Encapsulation

The purpose of producing the microgels was to encapsulate the sintered Fe-HAp nanoparticles inside the core and with this, to produce a magnetic thermo-responsive composite. For this, two distinct protocols were tested, the first one was a simpler version were the nanoceramics were added to the polymerization reaction in their natural state and the second involved a pre-functionalization of the inorganic particles. Both were analysed by TEM to determine the success of the encapsulation.

For the first protocol the idea of encapsulation was based on the concept of seeded polymerization. In theory, microgels are developed through a series of steps that start with nucleation. Such phenomenon is based on the aggregation of the monomers followed by crosslinking and expansion, however this nucleation step tends to be facilitated if some solid seeds are presents. Based on this information, in the first encapsulation protocol, the Fe-HAp nanoparticles were used as seeds on which the polymer would form. After the polymer coating was formed, ceramic particle deposition was observed and because of this the final shell layer was immediately synthetized in order to imprison as many Fe-HAp nanoparticles as possible.

From the TEM analysis (figure 4.25), it was possible to see that some particles were indeed encapsulated, however empty microgels were obtained, as well as some polymer aggregates and non-encapsulated particles. Thus, this results showed a non-specific encapsulation with high variability between encapsulated and non-encapsulated particles and for this reason the second protocol was expected to perform better.

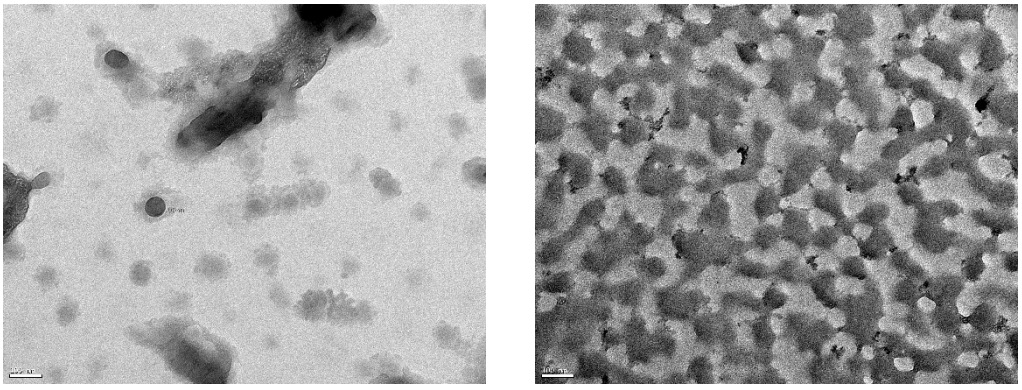

Figure 4.25 - Representative TEM images of the attempts of Fe-HAp encapsulation onto core microgels through the first protocol. Notice how ceramic clusters adopted a slightly rounder shape inside the microge. Scale bars: 100nm.

In the second protocol, Fe-HAp nanoparticles were functionalized with the objective to avoid the formation of empty microgels. Fe-HAp nanoparticles have at the surface OH^- groups at the surface to which a methacrylate ended coupling agent was covalently attached. Such linkage was mediated by the silanol groups of the coupling agent, through a series of hydroxylations and condensations, creating water as a side product. The now methacrylate functionalized nanoceramics would be able to covalently attach to the methacrylate groups of the core microgels, ensuring a complete encapsulation.

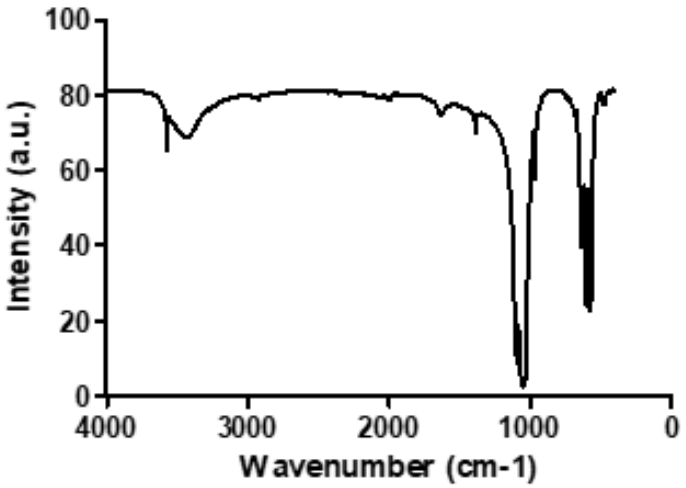

Figure 4.26 - FTIR analysis of the functionalized Fe-HAp nanoparticles. One analysis was performed.

Firstly, a FTIR analysis was performed to confirm the correct functionalization. From figure 4.26 it is possible to observe the methacrylate characteristic groups at 1400cm^{-1} corresponding to C-H deformation and the C=O stretching at ~1640cm^{-1}, not found on the bare Fe-HAp nanoparticles, indicating an adequate functionalization. Finally, from TEM analysis it is possible to observe a better encapsulation, when compared to the first method, shown in figure 4.27. Still, a heterogeneous sample was obtained, with regions presenting a correct encapsulation (figure 4.27A) of small nanoparticles embedded in the core matrix and with regions where polymer fusion was observable (figure 4.27B). Nonetheless, in these agglomerated areas (figure 4.27B), the formation of somewhat organized groups of ceramic nanoparticles could be seen, which may indicate encapsulation at the nucleus of the core microgels.

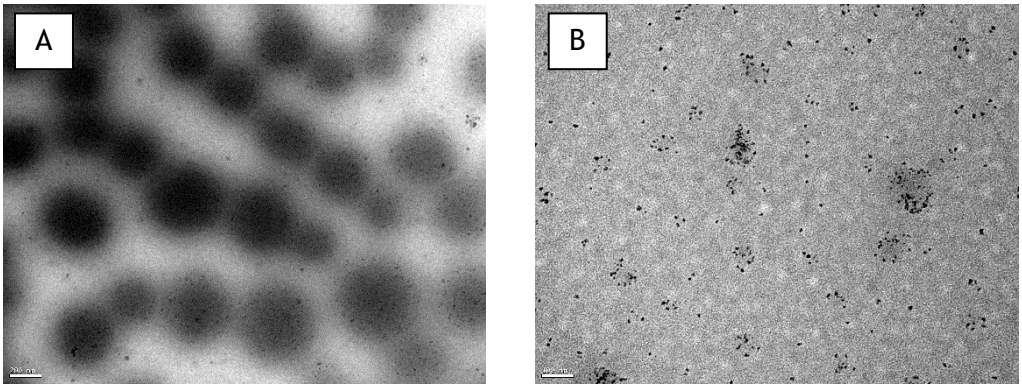

Figure 4.27 - Representative TEM images of the attempts of functionalized Fe-HAP encapsulation onto core microgels through the second protocol. Scale bars: 200nm.

In the future, a better dispersion of these microgels could be mediated by synthetizing the final shell layer, due to the stabilizing effects of the highly negative charged PEGMA terminal ends.

4.5 Drug Loading on Polymeric Core-Shell Microgels

The synthesized microgels, besides their capability for nanoparticle encapsulation, can also be used to encapsulate chemotherapeutical drugs such as doxorubicin. To assess encapsulation

efficiency (EE) and drug loading capacity (LC), a preliminary test was performed using a gel filtration column with Sephadex® G-25.

Given that the molecular weight of DOX is approximately 500Da, it was expected that the free drug eluted rapidly. Core-shell microgels were not expected to pass the 25kDa filter, since this MWCO corresponds to a hydrodynamic pore size of ~2nm [107]. The eluted free drug was collected and analysed, and yielded a final EE of 77.7% and a LC of 9.32% (figure 4.28).

With this, the final EE% and LC% showed an excellent loading of the hydrophobic drug. The next step would involve the release of DOX from the microgels in a biologically relevant buffer, such as PBS, at different temperature and pH conditions, in order to recreate the environments of the bloodstream, tumour milieu or inside the endosomes, and evaluate release rates accordingly.

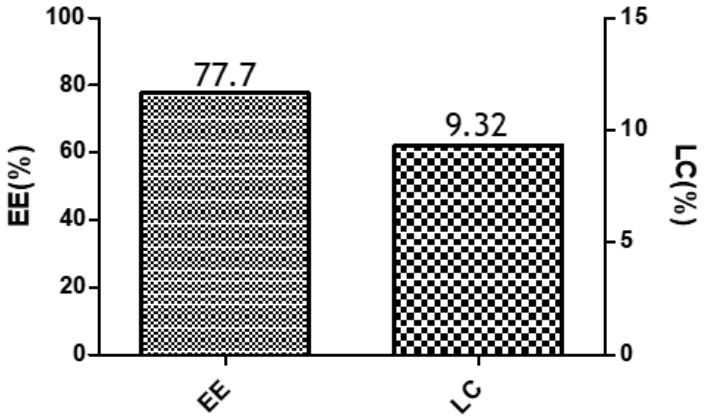

Figure 4.28 - Encapsulation efficiency (EE%) and drug loading capacity (LC%) of DOX loading into core-shell microgels.

(page intentionally left blank)

Chapter 5

Conclusion

This work presents the design of a magnetic thermo-responsive composite, comprising iron doped hydroxyapatite nanoparticles entrapped in the core of a core-shell microgel of P(NIPAM-co-DMAEMA)-co-P(NIPAM-co-PEGMA). This small scaled device is proposed as a solution for the problems associated with chemotherapy and MRI contrast agents toxicity in oncological diseases such as triple negative breast cancer.

Sintered HAp and Fe-HAp nanoparticles with a spherical shape and sizes below 100nm show very small amounts of secondary phases, consisting of TCP. Specifically, iron doped samples also show iron oxide phases and are also thought to have iron substitutions in the crystal lattice. Besides constitution, both HAp and Fe-HAp samples show electric properties, such as ferroelectricity, derived from the non-centrosymmetric hexagonal structure. This characteristic indicates that the materials are piezoelectric and therefor they can be used in cancer treatment, serving as substrates to induce electroporation, which can de-stabilize cells and increase drug uptake. Additionally, Fe-HAp samples presented superparamagnetic domains, showing good potential as contrast agents in MRI and for magnetic hyperthermia therapies. Moreover, both types of nanoparticles seem to have high toxic effects in cancer cells, due to intracellular calcium and iron release. Meanwhile, these nanoparticles present lower toxic effects on healthy cells, such as fibroblasts, due to well established mechanisms of healthy cells to avoid ion overload.

Tumours usually have temperatures above normal tissues due to an uncontrolled cell division and blood affluence. Taking this into consideration, when properly tuned, thermo-responsive microcarriers can release drugs and other contents, specifically into the tumour site without the need of external stimuli. Thereby, the transition temperature of the produced core-shell microgels was fixed at 39.04°C, which normal tissues cannot usually reach. Sizes below 200nm at body temperature and the covalently attached PEG chains also contribute for the safe profile of these carriers to be administrated through the intravenous route, since there is a reduced probability of thrombus formations and since the hydrophilic chains increase the circulation half-life of the system, contributing to a large accumulation at the tumour site. Still, for a better targeting model, antibodies such as VEGF and Pd-L1 could be covalently attached to the microgel, resulting in a more precise delivery.

In conclusion, the emerging field of theranostics has aimed to conjugate both therapeutic and diagnosis functionalities in one single system, with less toxicity to healthy tissues, high simplicity and best cost-effectiveness. This field promises to be a significant contribution to cancer treatment, proposing new solutions to counteract problems associated with current methods. Furthermore, due to the growing interest of the scientific community in this subject, it will not be long until these smart devices enter clinical trials and possibly be marketed.

(page intentionally left blank)

Chapter 6

Future Perspectives

Even though this project is still in an initial phase, the work presented very promising results, for which some further work still needs to be done.

In the short-term, cancer cells should be cultured in the presence of ultrasounds, in order to stimulate the electroporation effects by the piezoelectric nanoparticles. In terms of magnetism, sintered iron doped nanoparticles should be tested in terms of hyperthermia in order to evaluate the temperature that they are able to reach and how long it takes to reach it. Also, better MRI contrast images should be obtained by dispersing the particles in a high surfactant concentration in order to obtain a more uniform signal.

Regarding the microgels, more optimization steps should be performed in order to have a more controlled synthesis and therefore a more uniform and reliable outcome. Additionally, the encapsulation step should be concluded by synthetizing the shell layer on the already encapsulated ceramics. To conclude the drug profile, release tests at different temperatures, should be performed.

In a long-term point of view, cell co-cultures should be performed in spheroids in order to simulate the tumour microenvironment. Also, the final magnetic composite should be tested in cell cultures in order to evaluate magnetic hyperthermia induced cell death, and also electroporation stimulation should be tested under applied magnetic fields. Additionally, particle functionalization with antibodies could be a solution for a better targeting model.

(page intentionally left blank)

References

[1] R. Siegel, "Cáncer Statistics," *Ca Cáncer J.*, vol. 67, no. 1, pp. 7–30, 2017.

[2] W. H. Clark, "Tumour progression and the nature of cancer," *Br. J. Cancer*, vol. 64, no. 4, pp. 631–644, 1991.

[3] J. Skog *et al.*, "Glioblastoma microvesicles transport RNA and proteins that promote tumour growth and provide diagnostic biomarkers," *Nat. Cell Biol.*, vol. 10, no. 12, pp. 1470–1476, 2008.

[4] N. E. Sounni and A. Noel, "Targeting the Tumor Microenvironment for Cancer Therapy," *Clin. Chem.*, vol. 59, no. 1, pp. 85–93, 2013.

[5] R. M. Bremnes *et al.*, "The role of tumor stroma in cancer progression and prognosis: Emphasis on carcinoma-associated fibroblasts and non-small cell lung cancer," *J. Thorac. Oncol.*, vol. 6, no. 1, pp. 209–217, 2011.

[6] D. Ribatti, E. Crivellato, A. M. Roccaro, R. Ria, and A. Vacca, "Mast cell contribution to angiogenesis related to tumour progression," *Clin. Exp. Allergy*, vol. 34, no. 11, pp. 1660–1664, 2004.

[7] M. Villiers, P. Aramwit, and G. S. Kwon, *Nanotechnology in Drug Delivery*. New York, NY: Springer New York, 2009.

[8] T. R. Daniels *et al.*, "The transferrin receptor and the targeted delivery of therapeutic agents against cancer," *Biochim. Biophys. Acta - Gen. Subj.*, vol. 1820, no. 3, pp. 291–317, Mar. 2012.

[9] M. Bittremieux and G. Bultynck, "p53 and Ca^{2+} signaling from the endoplasmic reticulum: partners in anti-cancer therapies," *Oncoscience*, vol. 2, no. 3, pp. 233–238, 2015.

[10] W. D. Foulkes, I. E. Smith, and J. S. Reis-Filho, "Triple-Negative Breast Cancer," *N. Engl. J. Med.*, vol. 363, no. 20, pp. 1938–1948, 2010.

[11] R. Dent *et al.*, "Triple-negative breast cancer: Clinical features and patterns of recurrence," *Clin. Cancer Res.*, vol. 13, no. 15, pp. 4429–4434, 2007.

[12] C. Liedtke *et al.*, "Response to neoadjuvant therapy and long-term survival in patients with triple-negative breast cancer," *J. Clin. Oncol.*, vol. 26, no. 8, pp. 1275–1281, 2008.

[13] R. Vadivambal and D. S. Jayas, *Bio-imaging: Principles, techniques, and applications*. 2015.

[14] V. Keereman, Y. Fierens, T. Broux, Y. De Deene, M. Lonneux, and S. Vandenberghe, "MRI-Based Attenuation Correction for PET/MRI Using Ultrashort Echo Time Sequences," *J. Nucl. Med.*, vol. 51, no. 5, pp. 812–818, 2010.

[15] G. B. Chavhan MD DND, P. S. Babyn MD, B. Thomas MD, M. M. Shroff MD, and E. M. Haacke PhD, "Principles , Techniques , and Applications of T2* - based MR Imaging and Its Special Applications," *RadioGraphics*, vol. 29, no. 62983, pp.

1433–1449, 2009.

[16] A. Urruticoechea, R. Alemany, J. Balart, A. Villanueva, F. Vinals, and G. Capella, “Recent Advances in Cancer Therapy: An Overview,” *Curr. Pharm. Des.*, vol. 16, no. 1, pp. 3–10, 2010.

[17] B. A. Chabner and T. G. Roberts, “Chemotherapy and the war on cancer,” *Nat. Rev. Cancer*, vol. 5, no. 1, pp. 65–72, 2005.

[18] E. Pérez-Herrero and A. Fernández-Medarde, “Advanced targeted therapies in cancer: Drug nanocarriers, the future of chemotherapy,” *Eur. J. Pharm. Biopharm.*, vol. 93, pp. 52–79, 2015.

[19] C. F. Thorn *et al.*, “Doxorubicin pathways,” *Pharmacogenet. Genomics*, vol. 21, no. 7, pp. 440–446, Jul. 2011.

[20] O. Tacar, P. Sriamornsak, and C. R. Dass, “Doxorubicin: An update on anticancer molecular action, toxicity and novel drug delivery systems,” *J. Pharm. Pharmacol.*, vol. 65, no. 2, pp. 157–170, 2013.

[21] B. J. Baselga *et al.*, “Phase II Study of Weekly Intravenous Recombinant Metastatic Breast Cancer,” *J Clin Oncol*, vol. 14, no. 3, pp. 737–744, 1996.

[22] E. Fröhlich, “The role of surface charge in cellular uptake and cytotoxicity of medical nanoparticles,” *Int. J. Nanomedicine*, vol. 7, pp. 5577–5591, 2012.

[23] S. N. S. Alconcel, A. S. Baas, and H. D. Maynard, “FDA-approved poly(ethylene glycol)-protein conjugate drugs,” *Polym. Chem.*, vol. 2, no. 7, pp. 1442–1448, 2011.

[24] V. Roy, B. R. Laplant, G. G. Gross, C. L. Bane, and F. M. Palmieri, “Phase II trial of weekly nab (nanoparticle albumin-bound)-paclitaxel (nab-paclitaxel) (Abraxane®) in combination with gemcitabine in patients with metastatic breast cancer (N0531),” *Ann. Oncol.*, vol. 20, no. 3, pp. 449–453, 2009.

[25] T. A. ElBayoumi and V. P. Torchilin, “Current Trends in Liposome Research,” in *Fundamentals of Pharmaceutical Nanoscience*, no. November 2015, 2010, pp. 1–27.

[26] X. Huang and M. A. El-Sayed, “Gold nanoparticles: Optical properties and implementations in cancer diagnosis and photothermal therapy,” *J. Adv. Res.*, vol. 1, no. 1, pp. 13–28, 2010.

[27] J. Carrey, B. Mehdaoui, and M. Respaud, “Simple models for dynamic hysteresis loop calculations: Application to hyperthermia optimization,” *J. Appl. Phys.*, vol. 109, p. 083921, 2011.

[28] M. Bañobre-López, A. Teijeiro, and J. Rivas, “Magnetic nanoparticle-based hyperthermia for cancer treatment,” *Reports Pract. Oncol. Radiother.*, vol. 18, no. 6, pp. 397–400, 2013.

[29] EC, “Scientific Basis for the Definition of the Term ‘ Nanomaterial ,’” *Sci. Comm. Emerg. New. Identified Heal. Risks*, no. July, pp. 1–43, 2010.

[30] T. Arantes, L. Coimbra, F. Cristovan, T. Arantes, G. Rosa, and L. Lião, “Synthesis and Optimization of Colloidal Hydroxyapatite Nanoparticles by Hydrothermal Processes,” *J. Braz. Chem. Soc.*, vol. 29, no. 9, pp. 1894–1903, 2018.

[31] T. Sun, Y. S. Zhang, B. Pang, D. C. Hyun, M. Yang, and Y. Xia, “Engineered nanoparticles for drug delivery in cancer therapy,” *Angew. Chemie - Int. Ed.*,

vol. 53, no. 46, pp. 12320–12364, 2014.

[32] S. Jafari, “Application of Hydroxyapatite Nanoparticle in the Drug Delivery Systems,” *J. Mol. Pharm. Org. Process Res.*, vol. 03, no. 01, pp. 1–2, 2015.

[33] B. Blasiak, F. C. J. M. Van Veggel, and B. Tomanek, “Applications of nanoparticles for MRI cancer diagnosis and therapy,” *J. Nanomater.*, vol. 2013, 2013.

[34] Y.-X. Wang, “Superparamagnetic iron oxide based MRI contrast agents: Current status of clinical application.,” *Quant. Imaging Med. Surg.*, vol. 1, no. 1, pp. 35–40, 2011.

[35] R. Chen *et al.*, “Parallel Comparative Studies on Mouse Toxicity of Oxide Nanoparticle- and Gadolinium-Based T1 MRI Contrast Agents,” *ACS Nano*, vol. 9, no. 12, pp. 12425–12435, 2015.

[36] S. Naqvi *et al.*, “Concentration-dependent toxicity of iron oxide nanoparticles mediated by increased oxidative stress,” *Int. J. Nanomedicine*, vol. 5, no. 1, pp. 983–989, 2010.

[37] R. Dey, S. Mazumder, M. K. Mitra, S. Mukherjee, and G. C. Das, “Review: Biofunctionalized quantum dots in biology and medicine,” *J. Nanomater.*, vol. 2009, 2009.

[38] Kim and Zheng, “Numerical characterization and optimization of the microfluidics for nanowire biosensors,” *Nano Lett.*, vol. 8, no. 10, pp. 3233–3237, 2008.

[39] K. Kerman, M. Saito, E. Tamiya, S. Yamamura, and Y. Takamura, “Nanomaterial-based electrochemical biosensors for medical applications,” *TrAC - Trends Anal. Chem.*, vol. 27, no. 7, pp. 585–592, 2008.

[40] E. G. R. Fernandes and A. A. A. De Queiroz, “A bioconjugated polyglycerol dendrimer with glucose sensing properties,” *J. Mater. Sci. Mater. Med.*, vol. 20, no. 2, pp. 473–479, 2009.

[41] R. Singh and J. W. Lillard, “Nanoparticle-based targeted drug delivery,” *Exp. Mol. Pathol.*, vol. 86, no. 3, pp. 215–223, Jun. 2009.

[42] Y. Shu, R. Song, A. Zheng, J. Huang, M. Chen, and J. Wang, “Thermo/pH dual-stimuli-responsive drug delivery for chemo-/photothermal therapy monitored by cell imaging,” *Talanta*, vol. 181, no. December 2017, pp. 278–285, 2018.

[43] M. Babincová, P. Čičmanec, V. Altanerová, Č. Altaner, and P. Babinec, “AC-magnetic field controlled drug release from magnetoliposomes: Design of a method for site-specific chemotherapy,” *Bioelectrochemistry*, vol. 55, no. 1–2, pp. 17–19, 2002.

[44] S. H. Hu, C. H. Tsai, C. F. Liao, D. M. Liu, and S. Y. Chen, “Controlled rupture of magnetic polyelectrolyte microcapsules for drug delivery,” *Langmuir*, vol. 24, no. 20, pp. 11811–11818, 2008.

[45] S. Rana, A. Gallo, R. S. Srivastava, and R. D. K. Misra, “On the suitability of nanocrystalline ferrites as a magnetic carrier for drug delivery: Functionalization, conjugation and drug release kinetics,” *Acta Biomater.*, vol. 3, no. 2, pp. 233–242, 2007.

[46] M. Chen-Glasser, P. Li, J. Ryu, and S. Hong, “Piezoelectric Materials for Medical Applications,” in *Piezoelectricity - Organic and Inorganic Materials and*

Applications, vol. 2, InTech, 2018, p. 64.

[47] J. Mérian, J. Gravier, F. Navarro, and I. Texier, “Fluorescent nanoprobes dedicated to in vivo imaging: From preclinical validations to clinical translation,” *Molecules*, vol. 17, no. 5, pp. 5564–5591, 2012.

[48] U. Prabhakar *et al.*, “Challenges and Key Considerations of the Enhanced Permeability and Retention Effect for Nanomedicine Drug Delivery in Oncology,” *Cancer Res.*, vol. 73, no. 8, pp. 2412–2417, Apr. 2013.

[49] S. Wilhelm *et al.*, “Supplementary Information Analysis of nanoparticle delivery to tumours,” *Nat. Rev. Mater.*, vol. 1, no. 5, p. 16014, 2016.

[50] G. D. Lewis Phillips *et al.*, “Targeting HER2-positive breast cancer with trastuzumab-DM1, an antibody-cytotoxic drug conjugate,” *Cancer Res.*, vol. 68, no. 22, pp. 9280–9290, 2008.

[51] A. Szcześ, L. Hołysz, and E. Chibowski, “Synthesis of hydroxyapatite for biomedical applications,” *Adv. Colloid Interface Sci.*, vol. 249, no. April, pp. 321–330, 2017.

[52] W. Habraken, P. Habibovic, M. Epple, and M. Bohner, “Calcium phosphates in biomedical applications: Materials for the future?,” *Mater. Today*, vol. 19, no. 2, pp. 69–87, 2016.

[53] S. V. Dorozhkin, “Calcium orthophosphate bioceramics,” *Eurasian Chem. J.*, vol. 12, no. 3–4, pp. 247–258, 2010.

[54] M. Sadat-Shojai, M. T. Khorasani, E. Dinpanah-Khoshdargi, and A. Jamshidi, “Synthesis methods for nanosized hydroxyapatite with diverse structures,” *Acta Biomater.*, vol. 9, no. 8, pp. 7591–7621, 2013.

[55] M. Pawlikowski, “Biomineralogical Investigation of Apatite Piezoelectricity,” *Adv. Recycl. Waste Manag.*, vol. 02, no. 01, pp. 2–7, 2017.

[56] M. P. Ferraz, F. J. Monteiro, and C. M. Manuel, “Hydroxyapatite nanoparticles : A review of,” *J. Appl. Biomater.*, vol. 2, no. 2, pp. 74–80, 2004.

[57] S. K. Swain, S. V. Dorozhkin, and D. Sarkar, “Synthesis and dispersion of hydroxyapatite nanopowders,” *Mater. Sci. Eng. C*, vol. 32, no. 5, pp. 1237–1240, 2012.

[58] P. Turon, L. del Valle, C. Alemán, and J. Puiggalí, “Biodegradable and Biocompatible Systems Based on Hydroxyapatite Nanoparticles,” *Appl. Sci.*, vol. 7, no. 1, p. 60, 2017.

[59] Z. Evis and T. J. Webster, “Nanosize hydroxyapatite: doping with various ions,” *Adv. Appl. Ceram.*, vol. 110, no. 5, pp. 311–321, 2011.

[60] A. Gloria *et al.*, “Magnetic poly(-caprolactone)/iron-doped hydroxyapatite nanocomposite substrates for advanced bone tissue engineering,” *J. R. Soc. Interface*, vol. 10, no. 80, pp. 20120833–20120833, 2013.

[61] A. Tampieri *et al.*, “Intrinsic magnetism and hyperthermia in bioactive Fe-doped hydroxyapatite,” *Acta Biomater.*, vol. 8, no. 2, pp. 843–851, 2012.

[62] L. Sheikh, S. Sinha, Y. N. Singhababu, V. Verma, S. Tripathy, and S. Nayar, “Traversing the profile of biomimetically nanoengineered iron substituted hydroxyapatite: synthesis, characterization, property evaluation, and drug release modeling,” *RSC Adv.*, vol. 8, no. 35, pp. 19389–19401, 2018.

[63] T. Tite *et al.*, “Cationic substitutions in hydroxyapatite: Current status of the derived biofunctional effects and their in vitro interrogation methods,” *Materials (Basel).*, vol. 11, no. 11, pp. 1–62, 2018.

[64] J. Dhal, S. Bose, and A. Bandyopadhyay, “Influence of pentavalent dopant addition to polarization and bioactivity of hydroxyapatite,” *Mater. Sci. Eng. C*, vol. 33, no. 5, pp. 3061–3068, 2013.

[65] S. Panseri *et al.*, “Intrinsically superparamagnetic Fe-hydroxyapatite nanoparticles positively influence osteoblast-like cell behaviour,” *J. Nanobiotechnology*, vol. 10, pp. 1–10, 2012.

[66] M. S. Laranjeira *et al.*, “Different hydroxyapatite magnetic nanoparticles for medical imaging: Its effects on hemostatic, hemolytic activity and cellular cytotoxicity,” *Colloids Surfaces B Biointerfaces*, vol. 146, pp. 363–374, 2016.

[67] M. Hamidi, K. Rostamizadeh, and M. A. Shahbazi, “Hydrogel Nanoparticles in Drug Delivery,” *Intell. Nanomater. Process. Prop. Appl.*, vol. 60, pp. 583–624, 2012.

[68] K. Raemdonck, J. Demeester, and S. De Smedt, “Advanced nanogel engineering for drug delivery,” *Soft Matter*, vol. 5, no. 4, pp. 707–715, 2009.

[69] L. Duan, Y. Wang, Y. Zhang, Z. Wang, Y. Li, and P. He, “pH/redox/thermo-stimulative nanogels with enhanced thermosensitivity via incorporation of cationic and anionic components for anticancer drug delivery,” *Int. J. Polym. Mater. Polym. Biomater.*, vol. 67, no. 5, pp. 288–296, 2018.

[70] S. E. Averick *et al.*, “Preparation of cationic nanogels for nucleic acid delivery,” *Biomacromolecules*, vol. 13, no. 11, pp. 3445–3449, 2012.

[71] Y. Sasaki and K. Akiyoshi, “Self-assembled Nanogel Engineering for Advanced Biomedical Technology,” *Chem. Lett.*, vol. 41, no. 3, pp. 202–208, 2012.

[72] N. Morimoto, T. Endo, M. Ohtomi, Y. Iwasaki, and K. Akiyoshi, “Hybrid nanogels with physical and chemical cross-linking structures as nanocarriers,” *Macromol. Biosci.*, vol. 5, no. 8, pp. 710–716, 2005.

[73] S. Laurent *et al.*, “Magnetic Iron Oxide Nanoparticles: Synthesis, Stabilization, Vectorization, Physicochemical Characterizations, and Biological Applications,” *Chem. Rev.*, vol. 108, no. 6, pp. 2064–2110, 2008.

[74] T. Junkers and C. Barner-Kowollik, “The role of mid-chain radicals in acrylate free radical polymerization: Branching and scission,” *J. Polym. Sci. Part A Polym. Chem.*, vol. 46, no. 23, pp. 7585–7605, Dec. 2008.

[75] Z. Shakoori *et al.*, “Fluorescent multi-responsive cross-linked P(N-isopropylacrylamide)-based nanocomposites for cisplatin delivery,” *Drug Dev. Ind. Pharm.*, vol. 43, no. 8, pp. 1283–1291, 2017.

[76] M. Destribats *et al.*, “Impact of pNIPAM microgel size on its ability to stabilize pickering emulsions,” *Langmuir*, vol. 30, no. 7, pp. 1768–1777, 2014.

[77] S. Motaali, M. Pashaeiasl, A. Akbarzadeh, and S. Davaran, “Synthesis and characterization of smart N-isopropylacrylamide-based magnetic nanocomposites containing doxorubicin anti-cancer drug,” *Artif. Cells, Nanomedicine Biotechnol.*, vol. 45, no. 3, pp. 560–567, 2017.

[78] O. Mergel, A. P. H. Gelissen, P. Wünnemann, A. Böker, U. Simon, and F. A. Plamper, “Selective Packaging of Ferricyanide within Thermoresponsive

Microgels," *J. Phys. Chem. C*, vol. 118, no. 45, pp. 26199–26211, 2014.

[79] C. D. Jones and L. A. Lyon, "Synthesis and characterization of multiresponsive core-shell microgels," *Macromolecules*, vol. 33, no. 22, pp. 8301–8306, 2000.

[80] P. L. Turecek, M. J. Bossard, F. Schoetens, and I. A. Ivens, "PEGylation of Biopharmaceuticals: A Review of Chemistry and Nonclinical Safety Information of Approved Drugs," *J. Pharm. Sci.*, vol. 105, no. 2, pp. 460–475, 2016.

[81] K. Raza, P. Kumar, N. Kumar, and R. Malik, "Pharmacokinetics and biodistribution of the nanoparticles," *Adv. Nanomedicine Deliv. Ther. Nucleic Acids*, pp. 166–186, 2017.

[82] L. Lin, S. W. Yee, R. B. Kim, and K. M. Giacomini, "SLC transporters as therapeutic targets: emerging opportunities," *Nat. Rev. Drug Discov.*, vol. 14, no. 8, pp. 543–560, Aug. 2015.

[83] H. S. Choi *et al.*, "Renal Clearance of Nanoparticle," *Nat. Biotechnol. NIH Public acces*, vol. 25, no. 10, pp. 1165–1170, 2007.

[84] R. Kumar, K. H. Prakash, P. Cheang, and K. A. Khor, "Temperature Driven Morphological Changes of Chemically Precipitated Hydroxyapatite Nanoparticles," vol. 8, no. 18, pp. 5196–5200, 2004.

[85] L. Russo *et al.*, "Carbonate hydroxyapatite functionalization : a comparative study towards (bio) molecules fixation," 2013.

[86] G. Penel, G. Leroy, C. Rey, and E. Bres, "MicroRaman Spectral Study of the PO 4 and CO 3 Vibrational Modes in Synthetic and Biological Apatites," pp. 475–481, 1998.

[87] M. Figueiredo, A. Fernando, G. Martins, J. Freitas, F. Judas, and H. Figueiredo, "Effect of the calcination temperature on the composition and microstructure of hydroxyapatite derived from human and animal bone," *Ceram. Int.*, vol. 36, no. 8, pp. 2383–2393, 2010.

[88] D. F. Mercado *et al.*, "Paramagnetic iron-doped hydroxyapatite nanoparticles with improved metal sorption properties. A bioorganic substrates-mediated synthesis," *ACS Appl. Mater. Interfaces*, vol. 6, no. 6, pp. 3937–3946, 2014.

[89] R. G. Carrodeguas and S. De Aza, "Acta Biomaterialia a -Tricalcium phosphate : Synthesis , properties and biomedical applications," *Acta Biomater.*, vol. 7, no. 10, pp. 3536–3546, 2011.

[90] A. K. Bain and P. Chand, "Ferroelectric Ceramics: Devices and Applications," *Ferroelectrics*, no. i, pp. 195–306, 2017.

[91] R. Rodriguez, D. Rangel, G. Fonseca, M. Gonzalez, and S. Vargas, "Piezoelectric properties of synthetic hydroxyapatite-based organic-inorganic hydrated materials," *Results Phys.*, vol. 6, pp. 925–932, 2016.

[92] L. Pedesseau, C. Katan, and J. Even, "On the entanglement of electrostriction and non-linear piezoelectricity in non-centrosymmetric materials," *Appl. Phys. Lett.*, vol. 100, no. 3, 2012.

[93] S. L. Aktuğ, S. Durdu, E. Yalçın, K. Çavuşoğlu, and M. Usta, "Bioactivity and biocompatibility of hydroxyapatite-based bioceramic coatings on zirconium by plasma electrolytic oxidation," *Mater. Sci. Eng. C*, vol. 71, pp. 1020–1027, 2017.

[94] A. Danese *et al.*, "Calcium regulates cell death in cancer: Roles of the

mitochondria and mitochondria-associated membranes (MAMs)," *Biochim. Biophys. Acta - Bioenerg.*, vol. 1858, no. 8, pp. 615–627, 2017.

[95] L. Ghibelli, C. Cerella, and M. Diederich, "The dual role of calcium as messenger and stressor in cell damage, death, and survival," *Int. J. Cell Biol.*, vol. 2010, 2010.

[96] K. Bauckman, E. Haller, N. Taran, S. Rockfield, A. Ruiz-Rivera, and M. Nanjundan, "Iron alters cell survival in a mitochondria-dependent pathway in ovarian cancer cells," *Biochem. J.*, vol. 466, no. 2, pp. 401–413, 2015.

[97] N. Riaz, S. L. Wolden, D. Y. Gelblum, and J. Eric, "HHS Public Access," vol. 118, no. 24, pp. 6072–6078, 2016.

[98] K. Kamińska *et al.*, "The role of the cell-cell interactions in cancer progression," *J. Cell. Mol. Med.*, vol. 19, no. 2, pp. 283–296, 2015.

[99] R. Meena, K. K. Kesari, M. Rani, and R. Paulraj, "Effects of hydroxyapatite nanoparticles on proliferation and apoptosis of human breast cancer cells (MCF-7)," *J. Nanoparticle Res.*, vol. 14, no. 2, 2012.

[100] S. Rockfield, R. Chhabra, M. Robertson, N. Rehman, R. Bisht, and M. Nanjundan, "Links Between Iron and Lipids: Implications in Some Major Human Diseases," *Pharmaceuticals*, vol. 11, no. 4, p. 113, 2018.

[101] J. A. Olzmann and P. Carvalho, "Dynamics and functions of lipid droplets," *Nat. Rev. Mol. Cell Biol.*, vol. 20, no. 3, pp. 137–155, 2019.

[102] B. Wang *et al.*, "Breast fibroblasts in both cancer and normal tissues induce phenotypic transformation of breast cancer stem cells: a preliminary study," *PeerJ*, vol. 6, p. e4805, 2018.

[103] L. Vuolo, C. Di Somma, A. Faggiano, and A. Colao, "Vitamin D and Cancer," *Front. Endocrinol. (Lausanne).*, vol. 3, no. April, pp. 481–495, 2012.

[104] P. Vikas, N. Borcherding, and W. Zhang, "The clinical promise of immunotherapy in triple-negative breast cancer," *Cancer Manag. Res.*, vol. 10, pp. 6823–6833, 2018.

[105] C. Wu and S. Zhou, "Effects of surfactants on the phase transition of poly(N-isopropylacrylamide) in water," *J. Polym. Sci. Part B Polym. Phys.*, vol. 34, no. 9, pp. 1597–1604, 1996.

[106] N. A. Jalili, M. K. Jaiswal, C. W. Peak, L. M. Cross, and A. K. Gaharwar, "Injectable nanoengineered stimuli-responsive hydrogels for on-demand and localized therapeutic delivery," pp. 15379–15389, 2017.

[107] H. P. Erickson, "Size and shape of protein molecules at the nanometer level determined by sedimentation, gel filtration, and electron microscopy," *Biol. Proced. Online*, vol. 11, no. 1, pp. 32–51, 2009.

Appendix

Appendix A

A.1 XRD Difractograms of the Non-Sintered Nanoparticles

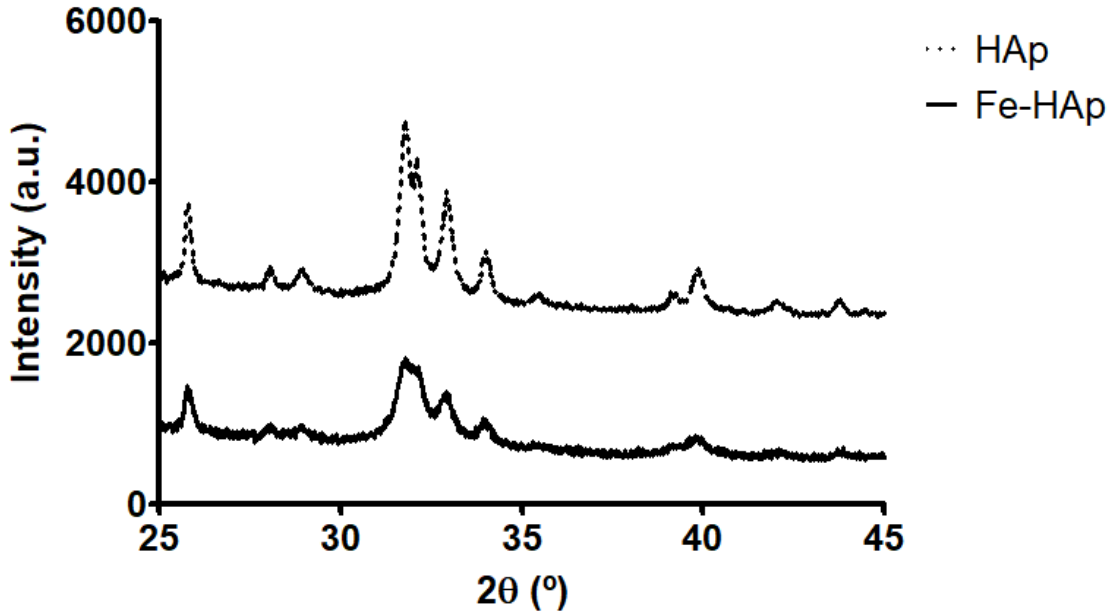

Figure A.1 - XRD difractograms of HAp and Fe-HAp samples. Vertical offset was adjusted for individual curve analysis.

A.2 PFM Contrast Regions

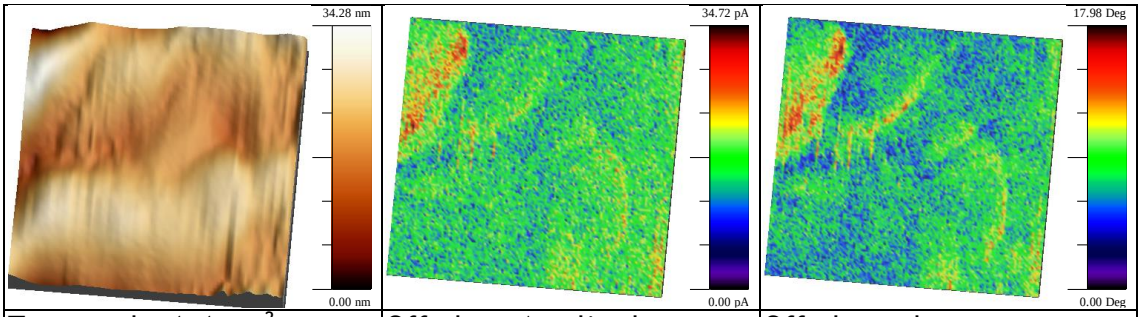

Topography 1x1 μm^2	Off-plane Amplitude	Off-plane phase

Figure A.2.1 – Topography and contrast regions of HAp obtained with PFM.

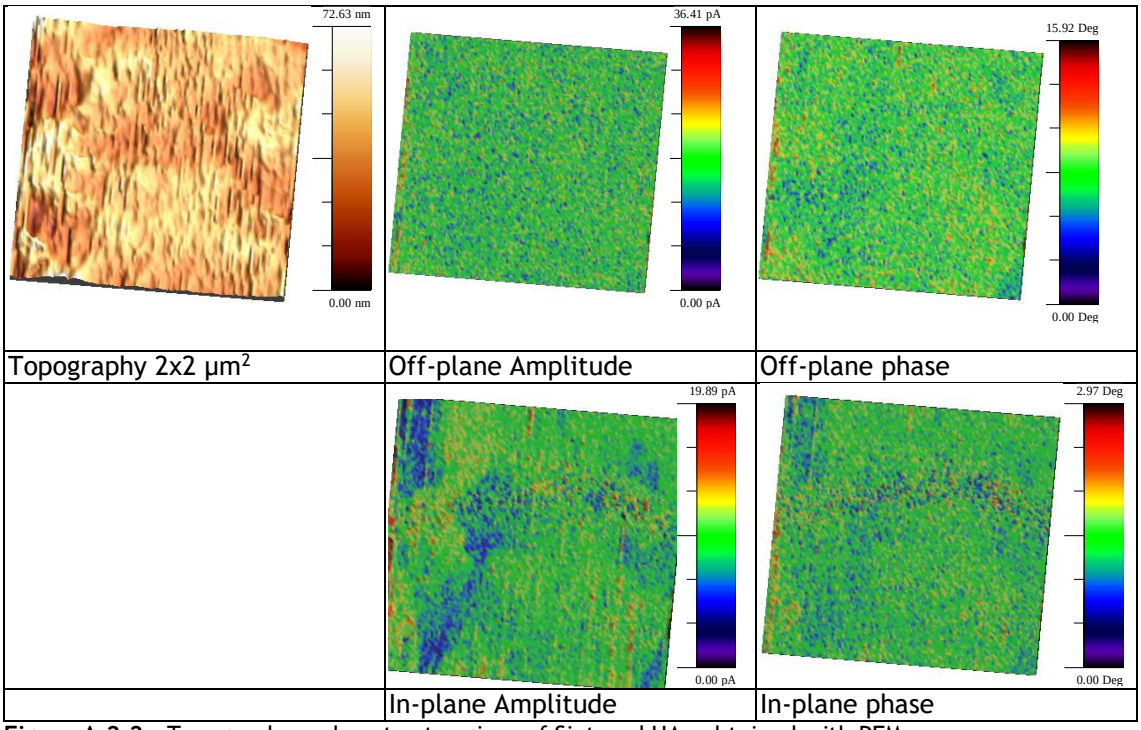

Topography 2x2 μm^2	Off-plane Amplitude	Off-plane phase
	In-plane Amplitude	In-plane phase

Figure A.2.2 - Topography and contrast regions of Sintered HAp obtained with PFM.

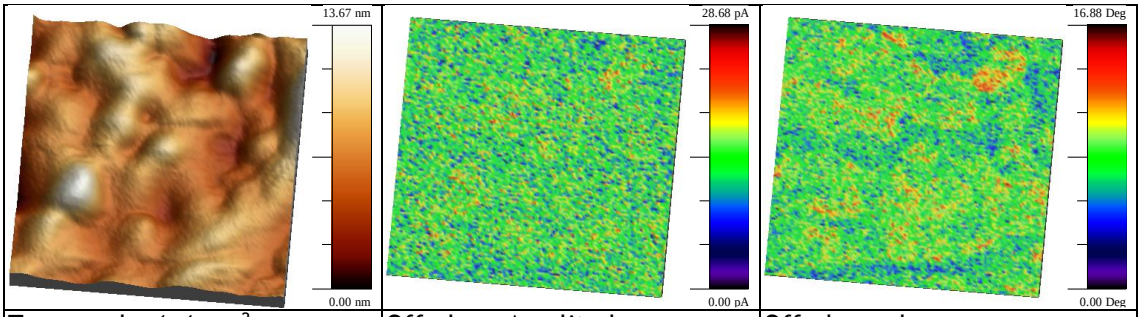

Topography 1x1 μm^2	Off-plane Amplitude	Off-plane phase

Figure A.2.3 - Topography and contrast regions of Fe-HAp obtained with PFM.

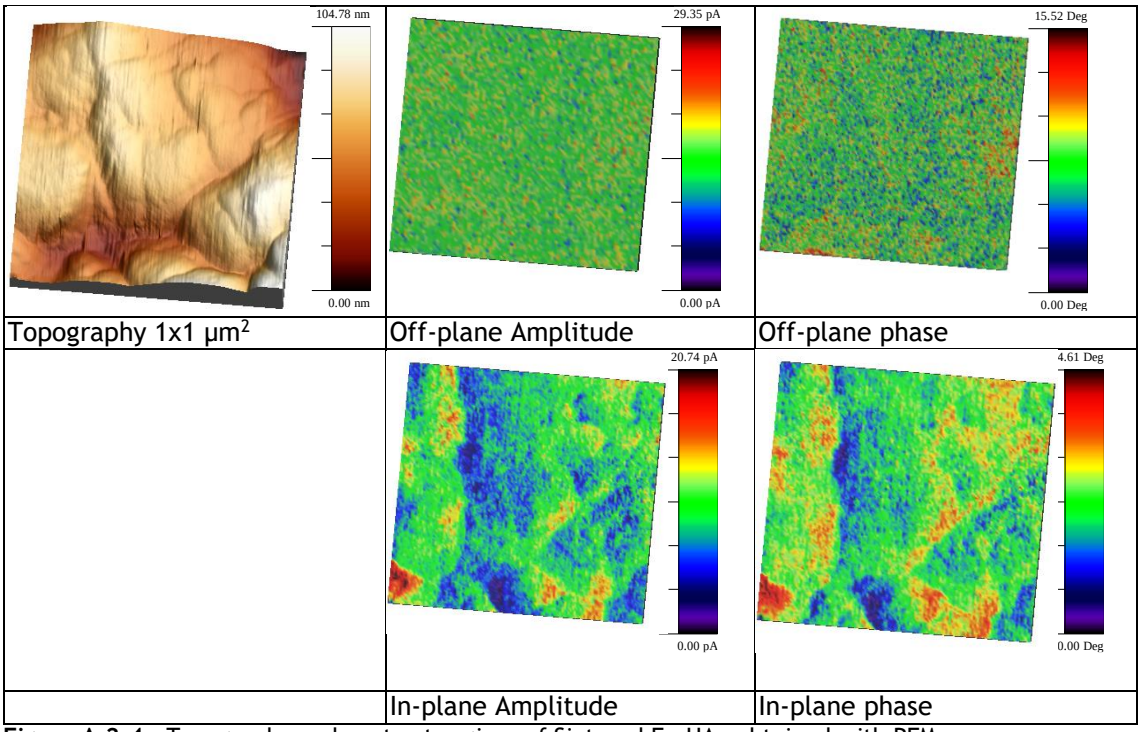

Figure A.2.4 - Topography and contrast regions of Sintered Fe-HAp obtained with PFM.

A.3 X-Ray Diffraction of Fe^{3+} Doped Hydroxyapatite

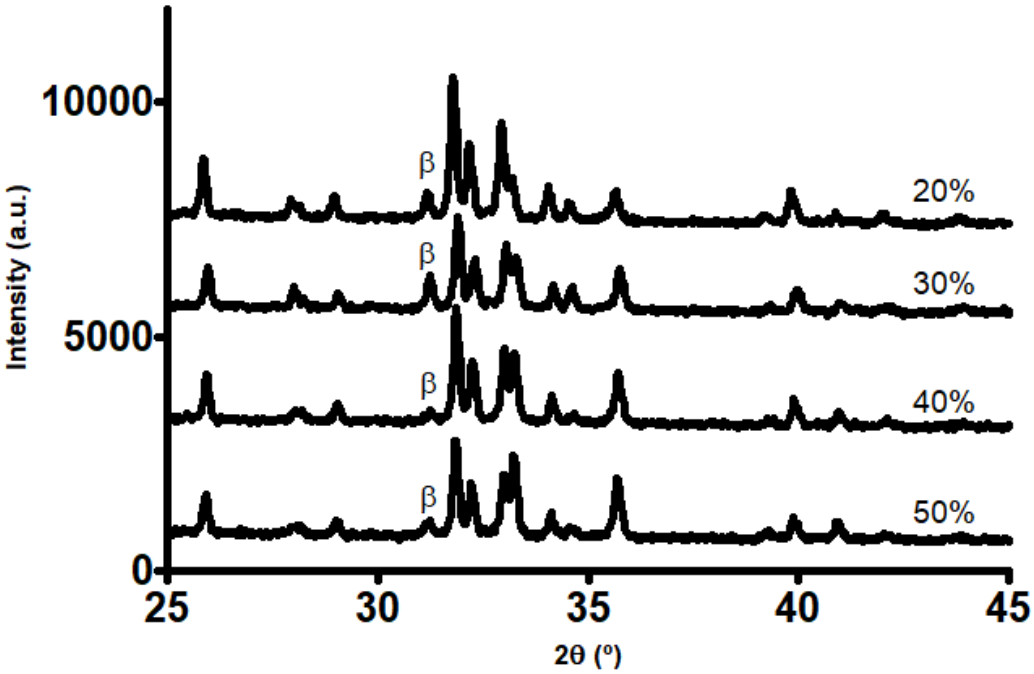

Figure A.3 – XRD difractograms of Fe-HAp samples doped at 20, 30, 40 and 50%. Peaks marked with β correspond to β-TCP phases, while non-marked peaks correspond to hydroxyapatite phases. Vertical offset was adjusted for individual curve analysis.